Predicting helicopter damage caused by a collision with an Unmanned Aerial System using explicit Finite Element Analysis.

Laurens Jonkheijm

(May, 2019)

TUDelft

This page is intentionally left blank.

Predicting helicopter damage caused by a collision with an Unmanned Aerial System using explicit Finite Element Analysis.

by

Laurens Jonkheijm

to obtain the degree of Master of Science
in Aerospace Engineering
at the Delft University of Technology,
to be defended publicly on Friday August 21, 2020 at 09:30 AM.

An electronic version of this thesis is available at `http://repository.tudelft.nl/`.

TU Delft

Abstract

Due to technological innovations in the Unmanned Aerial System (UAS) industry, the potential of these devices has increased remarkably in recent years. This led to an exponential increase in the number of shipments the last few years and this growth is expected to continue the upcoming years (Meola, 2017). The Federal Aviation Administration only permits the use of these devices without authorization in uncontrolled airspace and up to 400 ft. This airspace class is commonly shared with General Aviation aircraft and especially helicopter operators frequently operate below the UAS upper limit of 400 ft. In the United Kingdom alone, proximity incidents between UAS and aircraft have more than doubled from 40 encounters in 2015 to 94 in 2016 (Gilbert, 2017). Due to the increasing number of proximity incidents and the regularity of helicopter operations in the uncontrolled airspace, the question arises how much damage a helicopter can sustain after colliding with a UAS. Since it was not feasible for this research to actually impact a UAS on a helicopter, it was decided to simulate the collision in explicit Finite Element Analysis software. The research objective of this thesis was therefore defined as follows:

The objective of this thesis was to predict the helicopter's damage caused by a collision with an Unmanned Aerial System using explicit Finite Element Analysis.

Prior to modelling the collision, a risk analysis was completed to determine which impact in terms of UAS category and helicopter impact location poses the highest risk to the operator. Based on the prevailing UAS regulations (chance) and the kinetic energy of the UAS (effect), a UAS with a weight between 250 g and 25 kg would pose the highest risk. For the helicopter impact location, this would be the case for an impact onto the main rotor blade or windshield based on relative size of each helicopter impact location or recorded bird strikes (chance) in combination with the criticality of these components (effect). Based on popularity of the DJI Phantom family and due to availability of validation data of the critical components of this UAS, it was decided to model a DJI Phantom III in the Finite Element software. The models of the critical components were subsequently validated using the results of the available validation ballistic tests. For the helicopter impact location, accurately modelling a main rotor blade was not feasible within the timeframe of this study. Therefore, a windshield model was created in the Finite Element software. The A-109 helicopter windshield was adopted since the material properties and an accurate Computer Aided Design geometry were available. No actual test results to validate the model have been published, instead, a design process was completed to create a windshield compliant with the Part 29 certification requirements.

By means of simulating the collision, it was demonstrated that the A-109 Part 29 compliant windshield would sustain severe damage after a collision with the DJI Phantom III. Not only would the windshield break into dangerous fragments that could enter the cockpit, parts of the UAS would also penetrate the windshield thereby potentially severely injuring the crew. It was therefore concluded that the certification requirements did not guarantee a similar level of safety in case the windshield was impacted by this UAS. The results have initially been obtained in the most favourable conditions for the crew. This was the case if the UAS was oriented in its forward flying direction, clamped boundary conditions were a realistic representation of the surrounding windshield structure, and the Part 29 certification requirements applied to the rotorcraft. If any of these conditions were altered, the damage to the windshield even further increased and more parts of the UAS penetrated the cockpit station therefore further increasing the risk for the helicopter occupants.

Contents

List of Tables

List of Figures

Nomenclature

Abbreviations

Abbreviation	Description
AAIB	Air Accidents Investigation Branch
AC	Advisory Circular
AGL	Above Ground Level
ALE	Arbitrary Lagrangian-Eulerian
ARAC	Aviation Rulemaking Advisory Committee
ASSURE	Alliance for System Safety of UAS through Research Excellence
CAD	Computer Aided Design
CFR	Code of Federal Regulations
CS	Certification Specification
EASA	European Aviation Safety Agency
EC	European Commission
EOS	Equation Of State
EU	European Union
FAA	Federal Aviation Administration
FE	Finite Element
FEA	Finite Element Analysis
FEM	Finite Element Method
LSTC	Livermore Software Technology Corporation
MMPDS	Metallic Materials Properties Development and Standardization
MTOW	Maximum Take Off Weight
NOTAM	NOtice To AirMen
NTSB	National Transportation Safety Board
SPH	Smoothed Particle Hydrodynamics
TSSFAC	Time Step Scale FACtor
UAS	Unmanned Aerial System(s)
VLOS	Visual Line Of Sight

Symbols

Symbol	Description	Unit
A	Strain hardening constant	MPa
B	Strain hardening coefficient	MPa
C	Strain rate coefficient	-
C_{cs}	Cowper-Symonds strain rate parameter	1/s
$C(\epsilon_V)$	Tabulated pressure value	MPa
c	Speed of sound	m/s
D	Johnson-Cook failure parameters	-
d	Diameter	cm
E	Modulus of elasticity	GPa
E_k	Kinetic energy	J
E_t	Tangent modulus	MPa
l	Length	cm
l_{char}	Characteristic length	m
m	Mass	kg
m_t	Thermal softening exponent	-
n	Strain hardening exponent	-
P	Pressure	MPa
p	Cowper-Symonds strain rate parameter	-
S_{ts}	Time step scale factor	-
T_1	Translation in the 1-axis	-
t	Time	s
V	Velocity	m/s
V_{max}	Maximum velocity	m/s
W	Weight	kg
Y_t	Tensile cut off	MPa

Symbol	Description	Unit
β	Hardening parameter	-
Δt	Time step	s
Δt_{crit}	Critical time step	s
$\dot{\epsilon}$	Strain rate	1/s
ϵ_{max}	Failure strain	-
ϵ_V	Volumetric strain	-
θ_1	Rotation around the 1-axis	-
ν	Poisson's ratio	-
ρ	Density	kg/m^3
σ	Compressive stress	MPa
σ_d	Dynamic yield stress	MPa
σ_s	Static yield stress	MPa
σ_y	Yield stress	MPa

<div align="right">

1

</div>

Introduction

1.1. Background and motivation

Due to technological innovations in the Unmanned Aerial System (UAS) industry, the potential of these devices has increased remarkably over the last few years. Approximately a decade ago, the mainly used unmanned systems for recreational purposes were radio controlled airplanes operated by private modeller flying clubs. Currently millions of people around the globe own a UAS with a camera to for example create personal videos of all sorts of activities. The increasing potential of UAS also applies for commercial purposes. For example Volocopter is amongst other companies developing an autonomous air taxi and Amazon already started to deliver the first packages with unmanned multicopter systems as shown in Figure 1.1.

(a) *Volocopter Autonomous Air Taxi (Volocopter, 2020).*

(b) *Amazon UAS package delivery (Amazon, 2020).*

(c) *DJI Mavic Air follow me mode (DJI Technology Co., 2020a).*

Figure 1.1: *UAS example recent technological innovations.*

The increasing potential of the various types of UAS led to an increasing demand, whilst the prices of the devices were decreasing due to technological developments in the industry. This resulted in the number of shipments increasing exponentially the last few years and according to estimates from Andrew Meola (2017) in the Business Insider, this growth is expected to continue the upcoming years as shown in Figure 1.2. Alongside with this growth, a proportionate increase in the number of UAS operations in the sky can be expected.
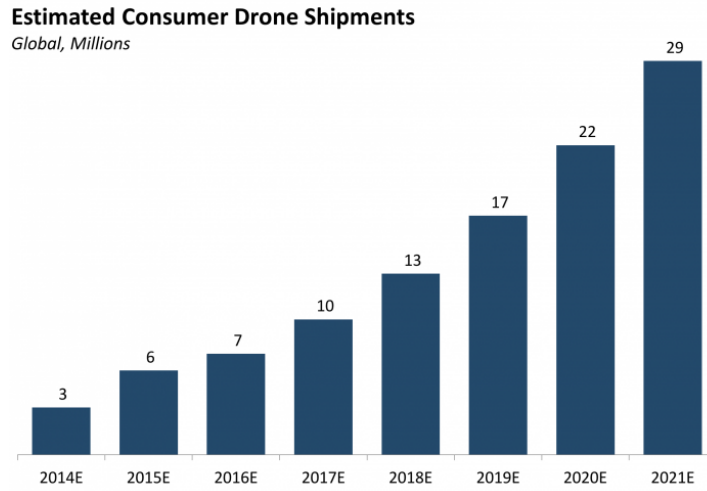
Figure 1.2: *UAS estimated number of shipments (Meola, 2017).*

When operating a UAS, the Federal Aviation Administration (FAA, 2020) only permits the use of these systems without a waiver or air traffic authorization in Class G airspace and up to 400 ft Above Ground Level (AGL) as shown in Figure 1.3. Class G airspace is the uncontrolled airspace and typically extends in the United States from ground level up to approximately 1200 ft AGL. Manned aircraft operating in this airspace are primarily General Aviation aircraft and military and governmental operators such as Helicopter Emergency Medical Service and police helicopters. For example airline operations are not permitted to fly in Class G airspace, whilst helicopters in contrary almost permanently operate within this airspace and frequently operate below the UAS upper limit of 400 ft AGL. This is especially applicable to military and other helicopters in governmental service, because these helicopters fly and land wherever the operation requires them to do so. Since Class G airspace is uncontrolled, collision avoidance is the responsibility of each individual operator including the UAS operators within this airspace. The FAA imposed the responsibility of remaining clear of manned aircraft on the UAS operators and not the other way around.
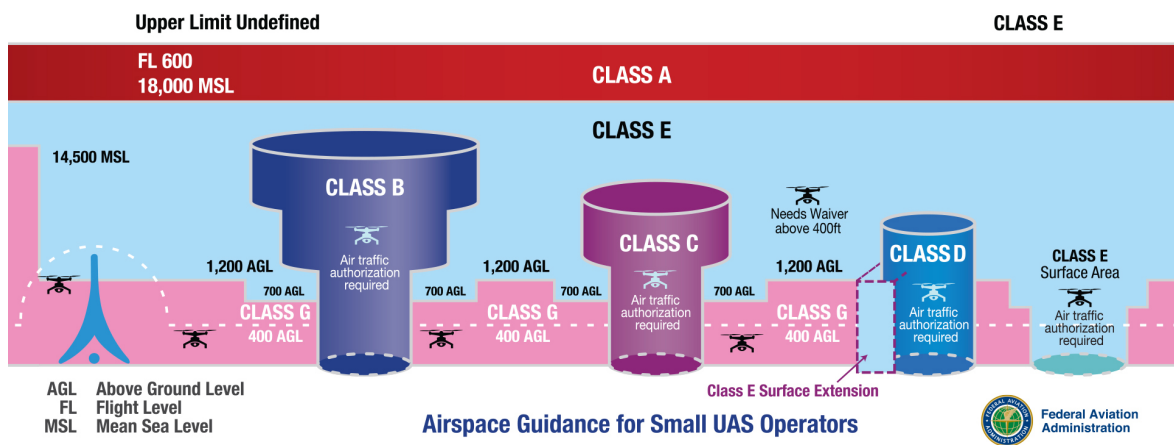
Figure 1.3: *UAS operators airspace guidance (FAA, 2020).*

Although operators should be familiar with the prevailing regulations, many UAS owners are either not aware of these regulations or consciously choose to ignore them. In addition, regulations are lagging behind the current technology making them unclear and in some instances unusable. These aspects increase the potential of a proximity incident between an aircraft and a UAS. In the United Kingdom alone, proximity incidents between UAS and aircraft have more than doubled from 40 encounters in 2015 to 94 in 2016 (Gilbert, 2017), whilst the number of aircraft-to-aircraft encounters remained constant over these years at approximately 170. The number of UAS proximity incidents is expected to grow proportionate to the estimated growth in number of shipments. 86% of the proximity incidents in the United Kingdom involved General Aviation aircraft, which is in line with the fact that these aircraft share certain parts of Class G airspace with the UAS operators.

Due to the increasing number of proximity incidents and the regularity of helicopter operations in the Class G airspace, the question arises how much damage a helicopter can sustain after colliding with a UAS. In the design of new helicopter, the sole collision related prevailing Certification Specification (CS) is CS §29.631 (EASA, 2018b, FAA, 2019b):

"The rotorcraft must be designed to ensure capability of continued safe flight and landing (for Category A) or safe landing (for Category B) after impact with a 1 kg bird, when the velocity of the rotorcraft (relative to the bird along the flight path of the rotorcraft) is equal to Vne or Vh (whichever is the lesser) at altitudes up to 2438 m (8000 ft)."

This requirement only applies to Transport (Part 29) category aircraft and is not applicable to the smaller Normal category rotorcraft (Part 27). The materials, structure, weight, and geometry of a UAS however significantly differ from a 1 kg bird. Therefore the expected damage after a collision would be different as well and is hence not taken into consideration during the design of a helicopter. At this moment, only a few UAS to helicopter collisions have been recorded. For example in 2017, a Sikorsky UH-60M Blackhawk helicopter of the US Army collided with a privately owned and operated DJI Phantom IV quadcopter. The helicopter sustained a 4 cm dent surrounded by various scratches and material transfer in the leading edge of one of the main rotor blades as shown in Figure 1.4 (NTSB, 2017). Additionally, some cracks were observed in the composite fairing and window frame material of the left hand cabin door. The sustained damage was considered minor and the crew could land uneventfully. However in contrary to civil rotorcraft, the UH-60 Blackhawk military helicopter is designed to continue its mission after sustaining considerable battle damage and not only to sustain safe flight after an impact with a 1 kg bird. How much damage a helicopter can sustain after a UAS collision therefore remains an unanswered question.
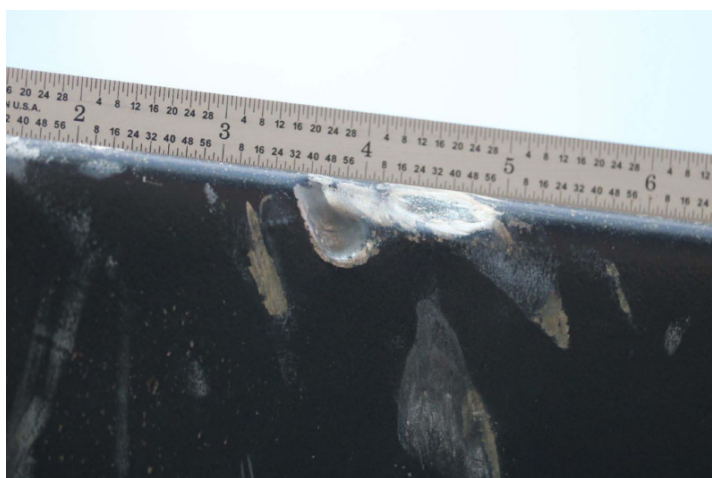
Figure 1.4: *Sikorsky UH-60M Blackhawk main rotor blade damage after UAS collision (NTSB, 2017).*

The National Transportation Safety Board (NTSB, 2017) concluded that a contributing factor to this incident was the UAS pilot's incomplete knowledge of the regulations and safe operating practices. This endorses the fact that the risk of a collision remains present, even though the prevailing regulations imposed by the FAA should prevent this.

1.2. Aim and scope

The increasing number of UAS in the sky and the fact that they share certain airspace with helicopters addresses the increasing potential of a helicopter-UAS collision occurrence. Since in accordance with the applicable certification requirements, a potential UAS collision does not have to be taken into consideration during the design phase of a helicopter, the question arises how much damage a helicopter can sustain by such a collision. Since it was not feasible for this research to actually impact a UAS on a helicopter, it was decided to simulate the collision in explicit Finite Element Analysis software. The research objective of this thesis was therefore defined as follows:

The objective of this thesis was to predict the helicopter's damage caused by a collision with an Unmanned Aerial System using explicit Finite Element Analysis.

In order to meet the objective as described above, 4 research questions have been drafted. The state-of-art regarding the thesis subject will be reviewed when answering the first question. The subsequent research questions are the main content of this study and will produce the data required to achieve the thesis objective.

1. What research has currently been published regarding the damage prediction of UAS to aircraft collisions and regarding creating a Finite Element model for these collisions? How does this thesis fit in the current state-of-art?

2. Which impact, in terms of impact location on the helicopter and the type of UAS involved in the collision, poses the highest risk to the helicopter operator?

3. How can an accurate and validated model of the following bodies be made in explicit Finite Element software?

    - The UAS.

    - The helicopter impact location(s).

4. What would be the damage on the helicopter impact location after the collision with the UAS has occurred?

1.3. Thesis layout

The structure of the research was aligned with the sequence of the research questions and therefore this report is arranged correspondingly. The literature regarding UAS to aircraft collisions has been reviewed in Chapter 2. This chapter concludes on how the research of this thesis fits in a gap in the current state-of-art and thereby answers the first research question. Furthermore, it provides information on how to model the collision in Finite Element (FE) software. Since it would be impossible to model all the potential collisions, a prioritization was made based on which collision poses the highest risk to the helicopter operator. The impact analyses are detailed in Chapter 3 and provide an answer to the second research question. Additionally it gives insight in the current UAS technology and prevailing UAS regulations. Subsequently in accordance with the third research question, FE models of the UAS, the DJI Phantom III, and the helicopter impact location, the windshield, were constructed in respectively Chapter 4 and 5. The collision between the two bodies is simulated in Chapter 6 and subsequently analysed as requested per research question 4. A discussion of the results of this research is included in Chapter 7. The conclusions and whether the thesis objective of this thesis was met, is detailed in Chapter 8. Recommendations on how this work may be continued are also incorporated in this chapter. Additional information supporting the work in the main body of the report is presented in the appendices. An overview of the layout of this study and how the various chapters of this report relate to the research questions is depicted in Figure 1.5.
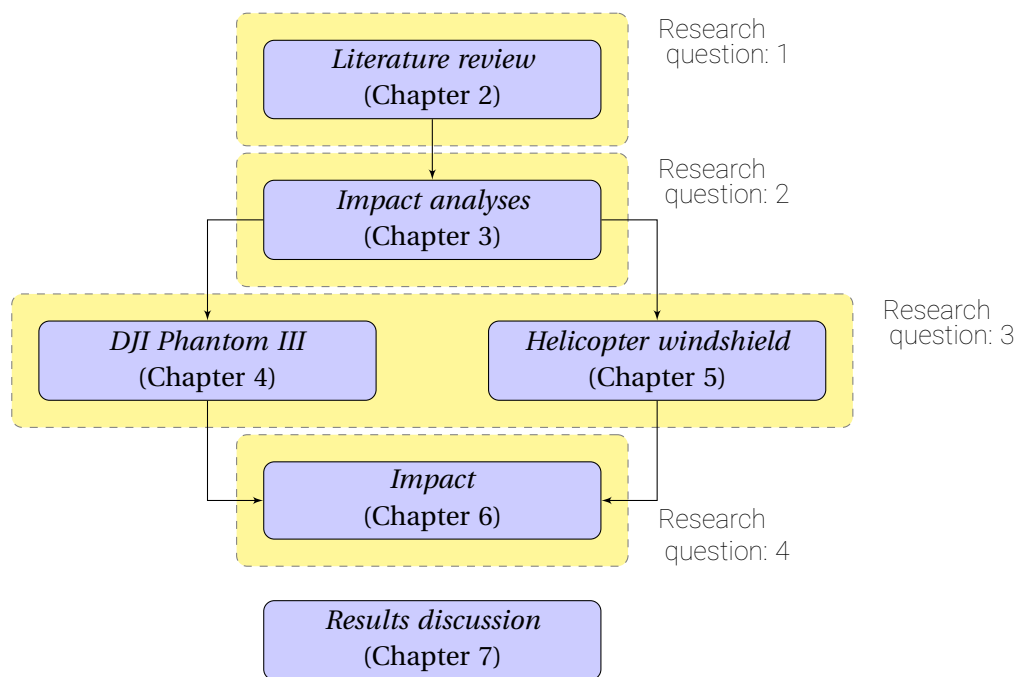
Figure 1.5: *Thesis layout.*

2

Literature review

To gain understanding of the existing studies regarding the damage prediction after UAS to aircraft collisions and to determine the modelling strategy for this study, a literature review is presented in this chapter. Prior to starting the research, a more detailed state-of-the-art review was completed and has been reported separately in the Literature Review of this thesis (Jonkheijm, 2019). However, a brief overview of this evaluation is presented below to help the reader in understanding the reasoning behind certain considerations made within this study. After reading this chapter, the first research question can be answered, namely what research has been published regarding the damage prediction for UAS to aircraft collisions and regarding the modelling strategy of these collisions.

In the first paragraph, an overview is presented of the research that has been completed on UAS to aircraft collisions. Subsequently in the next paragraph, an analysis was made to determine the modelling strategy for the UAS to helicopter collision. In line with this modelling strategy, the LS Dyna software package was selected and some features of this program are detailed in the third paragraph. After finishing the risk analysis in Chapter 3, it was concluded to model an impact onto the helicopter windshield in this study. Therefore in the fourth paragraph, research regarding impacts on aircraft windshields is presented. The literature review is summarized and an answer to the first research question is provided in the fifth and last paragraph.

2.1. UAS collision research

Alliance for System Safety of UAS through Research Excellence (ASSURE) (Olivares et al., 2017) published a comprehensive report on UAS impact assessments. In this research, two different types of UAS have been modelled, namely a quadcopter (DJI Phantom III) and a lightweight fixed wing UAS (Precision Hawk Lancaster). These UAS were impacted onto the following external components of a commercial transport and a business jet aircraft: horizontal and vertical stabilizer, windshield, wing's leading edge and engine inlet. The LS Dyna explicit Finite Element Analysis (FEA) solver was used with a Lagrangian numerical formulation. A detailed description of the FE strategy, such as the selected material models and contact algorithms, as well as the material properties of each component have been incorporated in the report. Additionally, the results of actual component level tests and the subsequent validation of the FE model was presented.

The comprehensive research performed by Olivares et al. (2017) formed the basis for multiple other researches. For example Lyons and D'Souza (2019) elaborated on this work by using the exact same DJI Phantom III FE model and ingesting it into a jet engine. Drumond, Greco, and Cimini (2019) simulated a UAS impact on a wing's leading edge of a fixed wing aircraft. In their research, only the critical components (motor, battery, and camera) of the DJI Phantom III were modelled and connected through 1-dimensional bar elements. Subsequently the results of the experimental tests of Olivares et al. (2017) were used to validate the FE model of these components. The material properties of the critical components were also detailed in the report. Both studies used explicit FEA and a Lagrangian mesh.

Meng et al. (2018) have reported on their research of a DJI Inspire 1 SZ colliding with a horizontal stabilizer of a commercial airliner. The numerical framework was developed and validated with results from a single experimental test. In this test, the entire UAS was impacted onto the stabilizer

at a velocity of 151 m/s. The FE strategy and the material parameters of the UAS have been detailed in the report and were implemented in the explicit dynamic code of PAM-CRASH. Following the validation process, series of simulations were conducted to assess the hazard of different collision scenarios, such as different impact angles and locations. In the conclusion, a comparison of the damage caused by a bird strike was made. The bird was simplified to a cylinder with hemispherical ends and a meshless Smoothed Particle Hydrodynamics (SPH) model was adopted.

The damage to the engine of a commercial airplane caused by an ingestion of a UAS was predicted by Song, Horton and Bayandor (2017) using explicit numerical integration and a Lagrangian formulation. Two virtual UAS were developed representing an average hobby and professional class UAS. For simplicity, only the main chassis, battery, motors and a camera were incorporated in the model. In the conclusion of this report, the impact damage of the different UAS types was compared to the damage caused by a bird ingestion. The modelling strategy was not detailed and no validation of the UAS models was conducted.

2.1.1. Evaluation

The research papers as presented above have multiple aspects in common. One of these aspects is the fact that only impacts onto fixed-wing aircraft have been modelled. The published literature does not encompass the helicopter damage prediction caused by a collision with a UAS. Therefore, the study in this thesis could fill this gap in the current state-of-art.

Since multiple research papers are based on the study of Olivares et al. (2017) and almost all research papers refer to this study in some form, it can be concluded that this report is the state-of-art regarding a UAS collision at the moment of conducting this thesis. Due to the comprehensive documentation of the process as well as the (test) results, this report provides a good reference when conducting this thesis research. Additionally, multiple studies have constructed accurate and validated FE models of different UAS types thereby endorsing the feasibility to meet the objective of this thesis.

2.2. FEM impact methods

In the previous paragraph, the relevance of this research has been addressed. The question remains how the UAS impact onto the helicopter can be modelled in a suitable software package. In this paragraph, an evaluation of various numerical integration and numerical mesh methods is presented.

2.2.1. Numerical integration methods

The two methods of numerical integration that are widely used in impact analysis are the implicit and explicit method (Rao, Narayanamurthy and Simha, 2016). In explicit Finite Element Methods (FEM), the state of a given system at the next time increment $(t + \Delta t)$ is calculated from the state of the system at the current time (t). In contrast, the implicit method requires the unknown state of the system at the next increment $(t + \Delta t)$ to solve the equilibrium equations. This is accomplished by enforcing equilibrium through iteration using for example the Newton-Raphson method. The implicit method requires additional computational steps, but is unconditionally stable. The explicit method is more computationally efficient for each individual time step, however, requires a smaller step size to remain stable.

Multiple research papers have been published regarding the suitable application regime of the implicit an explicit code as for example shown in Figure 2.1. An indication is given of the application regime of the two integration methods with respect to the strain rates of the materials involved in a certain engineering problem. Additionally, sample events for the different strain rate regimes have been added, which provide an indication of the expected strain rates in a comparable collision event.
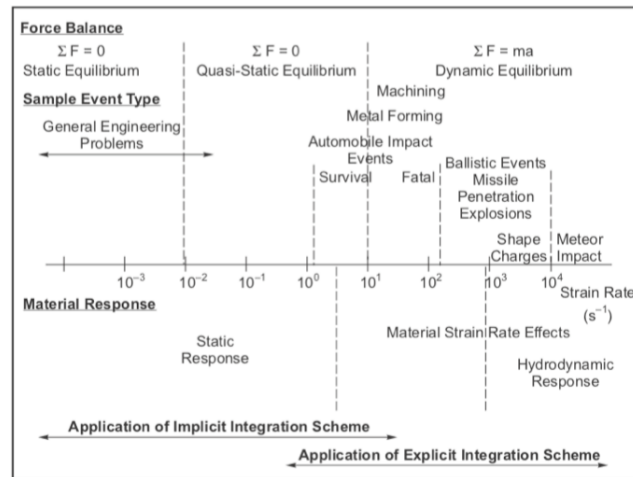
Figure 2.1: *Application of the numerical integration schemes (Zukas, 1990).*

2.2.2. Numerical mesh

In general, there are two groups of numerical formulations, namely the element-based and particle-based methods. Each of these methods has its own unique advantages and limitations depending on the engineering problem. In a Lagrangian formulation (Buyuk et al., 2004), each grid point has different material coordinates and connecting these grid points creates the elements in the FE model. As the body deforms, both the grid points and the material points change position, but the material points relative to the grid points remain fixed. In a Eulerian formulation the grid points remain fixed in space during deformation, whilst material flows from one element to the other. Elements are created by connecting the grid points. A combination of the Lagrangian en Eulerian method has been implemented in the so called Arbitrary Langrangian-Eulerian (ALE) coupling formulation. This method allows the Eulerian material to flow and coincide with the nodal points of the Lagrangian mesh. An additional computational step is incorporated to move the grid and remap the solution onto this grid. The most widely used particle-based method is the SPH method developed by Gingold and Monaghan (1977) and Lucy (1977). It is a mesh free technique in which free movable points with a fixed mass, called particles, have coherence by means of an interpolation function. A kernel estimate describes the conservation of mass, momentum and energy in terms of interpolation sums.

As detailed in Donea et al. (2004), the Lagrangian method permits an easy tracking of the deformation and interfaces of the various materials in the simulation. Severe mesh distortions are a typical difficulty, but can be overcome by an erosion mechanism which removes the severely distorted elements. Eulerian algorithms can deal with relatively large deformations, however, the interface definitions can be imprecise with limited resolution of flow details. The best features of both the algorithms as described above are combined into the ALE method at the cost of computational efficiency. The particle-based SPH method is capable of dealing with excessive local deformations compared to the element-based methods. Since it is a gridless technique, there is no grid tangling. Drawback of the method is that it can suffer from tensile instabilities and in some cases a lack of consistency.

2.2.3. Evaluation

In general, explicit integration is computationally more efficient for dynamic problems involving higher strain rates, whilst the implicit method requires less computational time in more static events. Since the engineering problem in this research involves impact analysis with a highly dynamic response, application of the explicit code prevails over implicit analysis. This decision is supported by

the fact that all the work already completed on UAS impacts, as detailed in Paragraph 2.1, also made use of explicit FEA.

The contact area between the colliding bodies is more accurately defined in a Lagrangian mesh compared to an Eulerian mesh, whilst the ALE-method requires significantly more computational expense. Therefore a Lagrangian formulation is the preferred element-based method for the simulation in this research. Although the SPH method can be a serious alternative to the Lagrangian mesh in case of brittle material behaviour, all the completed work on UAS impacts onto aircraft (Paragraph 2.1) made use of a Lagrangian formulation. Certain data from these studies can therefore more easily be compared with the results of this thesis in case the same formulation is used. Based on these arguments, the Lagrangian formulation prevails for use in this research to mesh the various parts of the UAS.

2.3. LS Dyna software package

One of the most widely used software packages for impact analysis is LS Dyna from Livermore Software Technology Corporation (LSTC). The code's origin lies in highly non-linear, transient dynamic FEA using explicit time integration. Due to its established reputation and the decision of using an explicit solver (Paragraph 2.2) in the study, this FEA package was selected for modelling the collision. At the time of completing the study, the software version of LS Dyna was R10.2.0 and the PrePost processor software was at version 4.6. LS Dyna uses by default its explicit code and a Lagrangian formulation. Some specific features of this software package have been detailed below.

2.3.1. Time step size

One of the most important parameters in explicit FEM simulations is the size of the time step. As explained in Paragraph 2.2.1, the time step should be sufficiently small for an explicit solver to guarantee stability. In LS Dyna, this time step (Δt) is automatically set as follows:

$$\Delta t = S_{ts} \cdot \Delta t_{crit}$$

In this equation, S_{ts} is a scale factor for the time step and Δt_{crit} is the critical time step. The S_{ts}, referred to as the Time Step Scale FACtor (TSSFAC) in the LS Dyna manual (LSTC, 2018a) and PrePost processor, is a user defined scale factor for the time step, which is by default set to a value of 0.9. LS Dyna recommends to lower this value to 0.67 in higher explosive events, which would be at the cost of an increased computation time. The critical time step (Δt_{crit}) is dependent on the size and shape of the elements and is calculated as follows:

$$\Delta t_{crit} = \frac{l_{char}}{c}$$

in which l_{char} is the characteristic length of an element and c the speed of sound. The element's shape and size determines the characteristic length, which is calculated in various ways depending on the type of the element (solid, shell etc.). The speed of sound is affected by the material properties of the specific element such as its density. LS Dyna calculates the critical time step for each individual element and uses the smallest value to set the actual time step of the simulation.

2.3.2. Contact algorithm

Over 150 different contact algorithms can be selected in LS Dyna. Unless stated otherwise, the selected contact algorithm in this research was the *CONTACT_AUTOMATIC_SURFACE_TO_ SURFACE, which is a penalty-based contact algorithm (LSTC, 2018a). The thickness offset of a shell element is considered in this algorithm by projecting the contact surface normally from the shell's mid-plane at a distance of half of the shell thickness. This automatic contact option is non-oriented,

meaning that penetration can be detected from either side of the shell element. This is recommended in case the orientation of parts relative to each other cannot be anticipated as for example parts in the simulation experience large deformations. Two-way treatment of contact is taken into account which checks the slaves nodes for penetrating the master segments and vice versa making the master-slave definition arbitrary. LS Dyna default values have been used for the algorithm's variables, such as the static and dynamic coefficient of friction throughout, therefore only requiring the master and slave parts to be defined. Although the computational time required for this algorithm would be more than for example a non-automatic algorithm, this contact algorithm was selected since the way the bodies would deform and interact with each other could not be predicted at the time.

2.4. Aircraft windshield

After finishing the risk analysis in Chapter 3, it was concluded to model an impact onto the helicopter windshield. Unlike for UAS impacts on helicopter windshields, a number of reports have been published simulating bird strikes on rotorcraft windshields. An overview of the various windshield models and the considerations regarding the imposed boundary conditions are presented below.

2.4.1. Windshield model

For example, Hedeyati et al. (2014) performed an analysis of bird strike simulations on helicopter windshields with different lay-ups, such as a single layer acrylic and a laminated lay-up. For each different lay-up, the minimum thickness was determined which did not allow bird penetration. This process was based on certification requirements for transport category rotorcraft (Part 29). Cwiklak and Grzesik (2016) performed a similar study, investigating a bird strike onto an Agusta 109 helicopter windshield. Both studies based their FE model of the windshield on simulations only and did not validate the simulations. The material parameters and material models were incorporated in both the reports. Due to the geometry of the windshield, 2 dimensional shell elements were employed to represent the structure of single layer windshields. After a comparison of various numerical meshes for the bird model, most accurate results were obtained in case the bird was modelled by means of the SPH method.

2.4.2. Boundary conditions

Typically, the windshield of a rotorcraft is attached to its surrounding frame with rivets or screws, thereby clamping the windshield to this frame as shown in Figure 2.2. Sealant is applied to close the remaining openings between the windshield and the framework. In most of the published reports, such as the study of Hedeyati et al. (2014) and Cwiklak and Grezsik (2016), the surrounding structure was not incorporated in the model but simplified by imposing clamped boundary conditions to the edges of the windshield. Whether the clamped boundary conditions would be realistic depends in this case on the stiffness of the surrounding structure. In case the framework stiffness is high, the clamped conditions could be appropriate. In case the framework is more flexible, the surrounding structure could deflect more easily and the clamped conditions would not be appropriate. As an example for comparison of different windshield frameworks, the frontal view of the UH-60 Blackhawk and the Robinson R22 are presented in Figure 2.2. It can be seen that the structure of the windshield framework differs significantly between these two aircraft types and the stiffness of the two would be dissimilar.

Two recordings of bird strike tests were available on the internet, both without further details of the test conditions. Robinson Helicopter Company (2020) showed a bird strike impact test on their new impact-resistant windshield of the R22 and Ramirez (2014) presented an impact test on an unknown helicopter type (presumably Bell 412). The undeformed windshield as well as a screenshot

(a) *Sikorsky UH-60A Blackhawk (Domke, 2006).*

(b) *Robinson R22 (Browne, 2009).*

Figure 2.2: *Example windshield surrounding structures.*

of the deformed windshield during these tests are shown in Figure 2.3. In both cases, the framework in between the cockpit windshields and at the top of the impacted windshield deflect notable and predominantly in their relative out-of-plane direction. The framework mainly supports the installation of the adjacent cockpit and overhead windshields. Due to the deflection of the windshield framework, the clamped boundary conditions at these edges of the windshield would not be appropriate in these cases to represent the surrounding structure. The bottom framework and edge of the windshield near the cockpit door remain fixed, possibly due to the strengthened structure to attach the door. Therefore clamped boundary conditions could be appropriate for these specific edges of the windshield.

In contrary to only modelling the windshield itself, Hu et al. (2016) performed simulations as well as a validation test on a full-scale helicopter composite cockpit structure. The objective was to build confidence to use an FE model as a predictive tool for certification purposes. Although the modelling strategy was described in detail, not all the data required to construct a similar model was included in the report. For example the geometry of the cockpit was not incorporated in the report.

Undeformed windshield.

Deformed windshield.
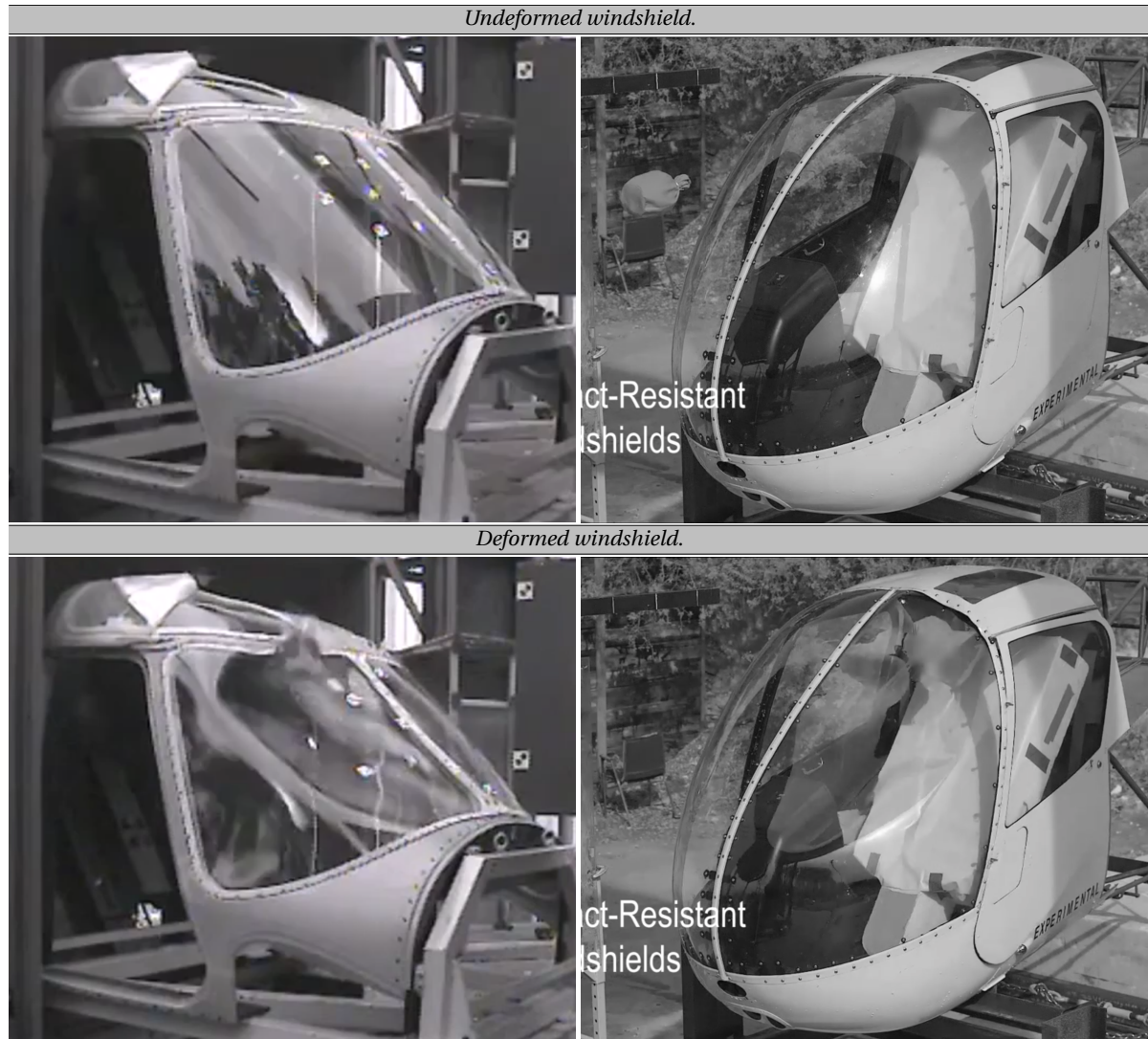
(a) *Unknown aircraft type
(Ramirez, 2014).*

(b) *Robinson R22
(Robinson Helicopter Company, 2020).*

Figure 2.3: *Windshield surrounding structures deformation during a bird strike test.*

2.4.3. Evaluation

Most of the studies focus on the analysis of birds striking fixed wing aircraft and only a handful reports have been reported regarding rotorcraft windshields. Multiple reports have included the modelling strategy such as the material model and parameters for the windshield in detail, thereby endorsing the feasibility of constructing a helicopter windshield model. However, only very limited results of validation tests of rotorcraft windshield impacts are freely available, making it not achievable to create a validated FE model. As an alternative, the approach as adopted by Hedeyati et al. (2014) can be used to create a purposeful windshield model. This approach included performing bird strike events to build a model that would comply with the certification requirements. Subsequently a conclusion can be drawn to assess the difference in damage caused by the bird strike and the UAS impact. Since almost all studies used an SPH model to represent the bird, this numerical mesh should be adopted for the bird model.

A simplification is often applied omitting the surrounding structure and instead implementing boundary conditions at the edges of the windshield. Whether these boundary conditions are appropriate depends highly on the stiffness of the surrounding structure. Recordings of bird impact tests showed that for these specific helicopter types, the clamped boundary conditions around all edges of the windshield would not be appropriate. In case the surrounding structure is included in the model, the reports describe the modelling strategy insufficiently for using a similar approach in this study. Therefore, the simplification by implementing boundary conditions to represent the surrounding structure of the windshield should be adopted initially. Thereafter, an attempt to represent the displacement of the surrounding framework as presented in the bird strike impact tests (Figure 2.3) through the boundary conditions should be made.

2.5. Conclusion

The aim of the literature review was to gain understanding of the existing studies regarding damage prediction caused by UAS to aircraft collisions and subsequently to determine the modelling strategy for this study. The analysis in this chapter provides an answer to the first research question of this study:

What research has currently been published regarding the damage prediction of UAS to aircraft collisions and regarding creating a Finite Element model for these collisions?
How does this thesis fit in the current state-of-art?

Multiple studies have been performed to predict the sustained damage on a fixed-wing aircraft after a UAS collision. For example Olivares et al. (2017) have provided a detailed report on a quadcopter colliding onto an fixed-wing airliner. The included validation process and corresponding results in the report endorse the feasibility of creating an accurate UAS model in this thesis. Due to the expected highly dynamic response during the collision, the explicit code prevails over implicit analysis. Since a comparison with the results of other studies can more easily be made in case the same numerical mesh is used, a Lagrangian formulation should be adopted in the FE model. The LS Dyna FE software's origin lies in dynamic explicit FEA and is therefore a suitable application for modelling the collision. Various bird strike events on helicopter windshields have been simulated and the modelling strategy is detailed in the respective reports. Therefore, a similar strategy can be used to create the helicopter windshield model in this thesis. Since there was no published literature available predicting the sustained damage on a rotorcraft caused by a UAS collision, this study could fill this gap in the current state-of-art.

3

Impact analyses

Since it would be impossible to model all the potential collision events between UAS and helicopters, a prioritization is required to determine which events should be modelled in the remainder of this study. The prioritization is completed by comparing the associated risk, based on a risk assessment, of each potential UAS to helicopter collision. After comparing the risk of the various impact scenarios, the second research question can be answered detailing which event poses the highest risk to the helicopter operator. A sub-purpose of this chapter is that this analysis provides the reader with an insight in the current UAS technology and the prevailing UAS regulations. Both these matters are undergoing constant significant developments at this time.

Risk is a function of chance, probability of the occurrence, and effect, consequence of the occurrence. Some events may have a severe effect, but are expected to occur only on extremely rare occasions, thereby posing a low risk. Other events may have a less severe effect, but are expected to occur more frequently, resulting in a relatively higher risk. The 3×3 risk matrix from Cox (2008) will be used in this chapter. The different levels of chance have been defined as improbable, possible, and probable. The three ratings of effect are negligible, moderate, and catastrophic. To provide the required resolution for prioritization of the impact events, three levels of risk have been identified, namely low, medium and high. The relationship between the levels of chance and effect with respect to the associated risk is detailed in the risk matrix in Table 3.1. Further detail to the thresholds and definitions of each level of effect and chance will be presented in the respective paragraphs. It should be noted that the result of this risk assessment only provides a qualitative distinction between the risk of various potential events, which is required to prioritize the different events with sufficient resolution. No statistical chance study to quantify the risk for the operator has been completed.

To categorize the risk of the different potential UAS to helicopter collisions, an analysis of the UAS operations in each UAS category is conducted and presented in the first paragraph. Subsequently in the second paragraph, the risk for the various helicopter impact locations is analysed. In both paragraphs, the chance as well as the effect of each aspect is assessed to determine the risk level. This chapter is summarized in the third and last paragraph in which the second research question is answered. More detail on the method of determining the chance and effect of each aspect will be presented in the respective paragraphs. An overview of the entire process is depicted in Figure 3.1.

3.1. UAS risk

Following the process in Figure 3.1, the risk of a collision on the UAS side will be determined by analysing the chance and the effect of this collision. The regulations imposed by aviation authorities define the prerequisites for various UAS operations and have a direct relation with the chance of a collision as detailed in the first subparagraph. The factor of importance regarding the effect of the collision, as included in the second subparagraph, is the kinetic energy of the UAS. The chance and effect for each UAS category are combined to determine the level of risk in the third subparagraph. To put the analysis in this paragraph into current perspective, some examples of present-day fixed-wing and multicopter UAS have been presented in Figure 3.2.

Table 3.1: *3×3 Risk matrix (Cox, 2008).*

		Effect		
		Negligible	Moderate	Catastrophic
Chance	Probable			High
	Possible		Medium	
	Improbable	Low		
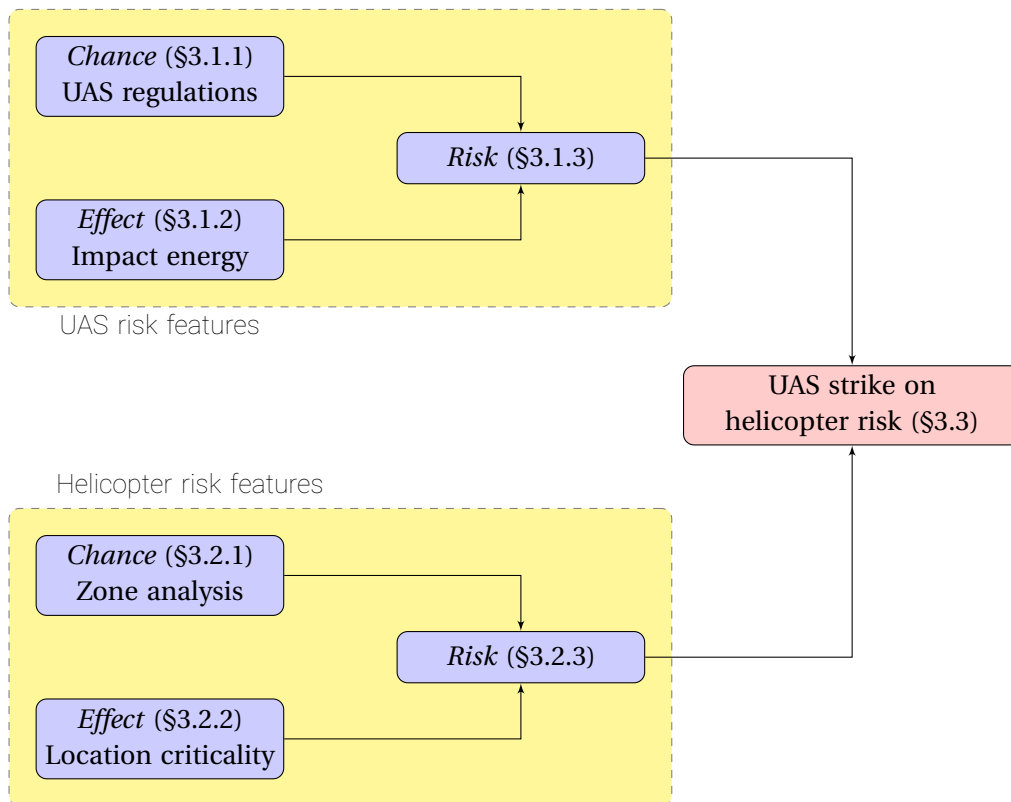
Figure 3.1: *Flowchart to determine the risk of a UAS strike on a helicopter.*

(a) *Parrot Airborne*
[Size: 18×18.5×4 cm]

(c) *DJI Phantom IV*
[Size: 29×29×19 cm]

(e) *Griff 350*
[Size: 265×280×50 cm]

(b) *TechOne Mini*
Popwing 600
[Wingspan: 60 cm]

(d) *SenseFly eBee*
[Wingspan: 96 cm]

Figure 3.2: *UAS models in the different categories.*

3.1.1. Chance: UAS regulations

Each UAS operator is obliged to adhere to the regulations imposed by the applicable aviation authority. Albeit that in some cases UAS operators are either not aware of these regulations or consciously decide to ignore them. The operating conditions affect the probability of a UAS colliding onto a rotorcraft. Analysing the UAS regulations therefore can lead to determining the level of chance of a collision with a rotorcraft. UAS regulations of two prominent aviation authorities, European Aviation Safety Agency (EASA) and the Federal Aviation Administration (FAA), are summarized below.

European Aviation Safety Agency

Mid 2019, the European Commission (EC) officially published the implementing regulation European Union (EU) 2019/947 (EC, 2019) in which the rules and procedures for the operation of unmanned aircraft is prescribed. Proportionate to the risk involved in each operation, the following three categories of operation have been defined: the open, specific, and certified category. Each category has its own associated regulatory regime.

Operations within the open category are identified as low-risk operations. There is no need for authorizations by a competent authority prior to conducting the operations nor is a declaration by the operator required. The potential risks in this category have been mitigated by implementing some strict regulations. The UAS must for example be flown under direct Visual Line-Of-Sight (VLOS) and the maximum operating altitude is 120 m AGL. The Maximum Take-Off Weight (MTOW) allowed is 25 kg and operations are not permitted within specified reserved areas such as airports. Only when operating a UAS weighing less than 250 grams, the vehicle does not have to be registered and the operator is not required to complete a training course with accompanying examination.

The specific category includes operations that do not meet the requirements of the open category by for example exceeding the MTOW of 25 kg. The operation therefore exceeds the risk of operations within the open category. The UAS operator is required to obtain an operational authorisation from the competent authority for operations in the specific category. When applying for this authorization, a risk assessment including adequate risk mitigation measures shall be submitted.

The UAS as well as its operator have to be certified, similar to the certification process in manned aviation, in case operations are conducted within the certified category. If an operation is conducted over assemblies of people, involves the transport of people, or involves the carriage of dangerous goods, the operation automatically is classified as an operation within this category. An alternative is that the competent authority, during the application for an operational authorisation within the specific category, considers that the risk of the operation cannot be adequately mitigated without the certification of the UAS and its operator.

Federal Aviation Administration

As opposed to EASA, which uses a risk-based categorization, the FAA makes a distinction between the purpose of the operation. Different regulations for example apply to recreational UAS operators compared to commercial operators.

In case the UAS is flown strictly for recreational purposes, operations can be conducted under Section 349 §44809 of the *FAA Reauthorization Act of 2018* and fall under the category of Recreational Flyers & Modeller Community-Based Organizations. The unmanned aircraft can be operated without specific certification or operating approval as long as the limitations under these rules are adhered to. These limitations for example include a maximum operating altitude of 400 ft AGL and operations must always be conducted within VLOS. Operations near other aircraft, over groups of people or over emergency response efforts are prohibited. The *FAA Reauthorization Act of 2018* introduced the requirement for the recreational operator to pass an online knowledge and safety test. At this stage the FAA is developing a long term plan for implementation of this requirement.

The small unmanned aircraft rule, 14 Code of Federal Regulations (CFR) §107 (FAA, 2019c) applies to the UAS category of Certificated Remote Pilots including Commercial Operators. These regulations are mandatory for operations with commercial purposes and include similar limitations compared to the regulations for recreational operators. The operator should be FAA-certified by passing a knowledge test in an FAA-approved Knowledge Testing Centre every 2 years. An operational authorization is not required as long as the limitations of this category are adhered to. Some operations are not covered by Part 107 and will require a waiver issued by the FAA. Common examples of Part 107 rules that are subject to waivers are: daylight operation, VLOS flying, operation in certain types of airspace and flight over people.

Both categories have in common that the MTOW is 55 lbs (25 kg) and that all UAS with a MTOW over 0.55 lbs (250 g) should be registered. In case an operation does not fall within either of the two categories presented above, it is considered an advanced operation and requires additional operational approval and may need certification. This includes for example emergency situations operations, such as firefighting missions, or operations with a UAS weighing more than 55 lbs.

Chance levels

When analysing the UAS regulations of the FAA and EASA, it can be seen that the prevailing regulations differ based on the MTOW of the UAS. For each of this UAS category, a level of chance is assigned by qualitatively assessing the applicable regulations for that specific category. The assessment is therefore of a qualitative nature and not based on quantitative data. An overview of the regulations for different UAS categories, based on the various groups of MTOW, is detailed in Table 3.2. In case EASA and the FAA imposed different regulations, a distinction between the two is presented.

Devices with a MTOW up to 250 g do not have to be registered and no operation authorization is required. Therefore only limited supervision is provided over operations within this category. Operator's training is not an EASA requirement and the FAA will only impose a brief online knowledge test in the future (currently not yet implemented). This makes the chance of the operator not being familiar with the regulations relatively high. Based on the combination of limited supervision and a high chance of unfamiliarity with the regulations, the chance level assigned to this category is probable.

An authorization of the UAS operation is mandatory when operating UAS with a MTOW exceeding 25 kg. A NOtice To AirMen (NOTAM) will be published prior to the operation thereby notifying all aircraft (manned and unmanned) operators of the operation. This reduces the chance of a collision significantly. In addition, a comprehensive training is mandatory for the UAS operator. An improbable chance level has been assigned to this category.

For the category of UAS with a MTOW between 250 g and 25 kg, the operation authorization is not required. However, the UAS must be registered and a more thorough examination is mandatory for the operator. The chance of a collision in this category therefore lies in between the two other categories and the assigned chance level is possible.

An interesting observation is that the UAS regulations of both the FAA and EASA are constantly updated with more strict regulations to reduce the risk of collisions. For example the requirement for recreational UAS operators to pass an online knowledge test has only been incorporated in the 2019 amendment of the FAA UAS regulations. At this moment a proposal by the FAA is pending that requires all new devices weighing more than 0.55 lbs (250 g) to connect over the internet to one of several location-tracking databases and provide real-time updates of their locations (FAA, 2019d).

Table 3.2: *UAS category chance analysis.*

UAS category	UAS registration	Operator's training		Operation authorization	Chance level
		FAA	**EASA**		
< 250 g[1,2]	No	Yes	No	No	Probable
250 g - 25 kg[1,2]	Yes	Yes	Yes	No	Possible
> 25 kg	Yes	Yes	Yes	Yes	Improbable

[1] For EASA, based on operations within limitations of open category.
[2] For FAA, based on operations within limitations of 14 CFR §107 (commercial) or Section 349 §44809 (recreational).

3.1.2. Effect: Impact energy

During an impact, energy is transferred between the colliding bodies. Kinetic energy is converted into other forms or energy, such as deformations, which could lead to structural damage. Dennis and Lyle (2009) analysed 11.000 bird strike incidents and found a strong correlation between the kinetic energy of the impact and the resulting damage to the aircraft. The kinetic energy of the UAS is therefore a quantitative measure of the expected resulting damage and can be used to determine the effect level. Albeit that the damage mechanisms in a bird strike event, soft body, will be different compared to the hard body impact of some of the UAS components. Further elaboration of this difference will be provided when analysing the UAS impact simulations in Chapter 6.

The kinetic energy (E_k) of a non-rotating object is:

$$E_k = \frac{1}{2}mV^2$$

in which E_k is the kinetic energy in joule, m is the mass in kilograms and V is the velocity in meters per second.

The parameters required to calculate the kinetic energy of the example UAS of Figure 3.2 are presented in Table 3.3. The results show that the kinetic energy of each category is of a different order of magnitude. The lightest category is in the order of one up to tens of joules, whilst the middle category is in the order of hundreds of joules. The example UAS weighing more than 25 kg can have

a kinetic energy in the order of tens of thousands of joules. Each category has been assigned an effect level based on this order of magnitude of the kinetic energy. The effect level for UAS weighing less than 250 g category is negligible and the 250 g - 25 kg category is assigned a moderate effect level. Devices weighing more than 25 kg are categorized into the catastrophic effect level.

Table 3.3: *UAS category effect analysis.*

UAS category	UAS model	m [kg]	V_{max} [m/s]	E_k [J]	Effect level
< 250 g	Parrot Airborne	0.063	5	0.8	Negligible
	TechOne Mini Popwing 600	0.140	27	51	
250 g - 25 kg	DJI Phantom IV	1.388	20	278	Moderate
	SenseFly eBee	0.69	25	300	
> 25 kg	Griff 350	350	17	50575	Catastrophic

3.1.3. Risk overview

The level of risk for each UAS category can be determined by combining the chance level, defined in Table 3.2, with the effect level, detailed in Table 3.3, into the 3×3 risk matrix as defined in Table 3.1. The result of this process is presented in the risk matrix in Table 3.4. This matrix shows that the UAS category for devices weighing more than 250 g and less than 25 kg poses a medium risk, whilst the other categories pose a low risk.

Table 3.4: *Risk matrix UAS category.*

		Effect		
		Negligible	Moderate	Catastrophic
Chance	Probable	< 250 g		
	Possible		250 g - 25 kg	
	Improbable			>25 kg

3.2. Helicopter Risk

Following the process as detailed in Figure 3.1, the risk of a collision on the helicopter side will be determined by analysing the chance and the effect of this collision. The analysis of the chance of the impact is completed based on the relative size of each helicopter external component and based on recorded bird strikes as described in the first subparagraph. In the second subparagraph, the consequence of damage based on the (flight) criticality of the helicopter part is determined. In the third subparagraph, the chance and the effect for each helicopter impact location are combined to determine the level of risk. A general layout of the helicopter's exterior parts is depicted in Figure 3.3. This Bell UH-1 lay-out is representative for a, at the time of completing this research, conventional helicopter with a single main rotor and a tail rotor countering the torque effect of the main rotor.
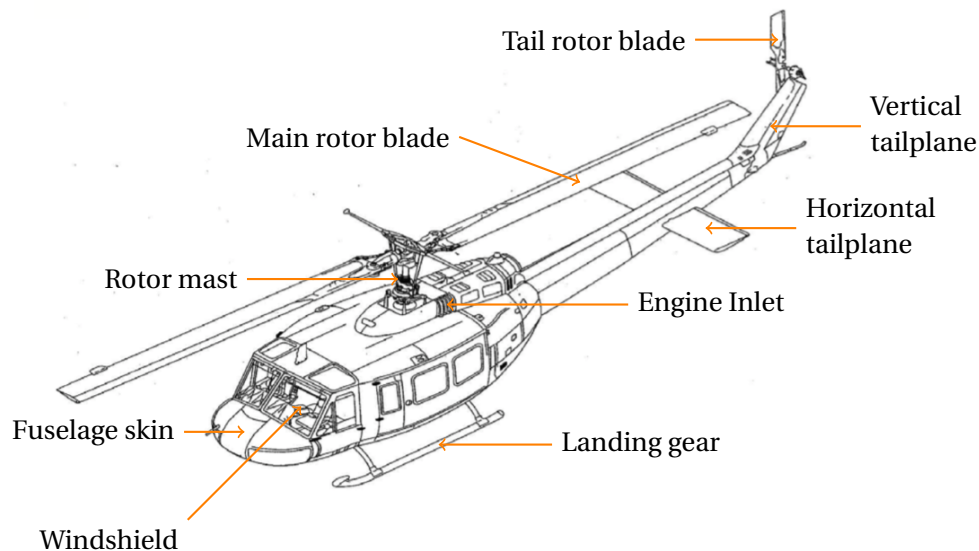
Figure 3.3: *Helicopter (Bell UH-1) main external components.*

3.2.1. Chance: Impact zone analysis

For each helicopter impact location, as defined in Figure 3.3, the chance of the impact should be determined to define the level of risk. Thus far (March 2020), 23 suspected and confirmed UAS collisions with aircraft have been reported world wide, 6 of which included helicopters (Aviation Safety Network Drone Database, 2020). Therefore a statistical analysis of UAS strikes on helicopters to determine the probability of impact cannot be applied at this stage. Two separate analysis methods will be presented below to quantitatively assess the chance.

Rattanagraikanakorn et al. (2018) performed a theoretical analysis for primary impacts to determine the impact chance for different impact zone locations. For each of this location, the surface area relative to the total frontal area of the rotorcraft is estimated and presented as a percentage. Based on the number of newly build aircraft deliveries in the past years, the following five rotorcraft models were analysed in the report: Robinson R44, Sikorsky UH-60 Blackhawk, Airbus H145, Airbus H125 and Bell 407GXP. Results of each of these models have been averaged and this average is shown in the second column of Table 3.5.

A different approach would be to use bird strike data, since the number of bird strikes suffices to perform statistical analysis. Albeit that there are clear differences between UAS and birds such as the fact that UAS are human-operated and fly a different flight path, the bird strike historical data does provide an insight in the likelihood of an impact for the various impact locations. The Aviation Rulemaking Advisory Committee (ARAC, 2017) analysed all reported bird strikes in the United States between January 1990 and February 2016. The result of their impact location analysis on Part 27 rotorcraft is presented in the fourth column of Table 3.5.

Impact chances exceeding 30% have been categorized into the level of probable and the possible chance level applies to percentages between 5 and 30%. Chances less than 5% are classified as improbable. The results for each analysis method are presented in respectively the third and fifth column of Table 3.5. The main difference between the two methods is the (predicted) percentage of impact chance on the main rotor and the windshield. The impact zone location analysis predicts by a considerable margin that the highest chance of impact is on the main rotor, whilst most of the actual recorded bird strikes were windshield impacts. The quantitative thresholds, as defined above, for the three levels of chance result in a different chance level for these two impact locations when comparing the two methods. The cause of this difference can potentially be pointed to the fact that the impact zone analysis is completed based on the frontal view of an aircraft parked on the ground.

Table 3.5: *Helicopter impact location chance analysis.*

Impact location	Frontal area analysis[1]		Bird hit analysis[2]	
	Percentage	Chance level	Percentage	Chance level
Fuselage skin	21.2	Possible	25.7	Possible
Windshield	13.9	Possible	36.2	Probable
Landing gear	1.61	Improbable	1.36	Improbable
Engine inlet	1.76	Improbable	1.30	Improbable
Rotor mast	0.35	Improbable		
Main rotor blade	57.9	Probable	22.7	Possible
Horizontal tailplane	1.20	Improbable		
Vertical tailplane	1.40	Improbable	3.28	Improbable
Tail rotor blade	0.35	Improbable		

[1] Rattanagraikanakorn et al. (2018).
[2] ARAC (2017), note that 9.42% strikes were recorded on other components.

In contrary, most of the bird hits have been recorded en route (ARAC, 2017) at which the aircraft has a different pitch attitude and thereby different exposed frontal area of the windshield and of the rotor disk. The results of both of the methods will be used in the remained of the risk analysis.

3.2.2. Effect: Impact location criticality

Damage to an engine inlet leading to an engine failure would have a more significant consequence on flight safety compared to for example a damaged navigation light. The effect of certain damage on flight safety is therefore dependent on the criticality of the damaged part. In this paragraph, a qualitative assessment will be made to assign an effect level to each helicopter impact location. To determine the criticality of each helicopter impact location, as defined in Figure 3.3, the first step is to review what EASA and the FAA defined as the criticality of a part.

EASA and the FAA share the same view on the prerequisites for a part being a critical one. EASA has detailed these prerequisites in their certification requirements for small, CS 27.602 (EASA, 2018a), and large rotorcraft, CS 29.602 (EASA, 2018b). In an equal manner, the FAA has prescribed the information in the 14 CFR §27.602 (FAA, 2019a) for normal and §29.602 (FAA, 2019b) for transport category rotorcraft. The definition of a critical part in these regulations is as follows: *"A critical part is a part, the failure of which could have a catastrophic effect upon the rotorcraft, and for which critical characteristics have been identified which must be controlled to ensure the required level of integrity."* More detail has been provided in the FAA's Advisory Circulars (ACs) (FAA, 2018a and 2018b), which state: *"Critical part requirements apply to structural components, rotor drive systems, rotors, and mechanical control systems."*

Following these guidelines, the main rotor blade, rotor mast and tail rotor blade are per definition critical items. These parts have therefore been categorized into the catastrophic effect level.

Table 3.6: *Helicopter impact location effect analysis.*

Impact location	Critical item	Catastrophic potential	Effect level
Fuselage skin	No	No	Negligible
Windshield	No	Yes	Moderate
Landing gear	No	Yes	Moderate
Engine inlet	No	A/C dependent	Moderate
Rotor mast	Yes	N/R	Catastrophic
Main rotor blade	Yes	N/R	Catastrophic
Horizontal tailplane	A/C dependent	N/R	Catastrophic
Vertical tailplane	A/C dependent	N/R	Catastrophic
Tail rotor blade	Yes	N/R	Catastrophic

An SA 365N Dauphin 2 landed uneventful after both sides of the horizontal stabilizer and both the vertical fins ruptured (Accident Investigation Board Norway, 2005). For other aircraft, this damage could lead to loss of control of the helicopter and accompanying loss of the aircraft and its occupants. Whether the horizontal and vertical tailplane are critical items, is therefore aircraft dependent. Taking a conservative approach, the horizontal and vertical tailplane have been assigned a catastrophic effect level.

A shattered windshield itself would not result in loss of control of the aircraft. However in case the UAS would penetrate the windshield, the pilot can be injured or disorientated. Flight safety can be compromised under these circumstances. An engine ingestion could lead to an engine failure, which for a single engine aircraft results in an autorotative landing. A poorly executed autorotative landing or collision with ground obstacles could lead to loss of aircraft and aircrew. For a dual engine aircraft, the pilot should always manoeuvre the aircraft such that a successful landing can be performed or continued flight is possible after an engine failure. The effect of an engine ingestion is therefore aircraft dependent. Structural damage to the landing gear would not change the flight characteristics of the aircraft. However during a landing, the helicopter could roll over leading to loss of the aircraft and potentially fatalities. The windshield, engine inlet and landing gear are not critical parts, however, damage to these items could under certain circumstances have a catastrophic outcome. Therefore, the effect of these parts has been categorized as moderate.

At the front of the aircraft, the fuselage skin covers the nose of the helicopter. Generally the aviation systems of the cockpit are installed in this area. Damage to these systems would not directly result in a loss of aircraft control. The fuselage skin effect level can therefore be categorized as negligible. An overview of the criticality analysis for each helicopter impact location is provided in Table 3.6.

Table 3.7: *Risk matrix helicopter impact location based on frontal size.*

		Effect		
		Negligible	Moderate	Catastrophic
Chance	Probable			Main rotor blade
	Possible	Fuselage skin	Windshield	
	Improbable		Engine inlet Horizontal tailplane Vertical tailplane Landing gear	Tail rotor blade Rotor mast

Table 3.8: *Risk matrix helicopter impact location based on recorded bird hits.*

		Effect		
		Negligible	Moderate	Catastrophic
Chance	Probable		Windshield	
	Possible	Fuselage skin		Main rotor blade
	Improbable		Engine inlet Landing gear	Tail empennage

3.2.3. Risk overview

The level of risk for each helicopter exterior part can be determined by combining the chance levels from Table 3.5 and effect levels of Table 3.6 into the risk matrix as defined in Table 3.1. Since two methods of analysing the chance levels have been used, two risk matrices can be constructed. The risk matrix based on the relative impact zone size is presented in Table 3.7 and the matrix based on recorded bird hits is shown in Table 3.8. An impact on the windshield is categorized as a medium risk for both the methods. The methods differ in the identified category for the main rotor, namely a high risk for the relative size of the impact zone analysis and medium for the bird strike analysis. This discrepancy is caused by the fact that different levels of chance are assigned for these methods. For both methods, all other impact locations pose a low risk.

3.3. Conclusion

The aim of this risk analysis was to determine the collision in terms of helicopter impact location and type of UAS that poses the highest risk to the helicopter operator. As analysed in Paragraph 3.1 and shown in the risk matrix of the UAS operations in Table 3.4, UAS operations in the category with a MTOW between 250 g and 25 kg pose the highest risk to the helicopter operator. This analysis is based on a qualitative assessment of the different UAS regulations leading to the chance levels. The kinetic energy of the different UAS categories was the quantitative measure for the different effect levels. For the helicopter impact location, the analysis has been completed in Paragraph 3.2 and the risk matrix for each helicopter impact location is shown in Table 3.7 for the analysis of the relative impact zone size and in Table 3.8 for the bird strike analysis. Regardless of the method used to determine the chance level, an impact on a main rotor blade or onto the windshield are the only two impact locations that have a risk exceeding the low category. In this analysis, the impact location chance was based on a quantitative analysis based on the relative impact zone size analysis and recorded bird strikes. A qualitative distinction between the (flight) criticality of each helicopter impact location led to the effect level.

The second research question, refer to Paragraph 1.2, was defined as follows:

Which impact, in terms of impact location on the helicopter and the type of UAS involved in the collision, poses the highest risk to the helicopter operator?

Based on the results of this chapter, the answer to this question is an impact of a UAS with a MTOW between 250 g and 25 kg onto the windshield or main rotor blade of the helicopter. In the remainder of this thesis, the impact between a UAS within this category and these helicopter components should therefore be modelled. Due to the complexity of accurately modelling a main rotor blade and the limited time available, it was decided to model only the impact onto the windshield within this study. It is recommended to conduct further research to also model a UAS colliding onto a main rotor blade to predict the sustained damage.

<div align="right">4</div>

UAS FE model

As analysed in Chapter 3, UAS with a MTOW between 250 g and 25 kg pose the highest risk to the helicopter operator. Up to the 31st of October 2017, 49% of the top 30 registered non-hobbyist UAS in the United States was of the DJI Phantom family (Gettinger and Michel, 2017). The UAS within this family are all quadcopters and have a MTOW within the UAS category posing the highest risk. Since an accurate Computer Aided Design (CAD) model and results of component level validation tests of the DJI Phantom III were freely available, this UAS out of the Phantom family was selected for impacting the helicopter parts in this study. How an accurate and validated FE model of a UAS could be made, was asked for in the first part of the third research question. To provide the reader with an answer to this question, this chapter covers the process of how the FE model of this UAS is made.

In the first paragraph, details are included on how the geometry of the UAS was established. The FE model was then constructed by meshing this geometry in the second paragraph, selecting the element type for each component in the third paragraph and assigning the respective material models in the fourth paragraph. For the critical components of the UAS, i.e. the battery, motors, and camera, validation tests have been performed as described in paragraph five. At that stage, the only unknown was the appropriate shell thickness for the main body. The process of determining this thickness is included in the sixth paragraph. This chapter is summarized in the last paragraph in which an answer is given to the first part of the third research question. Additional details on construction of the UAS FE model are incorporated in Appendix A and B.

4.1. Geometry

A CAD model of the DJI Phantom III, as shown in Figure 4.1, was available in the free CAD library of GrabCAD.com (2015). This model included the external components of the Phantom III, therefore not incorporating the internal components such as the battery pack and circuit boards. To verify whether the geometry of the CAD model was accurate, a comparison between the dimensions of the actual UAS and the CAD model was made, as shown in Figure 4.2. The main body of the CAD model was relatively 0.3% wider than the actual UAS. The width of the landing gear, length of the landing gear and height of the CAD model was respectively 1.6, 0.7, and 2.4% smaller in size compared to the actual UAS. Due to the small relative difference (max 2.4%) between these dimensions, it was concluded that the CAD model matched the geometry of the actual UAS sufficiently close for the purpose of this research. Additionally, it was assumed that the geometry of the other UAS parts of the CAD model, such as the camera and motors, also closely matched the dimensions of the actual UAS.

Compared to the actual UAS, some internal components such as the circuit boards were omitted when creating the geometry which formed the basis for the FE mesh. Inside the main body only the battery was included. The mass of the omitted components was added to the nodes of the main body as non-structural mass via the LS Dyna *ELEMENT_MASS function. Due to unavailability of an accurate representation of the battery including casing, the battery was simplified to a homogeneous box omitting the presence of the casing, refer to Figure 4.3a. In addition, the camera was simplified to a homogeneous geometry of the casing only, therefore not considering the internal

<div align="center">25</div>

Figure 4.1: *DJI Phantom III CAD model (GrabCAD, 2015).*
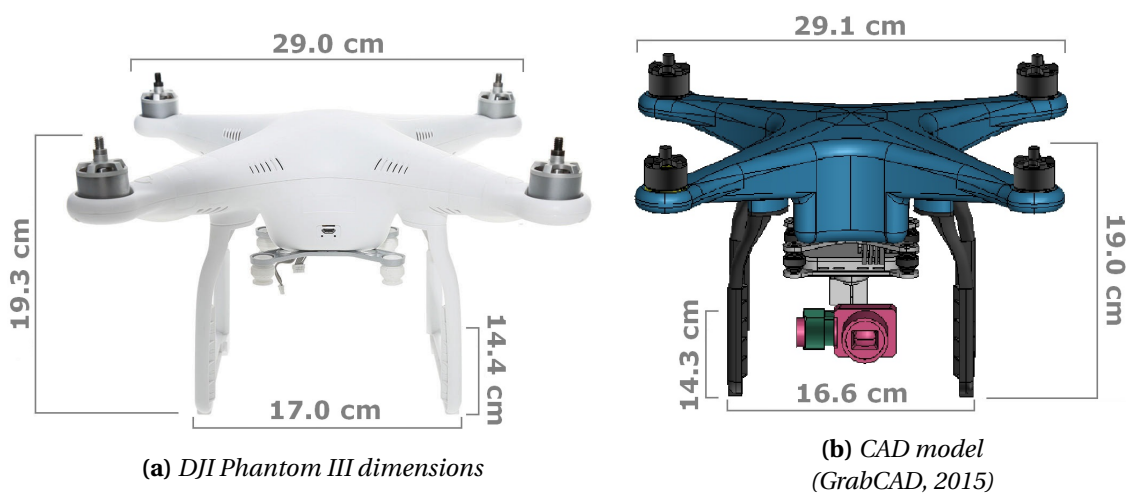
(a) *DJI Phantom III dimensions*

(b) *CAD model (GrabCAD, 2015)*

Figure 4.2: *DJI Phantom III CAD model verification.*

(a) *Battery*

(b) *FEM Mesh*
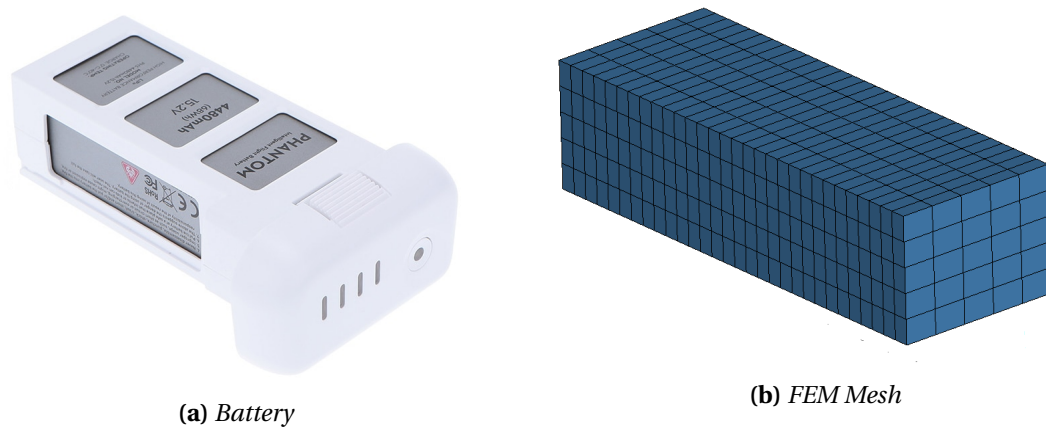
Figure 4.3: *Battery mesh.*

components and structure of the camera. The mass of these internal components were also added to the nodes of the camera as non-structural mass via the *ELEMENT_MASS function to match the weight as measured in the validation tests in Table B.1.

4.2. Mesh

To determine the appropriate mesh size for each component of the DJI Phantom III, a mesh sensitivity analysis has been conducted. For the purpose of this test, multiple mesh sizes of these components have been used in the simulations. The mesh size with the most optimal compromise between result accuracy and computational time required has been selected. More detail to the analysis and results of this mesh sensitivity analysis is presented in Appendix A.

As analysed in Paragraph A.1, the most accurate results for the battery were expected when the front side was meshed into 5×5 elements with 30 elements along the length of the battery. This resulted in each element having a size of 9.1×6.8×4.3 mm. An image of the actual battery of the DJI Phantom III and the mesh of this battery as used in the simulations is shown in Figure 4.3.

Due to the geometrical features of the motor, the automatic solid mesher of LS Dyna was the only means of meshing this geometry. The default average element size was required to be set to 2 mm, since otherwise the PrePost processor issued an error. The CAD model geometry as well as the mesh of the motor is shown in Figure 4.4. The rotor and stator of the motor were incorporated as separate parts.

Similarly to the mesher for the motor, only the automatic solid mesher of LS Dyna could accurately mesh the geometry of the camera. In the mesh sensitivity analysis, as presented in Paragraph A.3, the default average element size of 8 mm was selected. This element size resulted in accurate results whilst remaining computational efficient. The motor's CAD model geometry as well as the mesh with the selected default setting is shown in Figure 4.4.

Since the geometry of the main body and the rotor blades would be modelled with shell elements, the 2D automatic mesher of the LS Dyna PrePost processor was the appropriate means to mesh the CAD model geometry. As presented in the mesh sensitivity analysis, refer to Paragraph A.4, a default element size of 8 mm provided converged results whilst maintaining computationally efficient. The main body CAD geometry as well as the FEM mesh are presented in Figure 4.6. In the mesh sensitivity analysis of the main body, it was analysed that the coarsest mesh was the most appropriate choice. In a similar manner, the coarsest mesh that could be made by the PrePost processor without issuing an error was selected for the camera gimbal. This was the case for a default element size of 5 mm for this part. The CAD model geometry as well as the FE mesh of the camera gimbal are presented in Figure 4.7.

(a) *CAD model*
(GrabCAD, 2015)

(b) *FEM Mesh*

Figure 4.4: *Motor mesh.*

(a) *CAD model*
(GrabCAD, 2015)
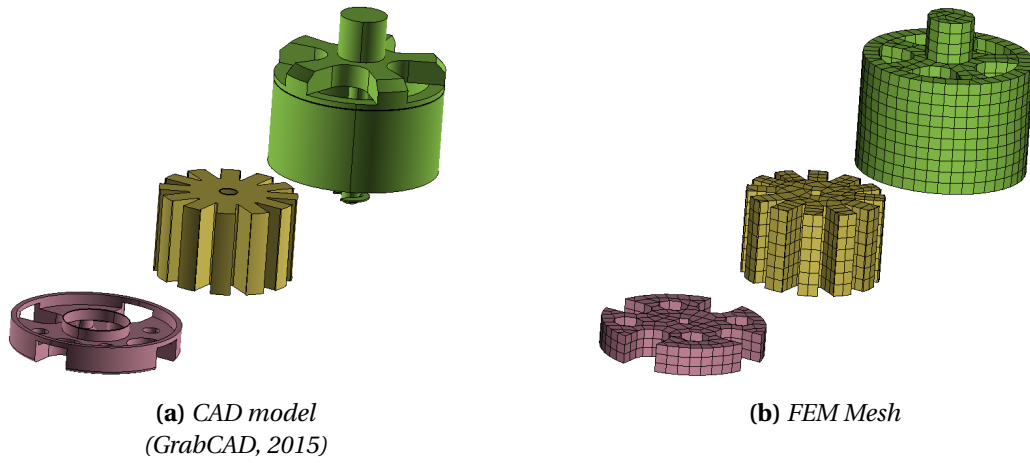
(b) *FEM Mesh*

Figure 4.5: *Camera mesh.*

(a) *CAD model*
(GrabCAD, 2015)
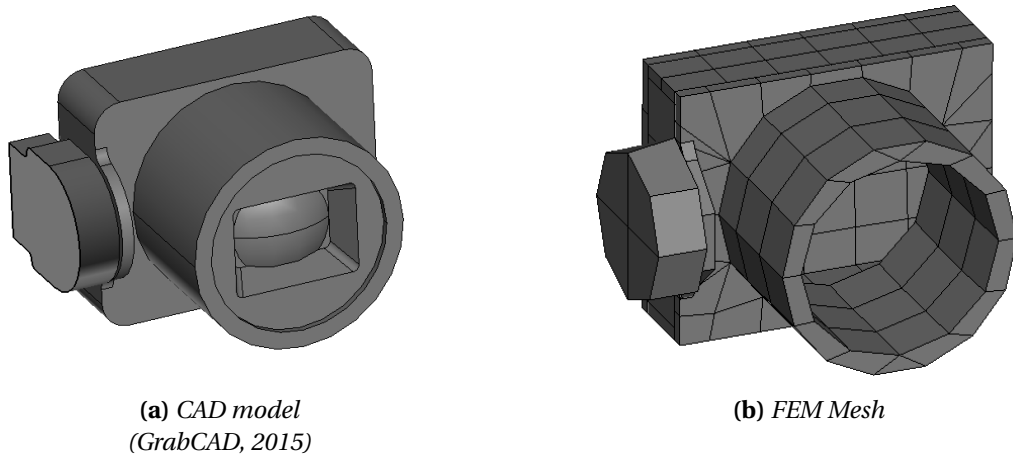
(b) *FEM Mesh*
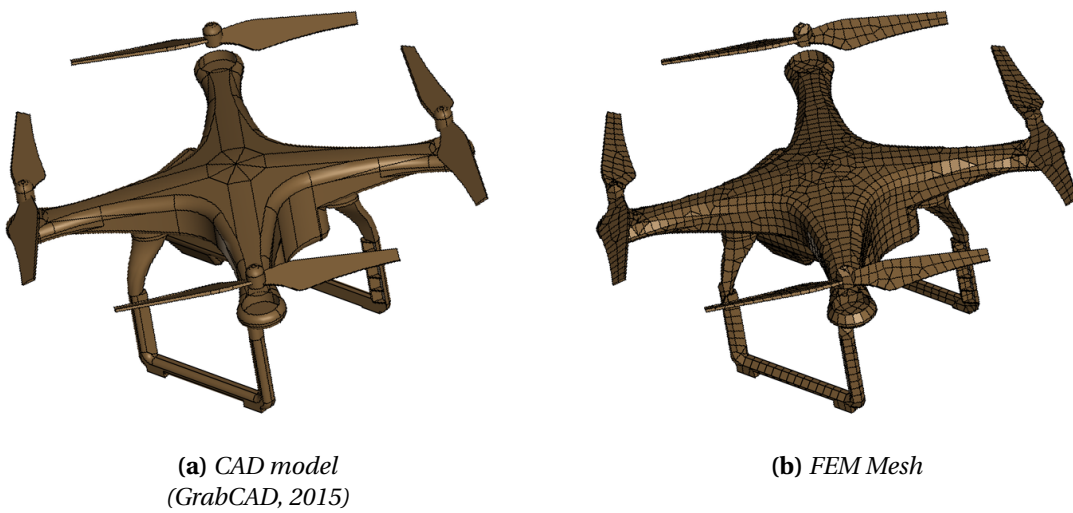
Figure 4.6: *Main body and propellers mesh.*

(a) *CAD model*
(GrabCAD, 2015)

(b) *FEM Mesh*
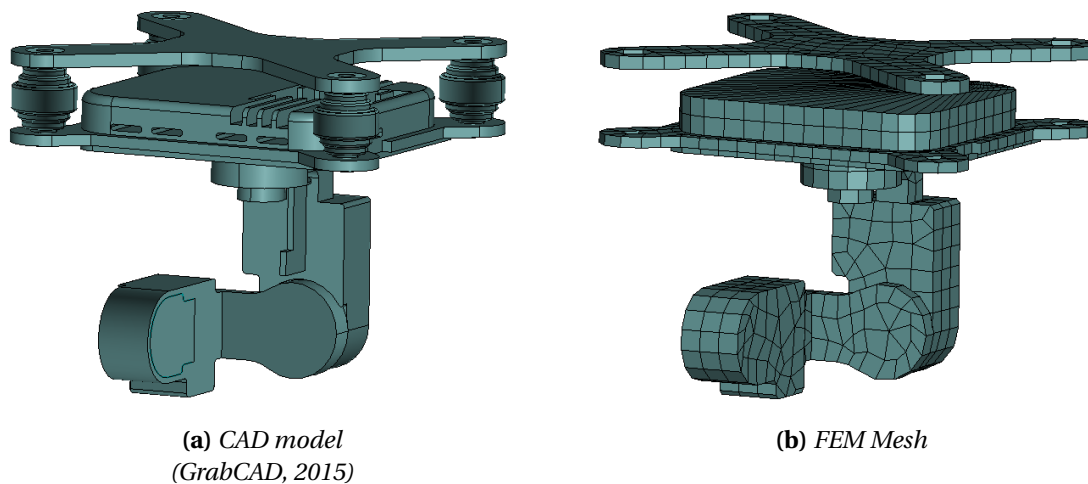
Figure 4.7: *Camera gimbal mesh.*

4.3. Element types

Drumond, Greco, and Cimini (2019) investigated that the DJI Phantom III battery, motors, and camera were the most critical parts during an impact. Considering that the structure of these parts was of a bulk type, 3D solid elements were selected for these components. The selected element formulation was the type 2 fully integrated selectively reduced (LSTC, 2018a). The advantage of this element type is that hourglassing is eliminated.

The camera gimbal was also a bulk type part, therefore requiring 3D solid elements. However, this part was not considered a critical component by Drumond, Greco, and Cimini (2019). Therefore, constant stress solid elements with formulation type 1 was selected to represent this component. This would reduce the computational time required in comparison with the more costly type 2 fully integrated element type of the critical components at potentially the cost of accuracy.

Since the main body and rotors of the DJI Phantom III were thin-walled, the structure was modelled using 2D shell elements. For this purpose, the LS Dyna type 16 shell element formulation was selected. This element type was a fully integrated shell element, therefore inherently eliminating hourglassing (LSTC, 2018a). The shear value of this element type was set to 5/6 and the number of through shell thickness integration points to 2, which were both the LS Dyna default values.

4.4. Material models

The DJI Phantom III main components were made out of the following materials:

– the main body and the camera gimbal were constructed out of polycarbonate;
– the power-pack was a lithium-ion polymer battery;
– the motors had an aluminium alloy A520.0-F rotor and an AISI 4130 steel core stator;
– the camera casing was made out of aluminium alloy A520.0-F.

The material properties of the aluminium alloy A520.0-F and the AISI 4130 steel alloy have been obtained from the Metallic Materials Properties Development and Standardization (MMPDS) database (2014) and are presented in Table 4.1. The *MAT_PIECEWISE_LINEAR_ PLASTICIY card has been used to model these materials (*MAT_024, LSTC, 2018b). This LS Dyna material type is an elasto-plastic model with an arbitrary stress strain curve. In this case, a tangent modulus (E_t) was defined, making the stress strain relationship bilinear. Although strain rate dependency can be defined in this material card, this was not incorporated to model these materials.

Table 4.1: *Metallic material properties (MMPDS, 2014).*

Material Property	Symbol	A520.0-F	AISI 4130	Unit
Density	ρ	2600	7850	kg/m^3
Modulus of Elasticity	E	66	200	GPa
Poisson's Ratio	ν	0.33	0.32	-
Yield Stress	σ_y	170	483	MPa
Tangent modulus	E_t	1164	1174	MPa
Failure strain	ϵ_{max}	0.14	0.12	-

The power source of the DJI Phantom III was a lithium-ion polymer battery. Sahraei, Meier and Wierzbicki (2014) performed experiments to determine the mechanical behaviour of different types of lithium-ion pouch cells. The material properties of the medium-sized pouch cells, applicable to the battery of this UAS, are listed in Table 4.2. In this study, the LS Dyna material card *MAT_CRUSHABLE_FOAM was selected to model the material (*MAT_063, LSTC, 2018b). An arbitrary load curve defines the yield stress versus volumetric strain in this material model. Tension is elastic-perfectly-plastic at the optional tension cut-off value and unloading is treated fully elastic.

Table 4.2: *Lithium-ion battery material properties (Sahraei, Meier and Wierzbicki, 2014).*

Material Property	Symbol	Value	Unit
Density	ρ	1750	kg/m^3
Modulus of Elasticity	E	500	GPa
Poisson's Ratio	ν	0.01	–
Compressive Stress	σ	$276 \cdot \epsilon^{1.8}$	MPa
Failure strain	ϵ_{max}	0.16	-
Tensile cut off	Y_t	30	MPa

For the polycarbonate, Meng et al. (2018) consulted the manufacturer of the Phantom III, DJI Technology Co. Ltd., to obtain the material properties. Subsequently the failure strain was modified through comparison with available test data. The material properties are listed in Table 4.3. In their research, the material was represented by an elastic-plastic model with ideal plasticity. The *MAT_PLASTIC_KINEMATIC LS Dyna card (*MAT_003, LSTC, 2018b) can model isotropic and kinematic hardening plasticity and has the option of including rate effects. However, it can also be configured to represent an elastic-plastic model with ideal plasticity as required in this case. The material card is suitable for solid (camera gimbal) as well as shell elements (main body, landing gear, and propellers).

Table 4.3: *Polycarbonate material properties (Meng et al., 2018).*

Material Property	Symbol	Value	Unit
Density	ρ	1180	kg/m^3
Modulus of Elasticity	E	2.35	GPa
Poisson's Ratio	ν	0.3	-
Yield Stress	σ_y	62	MPa
Failure strain	ϵ_{max}	0.2	-

For all the material models, the failure strain has been included in the respective material model by adding a criterion of element erosion through the LS Dyna *MAT_ADD_EROSION option. Once the failure strain is satisfied, the element is deleted from the calculation.

4.5. Validation tests

In the research of Drumond, Greco, and Cimini (2019) and of Olivares et al. (2017), it was identified that the critical components of the UAS were the motors, the battery, and the camera. Therefore in the research of the latter, these components were selected to perform ballistic tests for validation purposes. Each component was impacted against an aluminium flat plate by means of a compressed gas gun system. The results of these tests were reported in detail in the research paper and provided the basis for the validation process in this study.

To validate the DJI Phantom III FE model, created as described previously in this chapter, multiple validation tests simulating the ballistic tests of Olivares et al. (2017) were completed. The experimental and simulation set-up as well as the validation process for each critical component of the UAS is detailed in Appendix B. In summary, the motor and camera showed a strong correlation with the ballistic test results. For the battery, the initial deformation was accurately captured, however, the deformations thereafter were initially over predicted and subsequently under predicted. This will be taken into account when analysing the results in the remainder of this research. Recommendations to improve the model of the battery were to incorporate the casing of the battery or to change the numerical mesh into for example an SPH formulation. Additionally, strain softening could be introduced to reduce the distinct peak in the initial deformation in the simulation, since this peak is not present in the actual test results.

4.6. Main body shell thickness analysis

After loading the CAD model of the UAS into the PrePost processor of LS Dyna, the geometry of the 3D bulk components was established. The (shell-)thickness of the 2D representation of the main body however was unknown. In order to determine the appropriate thickness of the shell elements of the main body and propellers, a sensitivity analysis of this shell thickness was performed as detailed below.

As presented in Table B.1, during the validation tests of Olivares et al, (2017) each component was weighed prior to the impact. On average the mass of the battery was 346.89 g, of the motor 51.03 g and of the camera 52.74 g. The weight of the camera gimbal could be established by assigning the polycarbonate material properties, as defined in Table 4.3, to the 3D gimbal geometry and subsequently measuring the mass in LS Dyna. The mass of the gimbal was measured at 108.48 g. The mass of all the components, apart from the main body and the omitted internal components (refer to Paragraph 4.1), was added and measured approximately 708 g. The total mass of the DJI Phantom
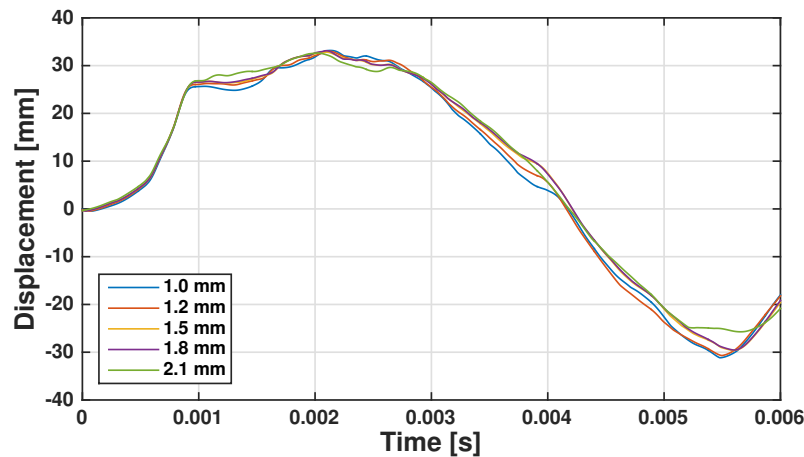
Figure 4.8: *Center plate deformation over time for the various main body shell thicknesses.*

III was 1216 g as stated in the user manual (DJI Technology Co., 2017). This resulted in that 508 g remained available to represent the main body and the mass of the omitted internal components in the FE model.

To determine how the shell thickness would affect the expected damage after an impact, tests for various thicknesses of the 2D shell elements of the main body and propellers have been performed. The main body shell with the propellers was impacted at a velocity of 129 m/s onto the center of a 1.6 mm thick aluminium plate, similar to the plate as detailed in Paragraph B.1. For each shell thickness, the total mass of the body was set to 508 g through the LS Dyna *ELEMENT_MASS function. This function measured the structural mass of the component and added non-structural mass to the nodes to ensure that the total mass was equal to the set value. The maximum feasible shell thickness was 2.1 mm, since the weight of the main body would then be 490 g. Increasing the thickness further would result in the weight of the UAS in the simulation exceeding the weight of the actual UAS. The tests have been performed for a shell thickness of 1.0, 1.2, 1.5, 1.8, and 2.1 mm.

The deflection of the center of the target plate during the impact for all the tested plate thicknesses is presented in Figure 4.8. As shown in this figure, the plate deflection was almost exactly equal (max 8% relative difference at 1.4 ms) throughout the test period for the various plate thicknesses of the main body. Therefore, it can be concluded that the effect of the plate thickness is negligible. Only the mass should be matched to 508 g, such that the total mass of the UAS corresponds to the mass of the actual DJI Phantom III. In the remainder of the simulations in this research, the shell thickness is set to 1.5 mm.

4.7. Conclusion

In line with the aim of this chapter, a detailed description was provided on how the FE model of the DJI Phantom III was made. With this description, the first part of the third research question can be answered:

How can an accurate and validated model of the UAS be made in explicit Finite Element software?

In summary the model was made follows. An accurate CAD model of the DJI Phantom III from Grab-CAD.com (2015) was imported into the LS Dyna PrePost processor. To select the appropriate mesh size for each UAS component, a mesh sensitivity analysis was performed (Appendix A). The critical components have been modelled using 3D fully integrated solid elements, whilst the remaining non-critical bulk component, the camera gimbal, was represented by a 3D constant stress solid element. Since the main body and rotors were thin-walled, a 2D fully integrated shell element was selected. For each component, the properties of the material were incorporated in a material model capable of representing the material behaviour. An overview of the mesh and material features of the FE model is depicted in Figure 4.9. To validate the constructed FE model, a validation process (Appendix B) was performed by comparing the results of the simulations with actual component ballistic tests performed by Olivares et al. (2017). The results of the simulations showed a strong correlation with the test results for the camera and the motor. The initial deformation caused by the battery impact was captured accurately, however, the subsequent deformation in the simulation was initially over predicted and thereafter under predicted. This should be taken into account when analysing the results in the remainder of this research. Recommendations to improve the battery model were to incorporate the battery casing or to select a different numerical mesh such as an SPH formulation. Additionally strain softening could be introduced to more accurately capture the initial displacement peak. Since the shell thickness of the main body and rotors was an unknown, a sensitivity analysis of the effect of various thicknesses was performed. The effect of changing the shell thickness on the deformation of the impacted aluminium plate was negligible, therefore, a shell thickness of 1.5 mm was selected arbitrary.
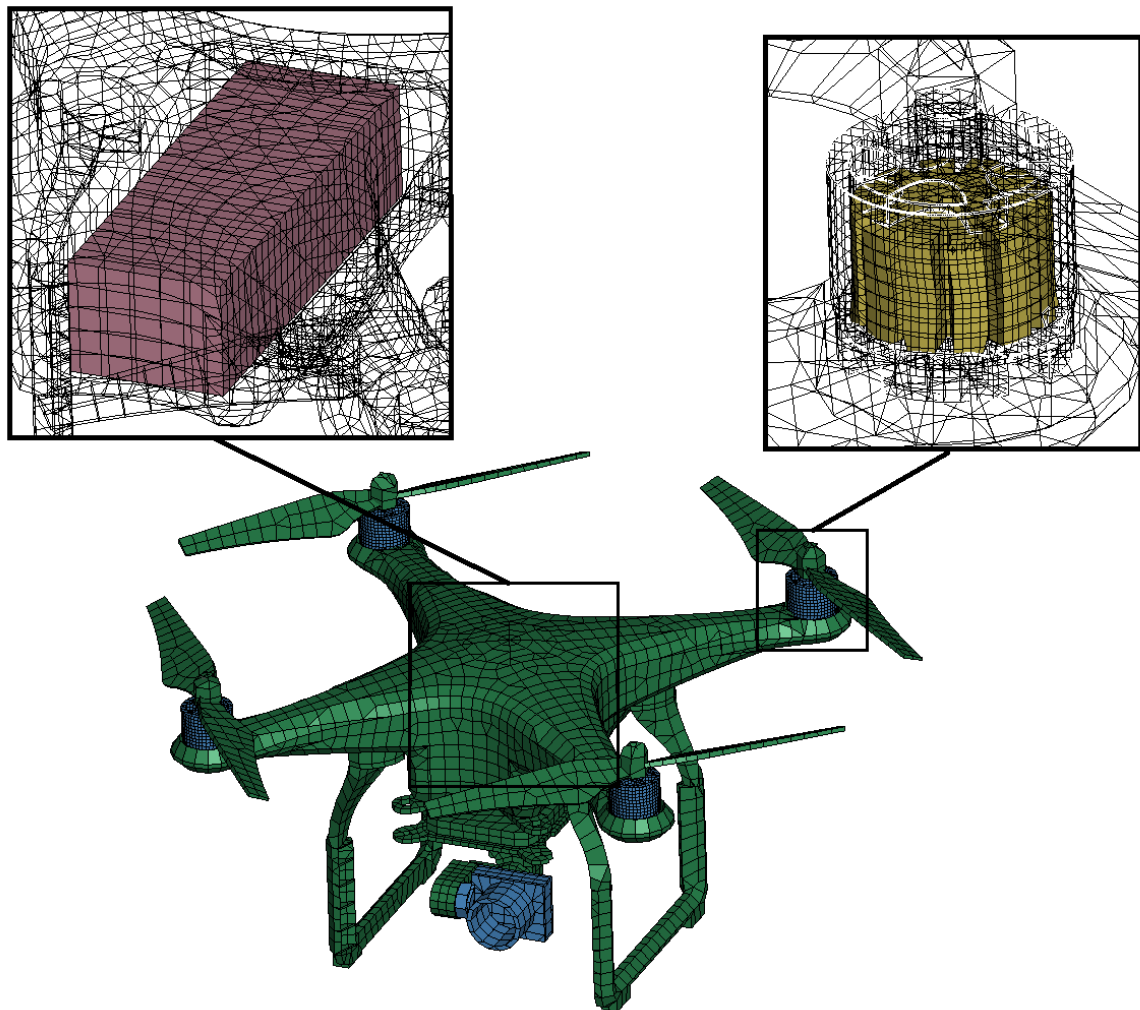
Colour Code	LS Dyna material model	Material
	Plastic Kinematic (*MAT_003)	Polycarbonate (Table 4.3)
	Piecewise Linear Plasticity (*MAT_024)	A520.0-F (Table 4.1)
	Piecewise Linear Plasticity (*MAT_024)	AISI 4130 (Table 4.1)
	Crushable Foam (*MAT_063)	Lithium-ion cells (Table 4.2)

Figure 4.9: *DJI Phantom III FE model overview.*

<div align="right">

5

</div>

Helicopter windshield FE model

The conclusion of the risk analysis in Chapter 3 was that an impact of the UAS onto the main rotor and windshield of the helicopter would pose the highest risk to the helicopter operator. Since creating a windshield model would be less complex compared to creating an accurate model of a helicopter main rotor blade and due to the limited time available, this study encompasses a UAS impact onto a helicopter windshield. The aim of this chapter is therefore to create a representative model of a helicopter windshield to predict the damage after a collision with a UAS. When achieving this aim, the part concerning the FE model of the helicopter impact location in the third research question can be answered.

The Agusta 109 helicopter (A-109) was selected to model a representative helicopter windshield. This selection was based on the fact that its windshield material properties as well as a CAD model of the entire aircraft was freely available. As presented in the literature review in Paragraph 2.4, results of validation tests of windshield bird strikes were not freely available or could not be easily simulated in FE software. Therefore an alternative approach had to be taken to create the windshield FE model, which in the end would result in achieving the research objective. For this purpose, the modelling strategy from Hedeyati et al. (2014) will be used in this chapter. This includes an assessment to determine the minimum thickness of the windshield FE model at which the simulation complies with the prevailing certification requirement.

The geometry of the A-109 windshield extracted from an available CAD model and the accuracy of this geometry is presented in the first paragraph. Subsequently, this geometry was meshed in the second paragraph and appropriate element types and material models were assigned to the part in paragraph three and four. The incorporated boundary conditions in the model is discussed in the fifth paragraph. To determine a representative thickness of the windshield, a brief design process is completed in paragraph six. In this paragraph, a bird strike event was simulated to determine the thickness required to comply with the certification standards. This chapter is summarized in the last paragraph in which the second part of the third research question of this study is answered. Additional details on the simulation of the bird strike events have been incorporated in Appendix C.

5.1. Geometry

A CAD model of the entire A-109 helicopter as shown in Figure 5.1 was available in the free CAD library of GrabCAD.com (2014). Within this study, all impacts were simulated onto the left hand side cockpit window, which is highlighted in orange in the figure. The actual size of the A-109 windshield was not available. Instead, the dimensions of the fuselage of the actual aircraft (EASA, 2013) have been compared with the dimensions of the CAD model to assess whether the geometry of the latter was accurate. The results of this comparison are shown in Figure 5.2.

After scaling the model with a factor of 1.2944 to minimize the relative difference between the two, the width, length and height of the CAD geometry were respectively 1.55, 11.71, and 3.29 m. The actual aircraft measured 1.64 m, 11.45 m, and 3.10 m for these dimensions resulting in a relative difference of +5.8% for the fuselage width, -2.2% for the length, and -5.8% for the height. Due to this relative small maximum difference of 5.8%, the CAD model matched the geometry of the actual aircraft sufficiently close for the purpose of this research. It was assumed that the geometry of
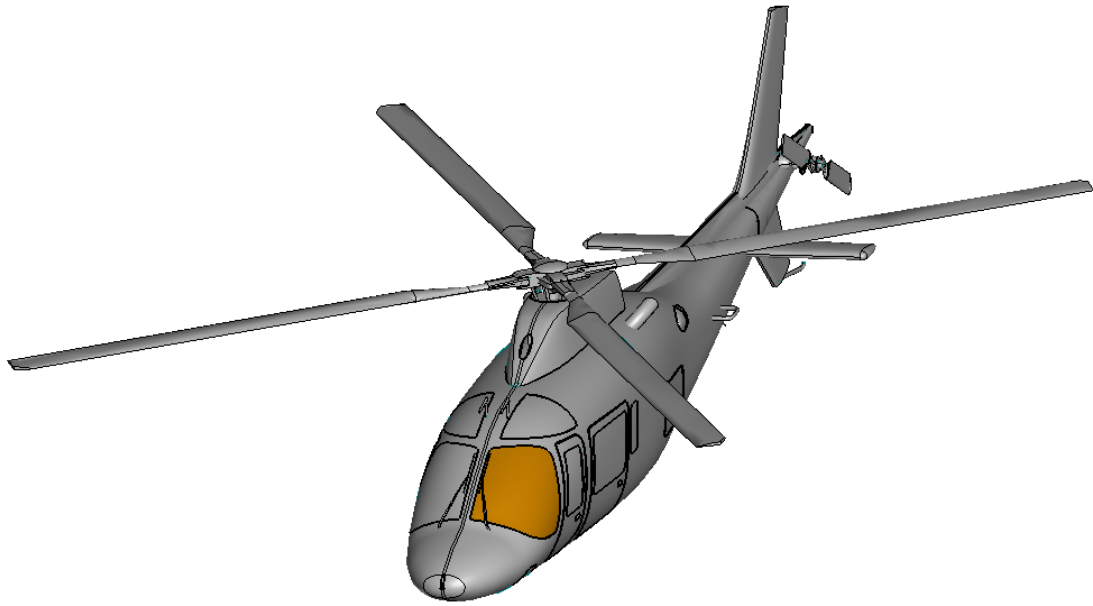
Figure 5.1: *Agusta A-109 CAD model (GrabCAD, 2014).*

the windshield itself would also match the actual windshield with similar accuracy. The surrounding structure was omitted and simplified by adopting boundary conditions as further specified in Paragraph 5.5.

5.2. Mesh

Different mesh sizes of the windshield are required to complete a mesh sensitivity analysis for the UAS impact onto this windshield. Therefore three FE models with a different default average mesh size have been made with the 2D automatic mesher of the PrePost processor as shown in Figure 5.3. This 2D mesher was by default set to mixed mode, which combines quadrilateral and triangular elements depending on the shape of the part to create the mesh. Elements in the three meshes are of similar size compared to the three finest meshes of the target plate as used in the UAS component mesh sensitivity analysis in Appendix A. The mesh with elements of a default size of 7.00 mm is equal to the plate meshed with 128 elements along each edge, 3.50 mm equates to the 256 elements plate and 1.75 mm to the finest mesh of 512 elements. The time step for the windshield is dependent on the mesh size of the smallest element, as explained in Paragraph 2.3.1, and is therefore a measure of the quality of the mesh refinement. For the 7.00 mm mesh, the smallest time step was 1.1 microseconds and for the 3.50 mm and 1.75 mm mesh respectively 745 and 292 nanoseconds. This reduction in time step with decreasing default size of the automatic meshes indicates that the resulting mesh is refined accordingly.

5.3. Element types

The thickness of the helicopter windshield is multiple factors smaller compared to its transverse dimensions. Therefore, 2D shell elements were adopted to represent the windshield. To prevent hourlassing modes, the fully integrated shell element formulation type 16 was selected (LSTC, 2018a). Within this formulation, the user is only required to set values for the thickness of the shell, the shear factor, and the number of through the shell thickness integration points. In this case the LS Dyna default values of respectively 5/6 for the shear factor and 2 for the number of integration points were used. The shell thickness will be set as further detailed in the bird strike analysis Paragraph 5.6.

(a) *A-109 Manual dimensions*[1]
(EASA, 2013)

(b) *Scaled CAD model*
(GrabCAD, 2014)
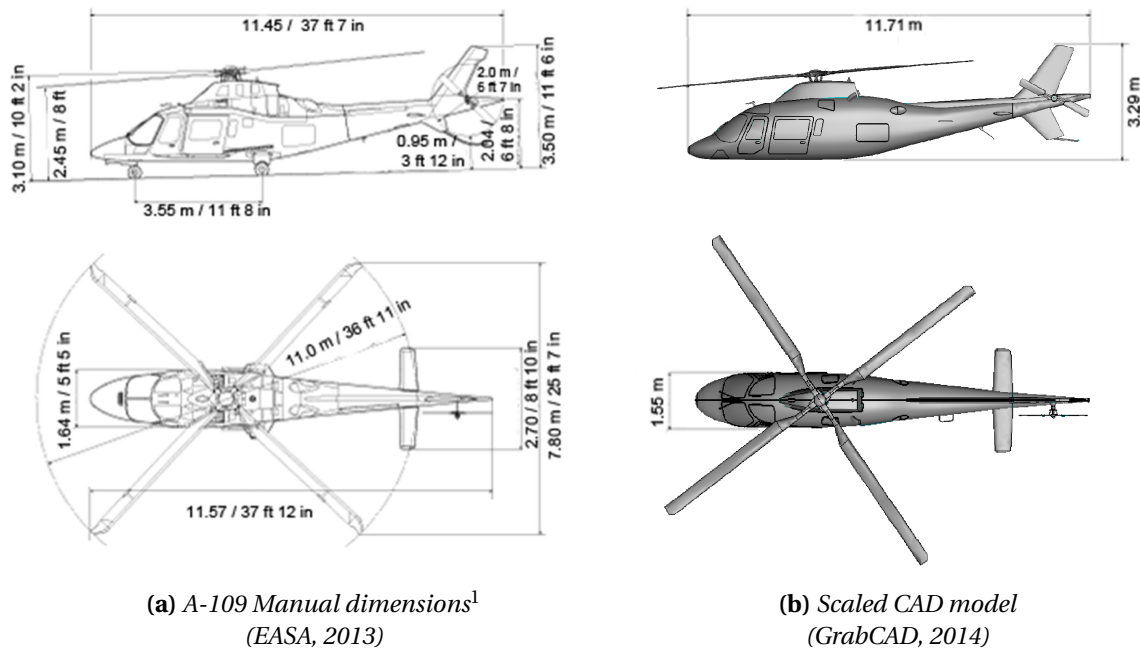
[1] The fuselage ground clearance is 0.40 m.

Figure 5.2: *Agusta A-109 CAD model verification.*

5.4. Material models

Acrylic is a widely used material in aviation for the production of windshields of different types of aircraft. The windshields of the A-109 are also made out of acrylic as reported by the Air Accidents Investigation Branch (AAIB, 2012) after a bird strike event on this aircraft. For their helicopter windshield FE model, Hedeyati et al. (2014) performed a number of tension tests on stretch acrylic to determine the material properties, which are listed in Table 5.1. The results of the tests showed an elastic perfectly plastic response of this material. The LS Dyna *MAT_PLASTIC_KINEMATIC card was selected to represent the stretch acrylic. This material card can model isotropic hardening plasticity including rate effects, but is configured in this case for the elastic perfectly plastic behaviour (*MAT_003, LSTC, 2018b).

Table 5.1: *Stretch acrylic material properties (Hedeyati et al., 2014).*

Material Property	Symbol	Value	Unit
Density	ρ	1180	kg/m^3
Modulus of Elasticity	E	330	GPa
Poisson's Ratio	ν	0.4	-
Yield stress	σ_y	600	MPa
Hardening parameter	β	0.5	-
Failure strain	ϵ_{max}	0.025	-
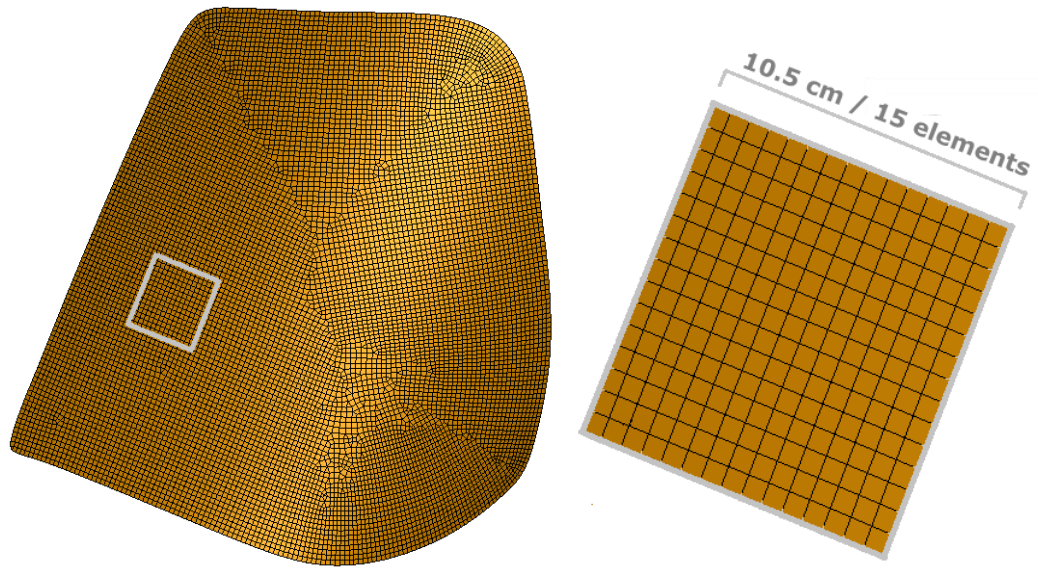
(a) *7.00 mm*
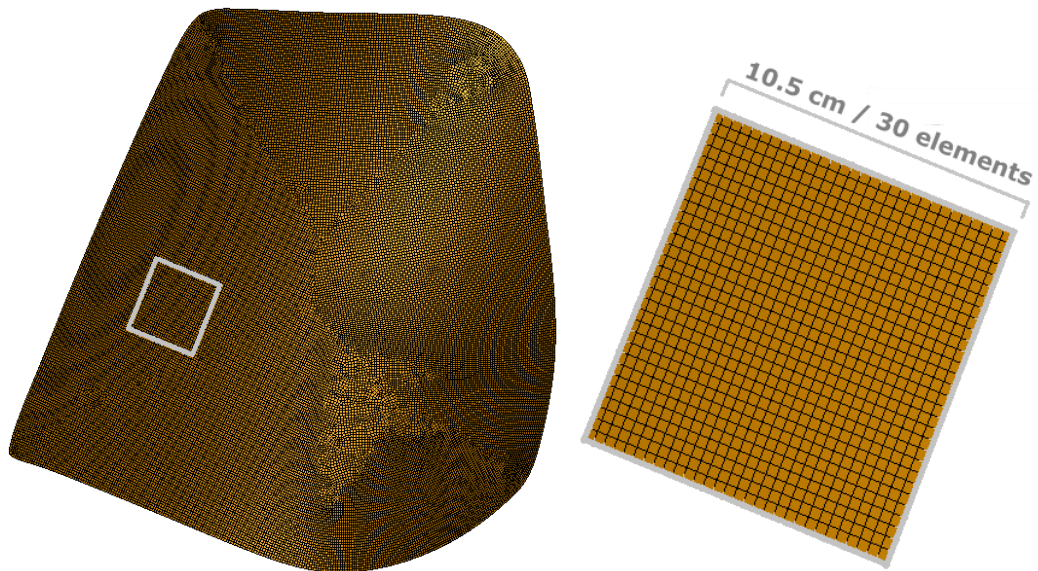
(b) *3.50 mm*
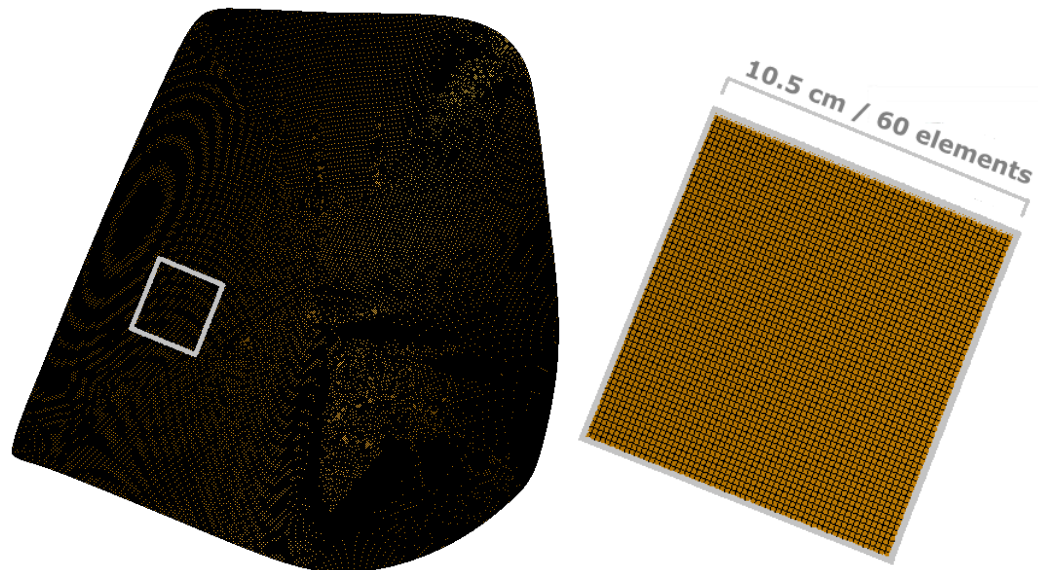
(c) *1.75 mm*

Figure 5.3: *Various windshield mesh sizes.*

Figure 5.4: *Agusta A-109 (Global Aircraft, 2019).*

Strain rate effects were considered by implementing the Cowper-Symonds model, which scales the yield stress as follows (LSTC, 2018b):

$$\frac{\sigma_d}{\sigma_s} = 1 + \left(\frac{\dot{\epsilon}}{C_{cs}}\right)^{1/p}$$

in which σ_d is the dynamic and σ_s the static yield stress. $\dot{\epsilon}$ is the strain rate and C_{cs} and p are the Cowper-Symonds parameters. For the acrylic, values of $C_{cs} = 40\ 1/s$ and $p = 4$ were implemented in the material card.

5.5. Boundary conditions

As analysed in the literature review in Paragraph 2.4, the surrounding framework of the windshield will be omitted since no data for an FE model is available for this structure. Instead, a simplification will be adopted in the windshield model by implementing boundary conditions at the edges of the windshield. As explained in the literature review, it is dependent on the stiffness of the framework whether clamped boundary conditions are appropriate to represent the surrounding structure of the windshield. The mechanical behaviour of the surrounding framework of the A-109 helicopter, as shown in Figure 5.4, is not readily available. Therefore it is unknown which boundary conditions would be appropriate for the A-109 FE model.

Two configurations of boundary conditions for the FE model have been adopted as presented in Figure 5.5 and the results of the various simulations will be compared. In the first configuration, all the edges of the windshield are clamped by restricting the nodal translations and rotations, similar to most of the published literature of rotorcraft windshields (Paragraph 2.4). In the second configuration, the bottom edge of the windshield and the edge adjacent the cockpit door frame are clamped. The surrounding structure of these locations usually has a relatively high stiffness to support for example the cockpit door. At the edge adjacent the right hand cockpit windshield, only translation in the x-direction is restricted. For the edge adjacent the overhead windshield, translation in the y-direction is restricted. This is based on the assumption that during the impact of the windshield, these adjacent windshields would be loaded in tension and thereby provide in-plane stiffness. The assumption could be valid for relatively small deformations, however, for larger deformations, the restriction in translation would not provide realistic results.
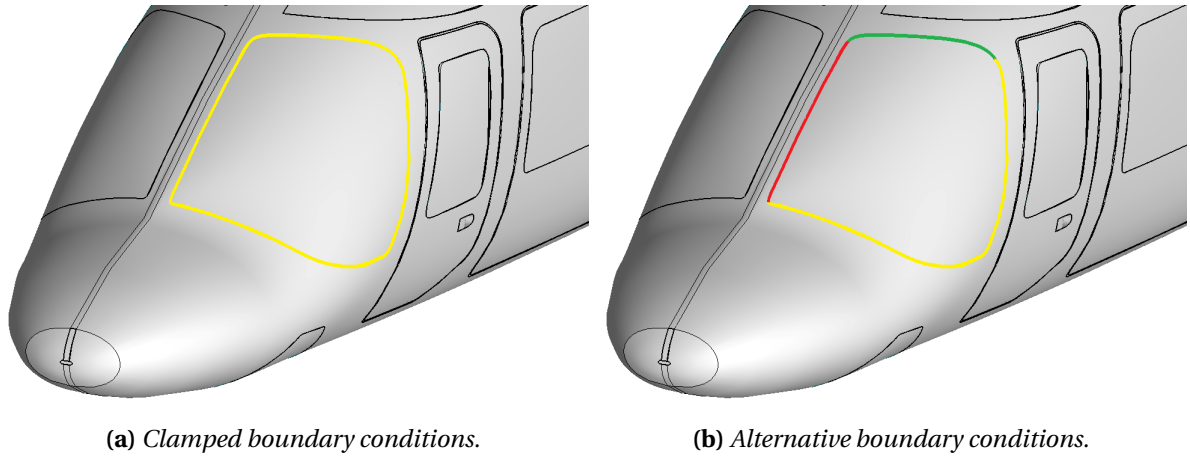
(a) *Clamped boundary conditions.*

(b) *Alternative boundary conditions.*

Linecolor	T_x	T_y	T_z	θ_x	θ_y	θ_z
🟨	0	0	0	0	0	0
🟥	0	1	1	1	1	1
🟩	1	0	1	1	1	1

0 = Constraint degree of freedom, 1 = Unconstraint degree of freedom

Figure 5.5: *Windshield various configurations of boundary conditions.*

To assess whether the alternative boundary conditions would be representative in case the surrounding structure would be relatively flexible, a bird strike event was simulated on a 6.8 mm thick windshield with the boundary conditions as detailed in Figure 5.5b. The set-up for this test was similar to the simulations performed for the bird strike analysis in Appendix C.1. The results of this simulation has been compared with an actual bird strike test on an unknown helicopter as shown in Figure 5.5b (Ramirez, 2014). The propagation of the deflection of the windshield in the simulation shows strong similarities with the actual test. The top of the windshield in both cases moves slightly in a downwards direction whilst the bottom and cockpit door side edges clamp the windshield. The windshield at the edge adjacent the right hand cockpit windshield rotates in a similar fashion inwards around the framework in between the windshields for both tests whilst the center of the windshield moves inwards due to the bird impact.

Since no information is available on the surrounding structure of the windshield of the A-109, it is unknown which configuration of boundary conditions should be adopted to represent the framework. For the remainder of this research, the two configurations of boundary conditions as presented in this paragraph can be used and the results can be compared. To improve the FE model of the windshield, it is recommended to accurately incorporate the surrounding structure, since it would have an effect on the results of the simulations.

(a) *Unknown aircraft type actual test (Ramirez, 2014).*

(b) *Alternative boundary conditions simulation.*
SPH Bird model not shown.
Undeformed surrounding structure shown only for visualization purposes.
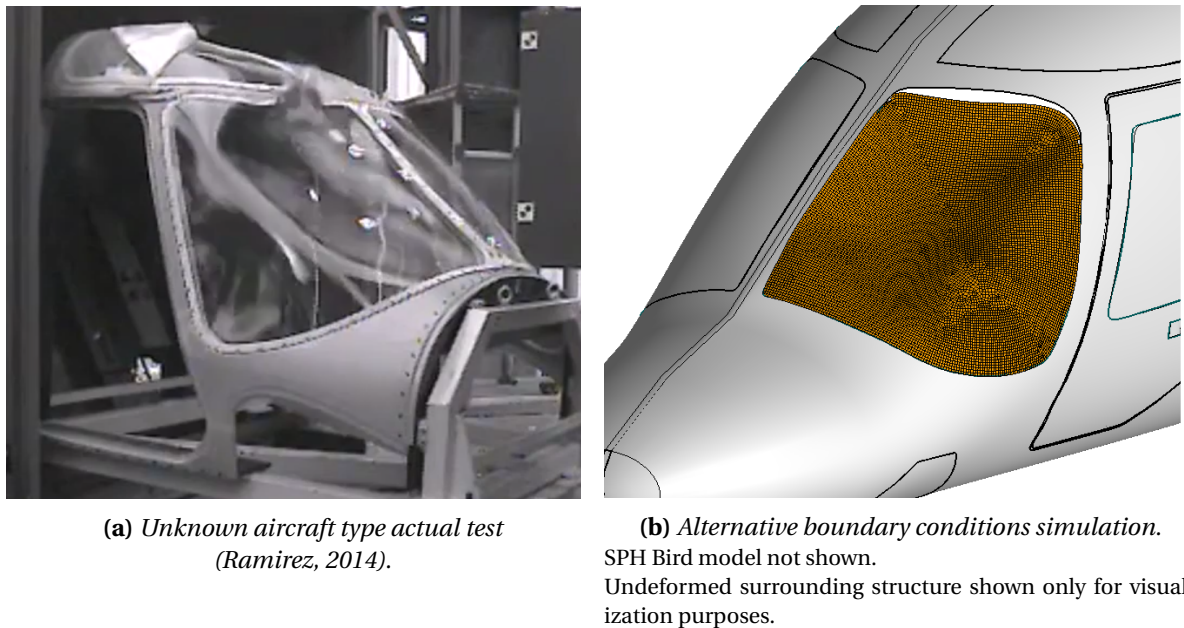
Figure 5.6: *Comparison of an actual bird strike test and a simulation with the alternative boundary conditions.*

5.6. Bird strike analysis

At this stage, the unknown in the model is the thickness of the windshield. Since no validation data of actual bird strike tests was available, the approach as adopted by Hedeyati et al. (2014) will be used. In this report, the minimum thickness was determined at which the windshield would comply with the certification requirements for Part 29 (transport category) rotorcraft. The following certification requirement §29.631 (EASA, 2018b, FAA, 2019b) regarding bird strikes applies to these rotorcraft:

"The rotorcraft must be designed to ensure capability of continued safe flight and landing (for Category A) or safe landing (for Category B) after impact with a 1 kg bird, when the velocity of the rotorcraft (relative to the bird along the flight path of the rotorcraft) is equal to Vne or Vh (whichever is the lesser) at altitudes up to 2438 m (8000 ft). Compliance must be shown by tests, or by analysis based on tests carried out on sufficiently representative structures of similar design."

In addition, the following certification requirement §27-29.775 (EASA, 2018a,f FAA, 2019a) applies to Part 29 as well as to Part 27 (normal category) rotorcraft:

"Windshields and windows must be made of material that will not break into dangerous fragments."

The maximum cruising velocity of the A-109 is 156 kts (Leonardo Helicopters, 2020), which equates to 80 m/s. Therefore to adhere to the requirements of §29.631, simulations of a 1 kg bird striking the windshield at 80 m/s had to be performed. In Appendix C the details of the test set-up and results have been included. The results of the simulations showed that for a 9.3 mm thick acrylic windshield with clamped edges representing the surrounding structure, the A-109 FE model would comply with the certification requirements of §29.631. In case the alternative boundary conditions are adopted (Figure 5.5b), the windshield should be at least 6.6 mm thick to comply with the requirements. Since the results were based on simulations only, it is recommended to conduct actual windshield bird strike tests and subsequently validate the FE model based on the results of this test.

The simulations verified compliance with the certification requirements for Part 29 class helicopters, whilst actually the A-109 is certified to the Part 27 requirements. Therefore, the additional requirement for Part 29 aircraft, stating that continued safe flight must be ensured after an impact with a 1 kg bird, does not apply for the A-109. The outcome of this bird strike analysis is therefore conservative for the A-109 specific, which should be taken into account when analysing the UAS strike results. To endorse this statement, four bird strikes on the A-109 have been reported (AAIB, 2012) which all resulted in a shattered windshield with bird penetration into the cockpit.

5.7. Conclusion

The aim of this chapter was to create an FE model of the windshield of a rotorcraft. With the description of how this model was made, an answer can be given to the second part of the third research question:

How can an accurate and validated model of the helicopter impact location(s)
be made in explicit FEM software?

In summary, the model was made as follows. An accurate CAD model of the A-109 helicopter was imported into the PrePost processor. Three different mesh sizes have been made to ensure a mesh refinement analysis can be completed later on in this study. Because of the shell-shaped geometry of the windshield, 2D fully integrated shell elements were adopted for the model. The acrylic material of the windshield was represented by an elastic perfectly plastic material model. Two different configurations of boundary conditions were adopted and compared to represent the surrounding framework of the windshield. In one configuration, all edges were clamped similar to the boundary conditions in the reviewed literature. In the other configuration, the edges adjacent the other cockpit and overhead windshield were only restricted to translate in the in-plane direction of these adjacent windshields. Since validation of the model was not feasible, the minimum thickness was determined at which the windshield would comply with the Part 29 certification requirements. This bird strike analysis was presented in Appendix C and showed that the windshield must be at least 9.3 mm thick in case all edges of the windshield are clamped in the simulations. For the alternative boundary conditions, this minimum thickness of the windshield would be 6.6 mm. To improve the model, actual bird strike tests have to be performed, such that validation of the FE model can be accomplished. Although the model is currently based on simulations only, the damage caused by a UAS strike can be compared with the bird strike results. This comparison can indicate the expected difference in damage between these two events.

Helicopter windshield UAS impact

In respectively Chapter 4 and Chapter 5, the FE models of the UAS, the DJI Phantom III, and the helicopter impact location, the A-109 helicopter windshield, were created. Hereafter, the collision between these two parts can be simulated and the results of these simulations will be incorporated in this chapter. The aim of this chapter is to determine the damage that the helicopter windshield will sustain after an impact with a UAS in accordance with the fourth research question.

In the first paragraph, the test set-up for the various UAS collisions is detailed. The subsequent results of these various collisions is presented in the second paragraph. This paragraph starts with a detailed analysis of the sustained damage of the windshield under certain conditions. Subsequently, these conditions have been changed in order to assess how these factors would affect the outcome. Simulations have therefore been performed for various boundary conditions of the windshield, orientations of the UAS with respect to the windshield and sizes of the UAS model. Thereafter, a comparison of the damage propagation mechanism between the UAS impact and a bird strike is presented. In the third and last paragraph, the chapter is summarized and an answer is given to the fourth research question regarding the sustained damage on the helicopter impact location caused by the collision.

6.1. Test set-up

The test set-up in terms of striking location and velocity for the UAS impact simulations was similar to the bird strike analysis as detailed in Paragraph C.1. This would enable a direct comparison of the results of the UAS and bird strike simulations. The impact velocity was therefore set to the maximum cruising velocity of the A-109 of 80 m/s in line with the certification requirements, refer to Paragraph 5.6. The battery of the UAS impacted the same location as the bird, since the expected damage would be the largest at this location of the windshield. This assumption was based on the fact that the distance to the edge of the windshield was the largest whilst the windshield's orientation was most perpendicular to the direction of motion of the bird. An overview of the test set-up is presented in Figure 6.1.

In the simulation, only contact was defined between the various UAS components and the target windshield, whilst contact between the various UAS components was not incorporated to save computational time. The inclined orientation of the windshield with respect to the direction of motion of the UAS namely would result in the components deflecting away from the windshield after initial contact. Therefore the various components would only pass through each other after the energy transfer with the windshield has already been completed. The reader might observe the components unnaturally passing through each other after contact with the windshield.

In all cases, the calculation time required for the 1.75 mm windshield mesh exceeded 96 hours. Therefore it was not feasible to use this mesh in this model for the numerous simulations that were required to be completed. The next dense mesh of 3.50 mm, refer to Figure 5.3b, was incorporated in the simulations. For the different boundary conditions tested in the bird strike analysis, the clamped boundary conditions required the thickest windshield to comply with the regulations and the expected damage of the UAS impact would for this reason be the least for this configuration. Using a best case approach for the helicopter crew, the clamped boundary conditions were imposed
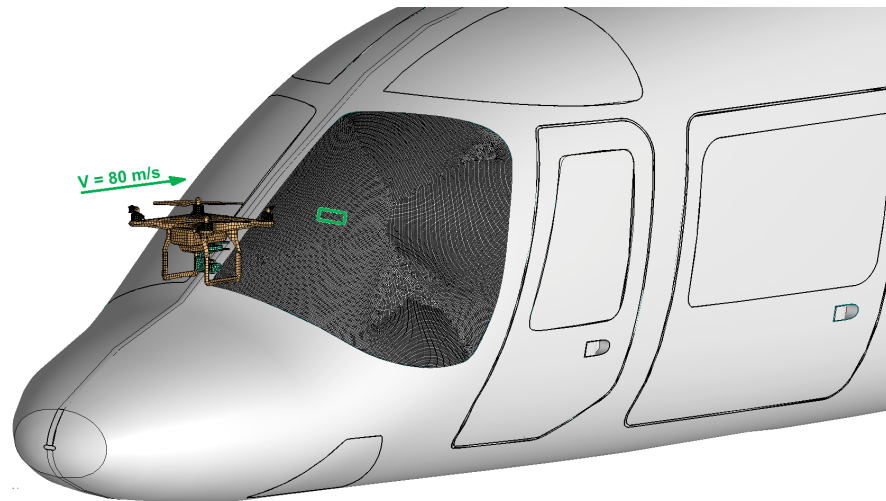
■ Impact location of the UAS battery.
Note: The windshield surrounding structure is only displayed for visualization purposes and was not incorporated in the simulation.

Figure 6.1: *Helicopter windshield UAS impact simulation overview.*

onto the edges of the windshield during all the simulations. An exception is the comparison of windshield damage for the various configurations of boundary conditions in Paragraph 6.2.2.

6.2. Damage assessment

6.2.1. UAS impact

To assess how much damage the windshield would sustain after a UAS impact, the DJI Phantom III was impacted onto a windshield that would comply with the certification requirements for Part 29 aircraft. As analysed in Paragraph 5.6, this would be the case for the A-109 windshield model of a 9.3 mm thickness for the clamped boundary conditions. The results of the simulation are presented in Figure 6.2 and 6.3.

After the battery and camera initiated the damage at the impact location, the damage propagated over the entire windshield. At the end of the simulation, only the edges of the windshield remained intact and attached to the surrounding frame, which was simplified by the imposed the boundary conditions. The windshield broke into dangerous fragments which entered the cockpit as shown in the view from inside the cockpit in the figures. Additionally the battery and main body of the UAS partly penetrated the windshield and entered the cockpit, refer to Figure 6.4a, whilst the other parts deflected away from the windshield.

Based on the simulations, it can be concluded that a Part 29 compliant windshield would sustain severe damage after an impact with the DJI Phantom III. The CS §27-29.775 (EASA, 2018a, FAA, 2019a) states that the windshield must not break into dangerous fragments, refer to Paragraph 5.6. This requirement would not be met for the UAS impact. Additionally the §29.631 CS requires that continued safe flight and landing must be guaranteed after impact with a 1 kg bird. For the impact by the DJI Phantom III, safe flight and landing would not be guaranteed since fragments of the windshield as well as parts of the UAS would enter the cockpit and could strike the crew. These requirements would be met in case the thickness of the windshield is increased to 16.0 mm, which would be a 72% increase in thickness and corresponding weight of the windshield.

Isometric view.

Frontal view. UAS main body is not shown.

View from inside the cockpit. Windshield surrounding structure is shown for visualization purposes and was not incorporated in the simulation.

(a) *Time 0 ms*   **(b)** *Time 2.5 ms*   **(c)** *Time 5.0 ms*

Figure 6.2: *Damage propagation of a 9.3 mm thick windshield with clamped edges impacted by the UAS (t = 0 ms, 2.5 ms, 5.0 ms).*

Isometric view.

Frontal view. UAS main body is not shown.

View from inside the cockpit. Windshield surrounding structure is shown for visualization purposes and was not incorporated in the simulation.

(a) *Time 7.5 ms*   **(b)** *Time 10 ms*   **(c)** *Time 15 ms*

Figure 6.3: *Damage propagation of a 9.3 mm thick windshield with clamped edges impacted by the UAS (t = 7.5 ms, 10 ms, 15 ms).*

6.2.2. Windshield boundary conditions

In the FE model of the A-109 windshield, two configurations of boundary conditions were imposed on the edges of the windshield as detailed in Paragraph 5.5. Subsequently the minimum thickness at which the windshield would comply with the bird strike certification requirements was determined for each of this configuration in Paragraph C.2. A minimum thickness of 9.3 mm was required for the windshield with the clamped edges, whilst a 6.6 mm thick windshield would comply in case the alternative boundary conditions are imposed. All simulations up to this point have been performed with the clamped edges. A comparison between the resulting damage after the UAS impact onto the specific compliant windshield for the two boundary condition configurations is made in this paragraph.

The final damage of the windshield after the impact and the parts of the UAS that penetrated the windshields into the cockpit during the collision are shown in Figure 6.4. The damage of the windshield caused by the collision is of a similar size for both the configurations of boundary conditions. However, the number of parts penetrating the windshield into the cockpit differs significantly between the two tested configurations. For the clamped boundary conditions, the back part of the battery and a small part of the main body penetrated the windshield. For the thinner windshield with the alternative boundary conditions, only the front part of the main body and of the battery would not penetrate the windshield. It can be concluded that in case the alternative boundary conditions would be an appropriate representation of the surrounding structure of the windshield, the cockpit crew would be exposed to a significantly higher risk of sustaining injuries due to parts of the UAS striking the body. This conclusion is based on a comparison with the results of the simulations with the clamped boundary conditions in this chapter.

6.2.3. Various UAS orientations

All simulations up to this point were performed with the UAS oriented in its forward flying direction, i.e. with the camera pointing towards the target. As analysed in Drumond, Greco, and Cimini (2019), the critical components of the UAS are the motors, battery, and camera. Of these critical components, the two left hand side motors as well as the two right hand side motors of the UAS line up during an impact with the UAS oriented in its forward flying direction (0° orientation). After rotating the device 45° around its yaw axis, the battery lines up with the right forward and left aft motors, thereby concentrating more mass of the UAS on a smaller area of the target during the impact. To assess how the orientation of the UAS would affect the resulting damage, simulations have been completed for the 0° and 45° orientations, refer to Figure 6.5. The thickness of the windshield was set to 14.0 mm, since the resulting damage in the form of a distinct hole could easily be compared for both the tested orientations impacting a windshield with this thickness.

The orientation of the 0° (frontal) and 45° orientation as well as the final resulting damage of the windshield after the collision is shown in Figure 6.5. A square shaped hole of 11.1×10.3 cm was formed after an impact with the 0° oriented DJI Phantom. This damage was mainly caused by the impact of the battery and camera at that location. The hole caused by an impact with the 45° oriented device was larger and more of a rectangular shape stretched in the vertical direction (9.6×17.1 cm). Initially, the battery and camera formed a hole in this windshield. Thereafter the aft motor, which is positioned above the battery in the UAS, enlarged the hole after impacting the already weakened structure of the windshield. It can therefore be concluded that an impact with the UAS rotated 45° over its yaw axis would cause more damage compared to a frontal (0°) impact.

6.2.4. Various scaled UAS models

As presented in Paragraph 6.2.1, the DJI Phantom III would partly penetrate a windshield that complies with the bird strike certification requirements and would break the windshield into dangerous fragments. The question arises to what extent these windshields would protect the crew after a UAS strike. To examine this matter, the original UAS model was scaled down to the extent that the UAS

Final damage of the windshield.

Parts of the UAS penetrating the windshield.

(a) *Clamped boundary conditions.*
Windshield thickness is 9.3 mm.

(b) *Alternative boundary conditions.*
Windshield thickness is 6.6 mm.
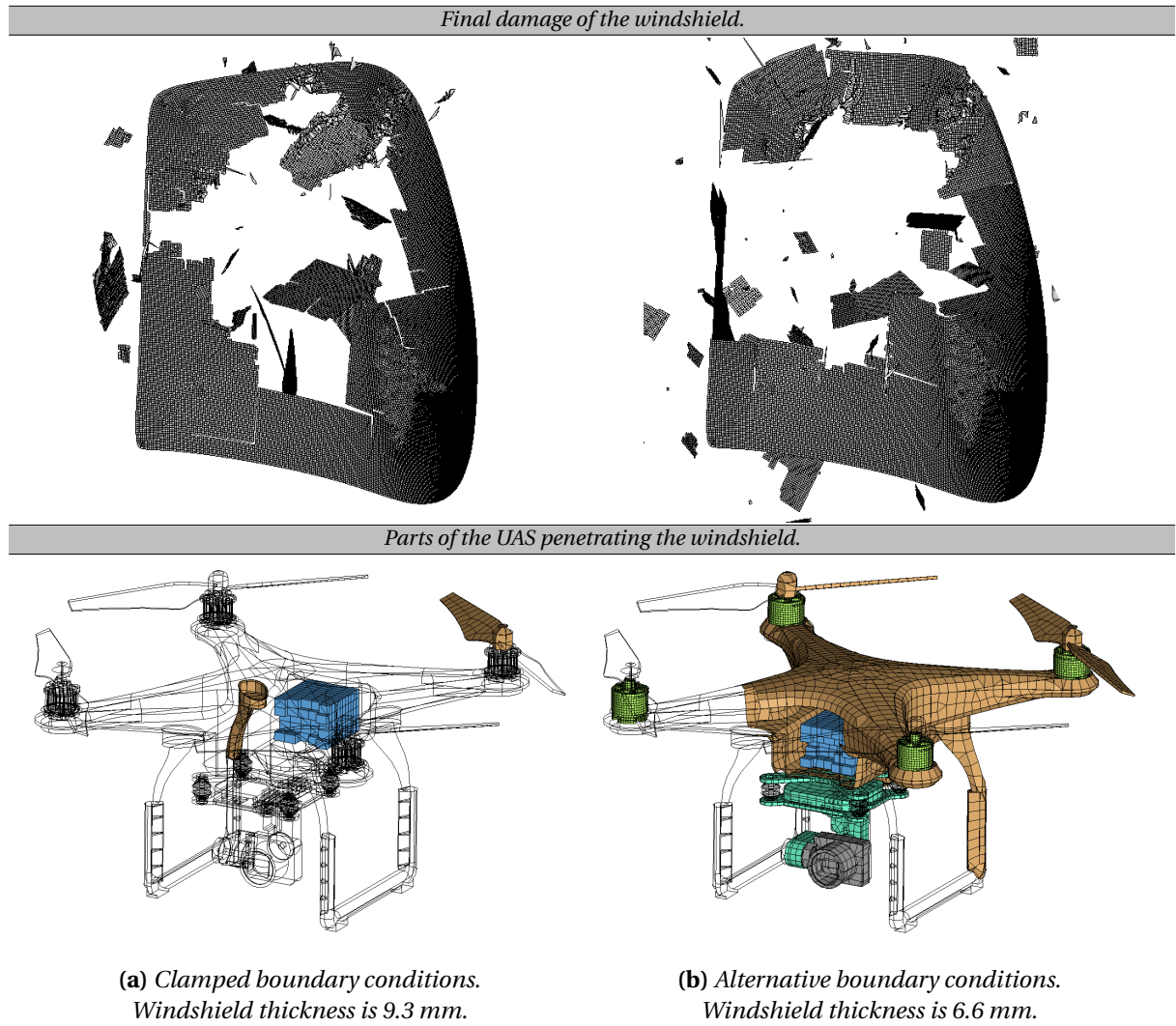
Figure 6.4: *Comparison of the damage of and the UAS parts penetrating a Part 29 compliant windshield for various windshield boundary conditions.*

Frontal view. UAS main body is shown transparent.
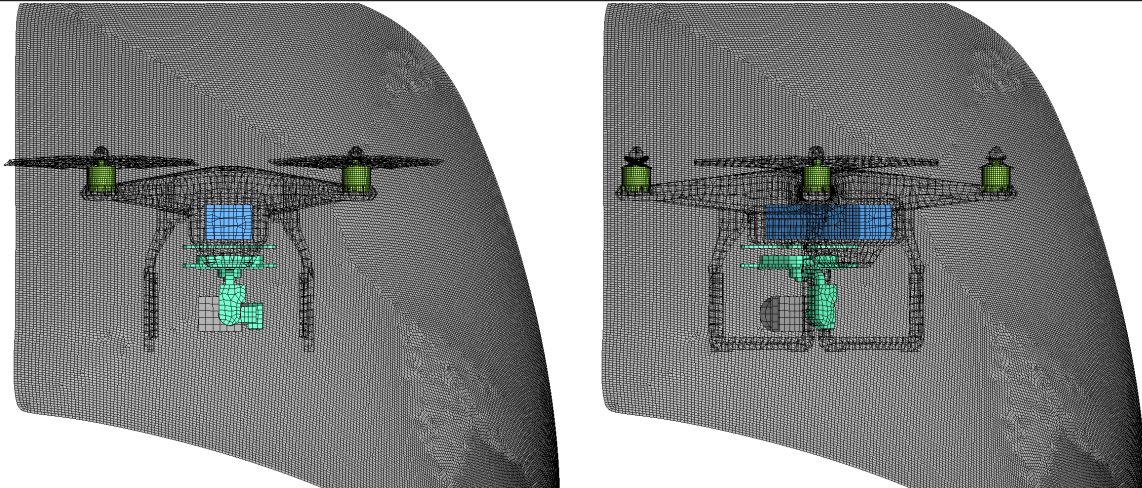
Isometric view of final damage.
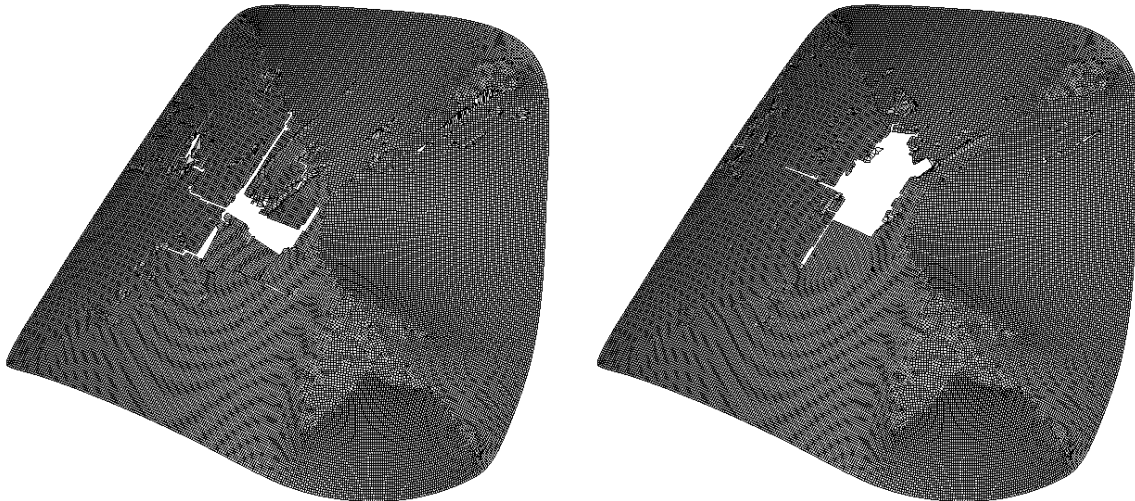
Measurements of final damage. Loose fragments are not shown.
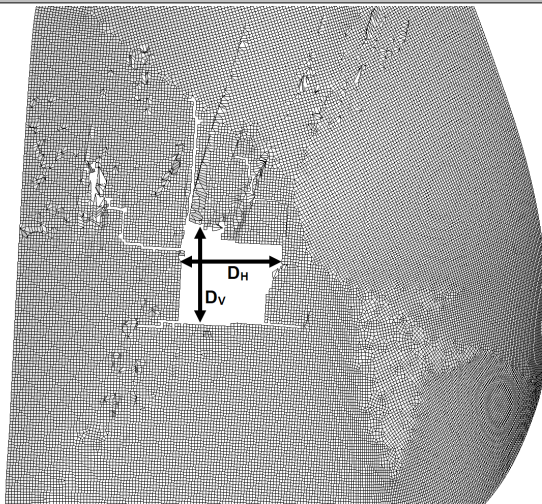
D_H= 11.1 cm, D_V = 10.3 cm

(a) *0° orientation.*
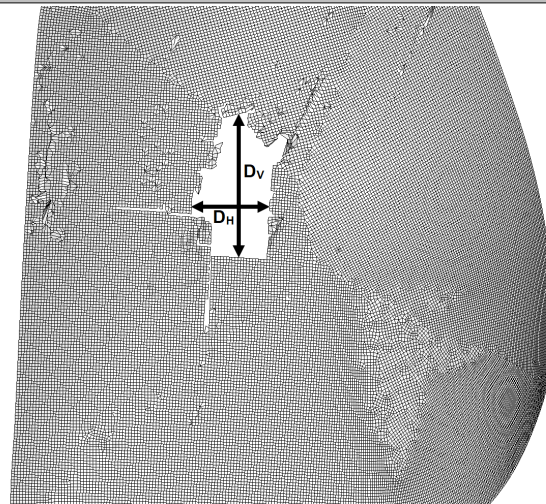
D_H = 9.6 cm, D_V = 17.1 cm

(b) *45° orientation.*

Figure 6.5: *Comparison of the damage of a 14.0 mm thick windshield impacted by the UAS for various UAS orientations.*

would no longer penetrate the windshield or break it into dangerous fragments. For this purpose, the Part 29 compliant windshield model for the clamped boundary conditions with a thickness of 9.3 mm was used. Scaling of the UAS was based on the weight of the device, so the weight was halved compared to the actual DJI Phantom III for a scale factor of 1/2. To realize this scaling, the length, height, and width of the geometry of the device were reduced by a factor of $\sqrt[3]{1/2} \approx 0.8$ for a scale factor of 1/2 and $\sqrt[3]{1/4} \approx 0.63$ for a scale factor of 1/4. Additionally, the thickness of the 2D shell elements of the main body and propellers was also reduced by the same factor.

The UAS original and scaled models with the corresponding final damage of the windshield after the impact are shown in Figure 6.6. For a DJI Phantom III scaled to half its weight, components of the device would no longer penetrate the windshield. However, the windshield would still break into dangerous fragments which could injure the crew in the cockpit. For a quarter weight of the original UAS, the device would deflect away from the windshield. At the top of the windshield, a small crack was formed and the motors left some scratches on the windshield. However, the windshield remained intact thereby protecting the crew from the impact.

An interesting correlation can be observed with the UAS regulations imposed by the aviation authorities as described in Paragraph 3.1.1. The least stringent regulations are imposed when operating a UAS with a MTOW less than 250 g. In line with the results of the simulations with the 300 g UAS (1/4 scaled DJI Phantom III), these devices would only pose minimal risk to the crew for a windshield impact.

6.2.5. Comparison with bird strike

As stated previously, the windshields of a Part 29 rotorcraft are designed to comply with a bird strike requirement. The results in the previous paragraph (6.2.1) showed that such a certified windshield would sustain severe damage after an impact with the DJI Phantom III. After completing various simulations, it became apparent that the damage caused by a bird strike initiates and propagates in a different manner when compared to the damage caused by the UAS impact. To visualize this difference, the UAS impact on a 9.3 mm thick windshield will be compared with the bird strike on a 7.0 mm thick windshield, since the resulting final damage caused by these impacts is of a similar size. The moment at which the damage on the windshield is initiated and the final damage for the UAS impact and bird strike are shown in Figure 6.7.

After the UAS battery and camera made contact with the windshield, the damage immediately initiates at that location. The components of the UAS partly bounce off and partly penetrate the windshield as shown in Figure 6.2 and 6.3. The load is therefore concentrated at the impact location of these components. Thereafter, the damage propagates and creates a large hole in the middle of the windshield, whilst the edges of the windshield remain intact. The results of the simulations showed that the impact of the critical components of the UAS on the windshield can be considered as a hard body impact.

The bird initially contacts the windshield at the same location as the battery of the UAS. However, the bird does not bounce off the windshield, but deforms and flows along the inclination of the target. This results in the load extending over a larger area. The damage is subsequently initiated at the top of the windshield and thereafter propagates further over the windshield. At the end of the simulation, the left hand side and bottom edge of the windshield remained intact. In this simulation, the bird partly penetrated the cockpit through the opening that was created at the top edge of the windshield after the damage initiation. The behaviour during the bird strike can be considered as a soft body impact.

The comparison of the impact events showed that the design of the windshield takes into account a damage propagation mechanism, which is different when compared to the mechanism caused by a UAS impact. To protect a crew after an impact by a UAS, the certification requirements of the windshield should be amended to incorporate an appropriate hard body impact criteria.

Original size.

29.1 cm

Mass = 1211 g

Scale factor 1/2.

23.3 cm

Mass = 606 g

Scale factor 1/4.

18.3 cm

Mass = 303 g

(a) *UAS model dimensions.*   **(b)** *Windshield final damage.*
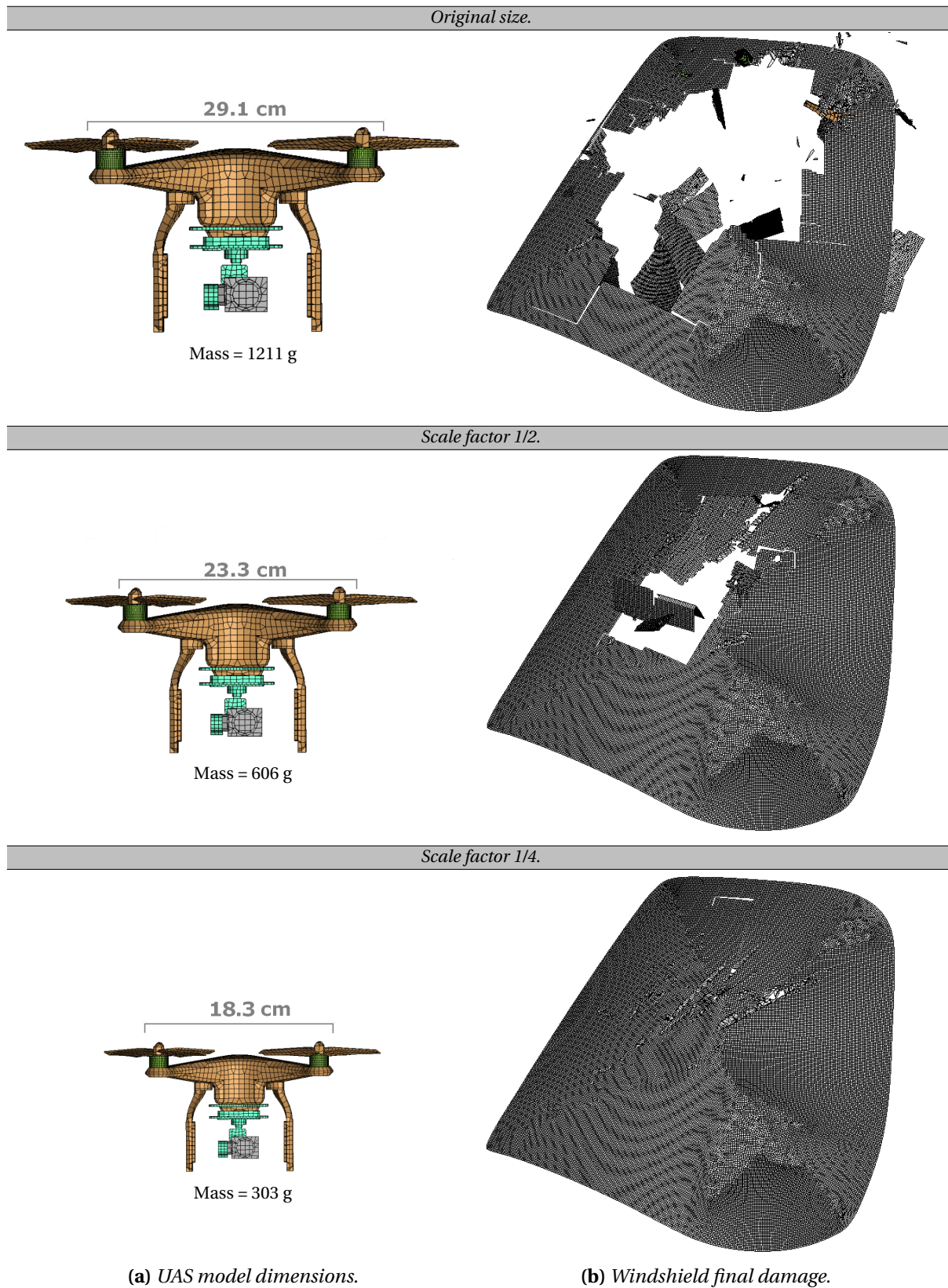
Figure 6.6: *Comparison of the damage of a 9.3 mm thick windshield impacted by the UAS for various scaled UAS models.*

Damage initiation.

Final damage.

(a) *UAS impact on a 9.3 mm thick windshield.*
Main body is not shown.

(b) *Bird strike on a 7.0 mm thick windshield.*
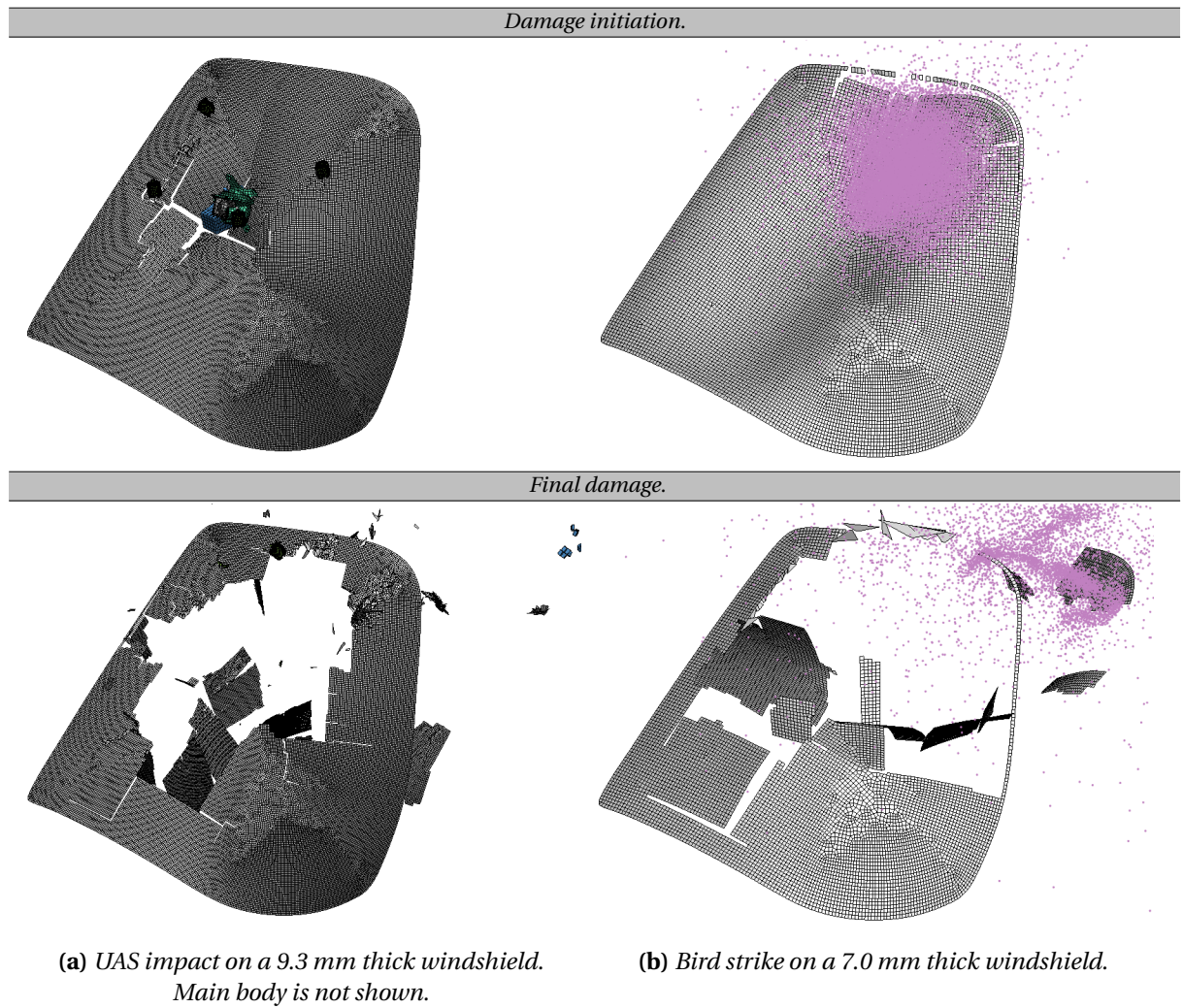
Figure 6.7: *Comparison of the damage propagation mechanism of a windshield UAS impact and bird strike.*

6.3. Conclusion

In this chapter, various collisions between the UAS and helicopter windshield have been simulated. The aim of this chapter was to determine the damage that the helicopter windshield would sustain after an impact with a UAS. The results of the simulations provide an answer to the fourth research question:

What would be the damage on the helicopter impact location after the collision with the UAS has occurred?

The striking velocity of the UAS was set in the simulation to the maximum cruising velocity of the A-109 of 80 m/s. In the baseline set-up of the simulations, the UAS was oriented in its forward flying direction with respect to the windshield and the clamped boundary conditions were imposed to the edges of the windshield. Under these conditions, the damage to a Part 29 compliant windshield would be severe and the battery and main body of the UAS would partly penetrate the windshield thereby potentially striking the crew. Additionally, the windshield would break into dangerous fragments also posing a risk to the crew. A substantial increase of approximately 72% in the windshield thickness and therefore also in the corresponding weight of the windshield would be required to guarantee safe flight and landing after the impact. Since less stringent certification requirements apply to the windshield of Part 27 compliant windshields, these aircraft would sustain even more damage or more parts of the UAS would penetrate into the cockpit. In case the alternative boundary conditions would be more appropriate to represent the surrounding structure, the damage to the windshield would remain of a similar size, but more parts of the UAS would penetrate the windshield. Therefore the crew would be exposed to a higher risk of sustaining severe injuries. A comparison was made between the resulting damage of a frontal collision and in case the UAS was rotated 45° around its yaw axis. The latter would result in slightly more damage to the windshield. Subsequently an analysis was completed to determine how well the crew would be protected against an impact of a UAS of a smaller size. The results of the simulations showed that the currently compliant Part 29 windshields would protect the crew from an impact of a 1/4 scaled DJI Phantom III, which would weigh approximately 300 g. Additionally, a comparison was made between the UAS impact and the bird strike. This comparison indicated that the windshield is designed to withstand a soft body impact of the 1 kg bird strike, whilst the UAS impact can be considered a hard body impact.

<div align="right">7</div>

Discussion of the results

In the previous chapters of this report, the results of this research as well as the process of obtaining these results are presented. During the process and after analysing the results in detail, certain observations have been made worth discussing further in detail. A discussion of each of these observations is included in this chapter. The aim of this chapter is to provide a more detailed insight in the results and to put the results in perspective.

In the first paragraph, the effect of the various tested boundary conditions of the windshield on the results and conclusions in this report will be discussed. Subsequently, the representativeness of the various scaled DJI Phantom III UAS models in Paragraph 6.2.4 is assessed in the second paragraph. A discrepancy between crack propagation of the windshield in the simulations and in actual cracked acrylic windshield is addressed and further investigated in the third paragraph. The conclusions of this chapter are summarized in the fourth and last paragraph.

7.1. Boundary conditions windshield

Two configurations of boundary conditions were incorporated in the different windshield models. In the first configuration, all the translational and rotational degrees of freedom of the edges of the windshield were constrained. In the second configuration less stringent boundary conditions were imposed in the simulations. The edge adjacent the right hand cockpit windshield and adjacent the overhead windshield were only constrained of translating into a single direction, refer to Figure 5.5. The other edges remained clamped by constraining all the degrees of freedom.

To compare the effect of the various boundary conditions, the bird strike simulation as detailed in Paragraph C.1 is completed on a 9.3 mm thick windshield for the two configurations of boundary conditions as defined previously. In addition to support the comparison, the test was performed for simply supported boundary conditions i.e. restricting the translations but not constraining the rotations of the windshield edges. The von Mises stresses in the windshield at 4.5 ms after initial contact with the bird for the three configurations of boundary conditions is presented in Figure 7.1. The figure shows that the von Mises stresses in the windshield decrease during the bird strike event in case less stringent constraints are imposed on the edges of the windshield. This decrease in von Mises stresses in the end results in a reduction in the required thickness of the windshield for compliance with the 1 kg bird resistance certification requirement. Since less stringent constraints represent a more flexible surrounding structure, it can be concluded that a thinner windshield is required for compliance with the certification requirements in case the surrounding structure is more flexible. Respectively for the clamped boundary conditions, this thickness was 9.3 mm, for the simply supported edges 8.5 mm and for the alternative boundary conditions 6.6 mm.

However for the hard body impact of the UAS, the various boundary conditions have limited effect on the results. Most of the damage has already been sustained prior to the shockwaves propagating through the windshield towards the edges. As shown in Figure 6.4, more parts of the UAS would penetrate the thinner windshield with less stringent boundary conditions. For the simply supported boundary conditions, the number of UAS parts penetrating the required 8.5 mm thick windshield was in between the clamped and alternative boundary condition configurations. In addition, the exact same windshield thickness of 16.0 mm is required for the alternative and the

<div align="center">54</div>

(a) *Clamped.*   (b) *Simply supported.*   (c) *Alternative.*
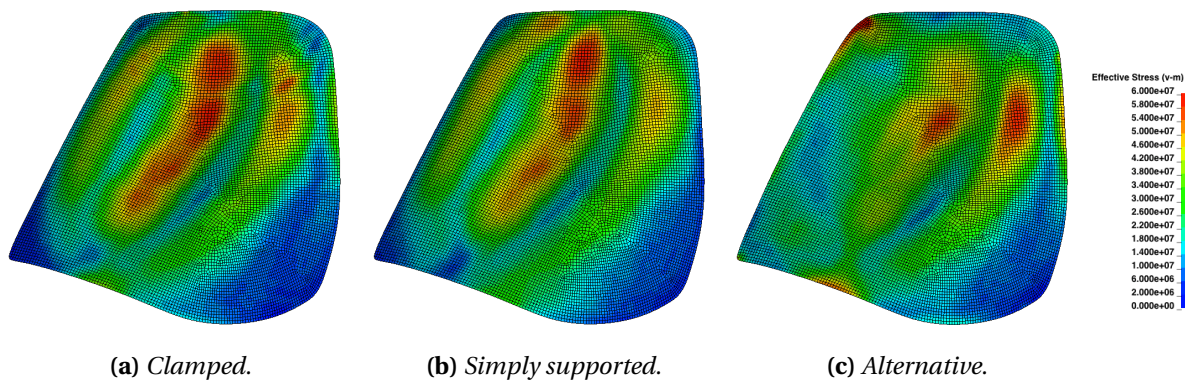
Figure 7.1: *Comparison of the von Mises stresses of a 9.3 mm thick windshield impacted by a 1 kg bird 4.5 ms after initial contact for various boundary conditions.*

clamped boundary conditions to prevent UAS parts penetrating the windshield and the windshield breaking into dangerous fragments. In conclusion, a thinner windshield in combination with less restrictive boundary conditions makes the Part 29 compliant windshield less impact resistance for a collision with the UAS.

Which configuration of boundary conditions would be representative for the A-109 windshield remains unknown at the moment. However, it can be concluded that in case the surrounding structure is more flexible, a thinner windshield is required for compliance with the Part 29 certification requirements. These thinner windshields with less stringent boundary conditions are less impact resistant for the UAS impact. Additionally, the sustained damage and the number of UAS parts penetrating the windshield has a strong correlation with the imposed boundary conditions. Therefore an accurate representation of the surrounding structure is of a high importance in the simulations to obtain accurate and realistic results.

7.2. Scaling of the UAS

In Paragraph 6.2.4, the FE model of the DJI Phantom III was scaled down based on weight up to the point that no parts of the UAS penetrated the windshield and the windshield would no longer break into dangerous fragments. For the 1/4 scaled model with a weight of 303 g, these terms were met. Whether this scaled model would be representative for a UAS of similar weight can be assessed by comparing the model with an actual drone. The DJI Spark, shown in Figure 7.2, is a quadcopter type UAS with a comparable take-off weight of 300 g with respect to the 1/4 scaled Phantom III model. A comparison of the weight and dimensions of the entire UAS, the battery, and the motor of the DJI Spark and the scaled Phantom III model is presented in Table 7.1.

Of the critical components, a comparison of the material properties, dimensions, and weight of the camera could not be completed, since no data regarding this component of the DJI Spark was available. The power source of the DJI Spark is a Lithium-ion battery and the motors are brushless with a steel stator and aluminium rotor similar to these components installed into the DJI Phantom III. The sizes of these components are of a comparable order with a maximum relative difference in the length of the battery of 35%, however, the volume of the battery pack only differs 2%.

The geometry of the main body of the two devices is dissimilar. The DJI Phantom III scaled model is larger in height (relatively 28%), predominantly because no landing gear is attached to the DJI Spark. In case the landing gear is omitted in the scaled Phantom III model, the height of the main body is 49 mm which is a relative difference of 12% compared to the DJI Spark. In addition, the camera is located in front of the battery, whilst in the (scaled) Phantom III model the camera is below the battery. The mass of these components would be concentrated over a smaller area for the Spark, therefore potentially causing slightly more damage.

Figure 7.2: *DJI Spark Alpine White (DJI Technology Co., 2020b).*

Table 7.1: *Comparison of the 1/4 scaled DJI Phantom III model and the DJI Spark.*

Parameter	Scaled DJI Phantom III model	DJI Spark[1]
UAS		
Weight (g)	303	300
Dimensions (mm)	183×183×119	143×142×55
Battery		
Weight (g)	86	95
Dimensions (mm)	81×29×21	60×34×26
Motor		
Weight (g)	13	10
Dimensions (mm)	15×17.6	17×14.5

[1] DJI Technology Co. (2020b).

In conclusion, the materials, dimensions, and weight of the various components of the scaled DJI Phantom III model and of the Spark are of a comparable order. Note that no comparison is made for the camera. There are some differences in the geometry of the main body and the location of some components with respect to each other. However in general, the scaled model would provide a reasonable approximation of the sustained damage after an impact on the windshield for an actual drone of comparable weight.

7.3. Crack propagation

In the various simulations performed in this study, the cracks in the windshield propagated predominantly along straight lines. The consequent loose fragments of the windshield were therefore primarily of a quadrilateral shape. When analysing the damage pattern of actual acrylic windshields impacted by a bird, the damage propagates more along curved lines. An example of both damage patterns is shown in Figure 7.3 which highlights the discrepancy between actual damage and the

(a) *A-109 acrylic windshield FE model.*   **(b)** *Bell 429 acrylic windshield (AAIB, 2019).*
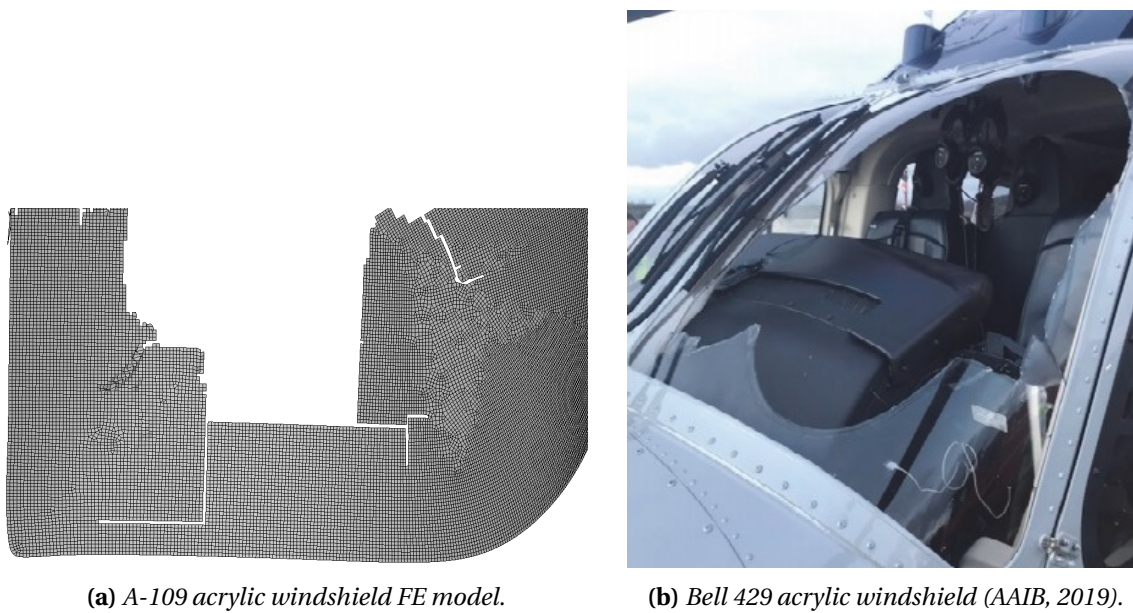
Figure 7.3: *Comparison of the damage pattern caused by a bird strike of
an actual damaged acrylic windshield and the FE model simulation.*

simulation results. In the simulations, the damage initiates when a certain element reaches its element erosion criterion and is thereby deleted from the equation. Subsequently the damage propagates due to adjacent elements also reaching the erosion criterion. Within the quadrilateral mesh of the windshield this results in straight line cracks (Figure 7.3a bottom cracks), whilst in the triangular mesh area in this windshield the cracks were more curved (Figure 7.3a top right crack). The crack propagation therefore appeared mesh dependent and further analysis to assess the effect on the results in this thesis is incorporated in this paragraph.

By default, the LS Dyna PrePost processor 2D automatic mesher is set to mixed mode, which combines quadrilateral and triangular elements depending on the shape of the part to create the shell element mesh. This default mode was used for the windshield mesh in this research and resulted in a uniformly distributed quadrilateral mesh with only triangular elements incorporated along the bending lines of the windshield. A detailed representation of this mesh is shown in Figure 5.3. The only alternative option in the PrePost 2D automatic mesher is the triangle mesh type, which exclusively uses triangular elements to create the mesh regardless of the shape of the part.

The results of the bird strike simulation of the 8.0 mm thick clamped windshield (mixed mode mesh), as detailed in Appendix C.1, were compared with the results of a triangular mesh under the same test conditions. Similar to the element size of the mixed mode mesh in that analysis, the element size in the automatic mesher was set to 7.0 mm for the triangular mesh. A zoom view of the two meshes created by the two mesh type selections and the resulting final damage of the bird strike simulations are presented in Figure 7.4.

The cracks in the triangular mesh propagated more along curved lines when compared to the damage in the mixed mesh. Therefore the damage pattern more closely matched actual bird strike damage on an acrylic windshield. However, the final resulting damage for both meshes shows strong similarities and does not vary notably between the two meshes. Therefore it can be assumed that the conclusions based on the results of the simulations with the mixed mode mesh in this study would not significantly change in case the triangular mesh was adopted.

Mesh overview.

Final damage.

(a) *Mixed mesh.*   **(b)** *Triangular mesh.*
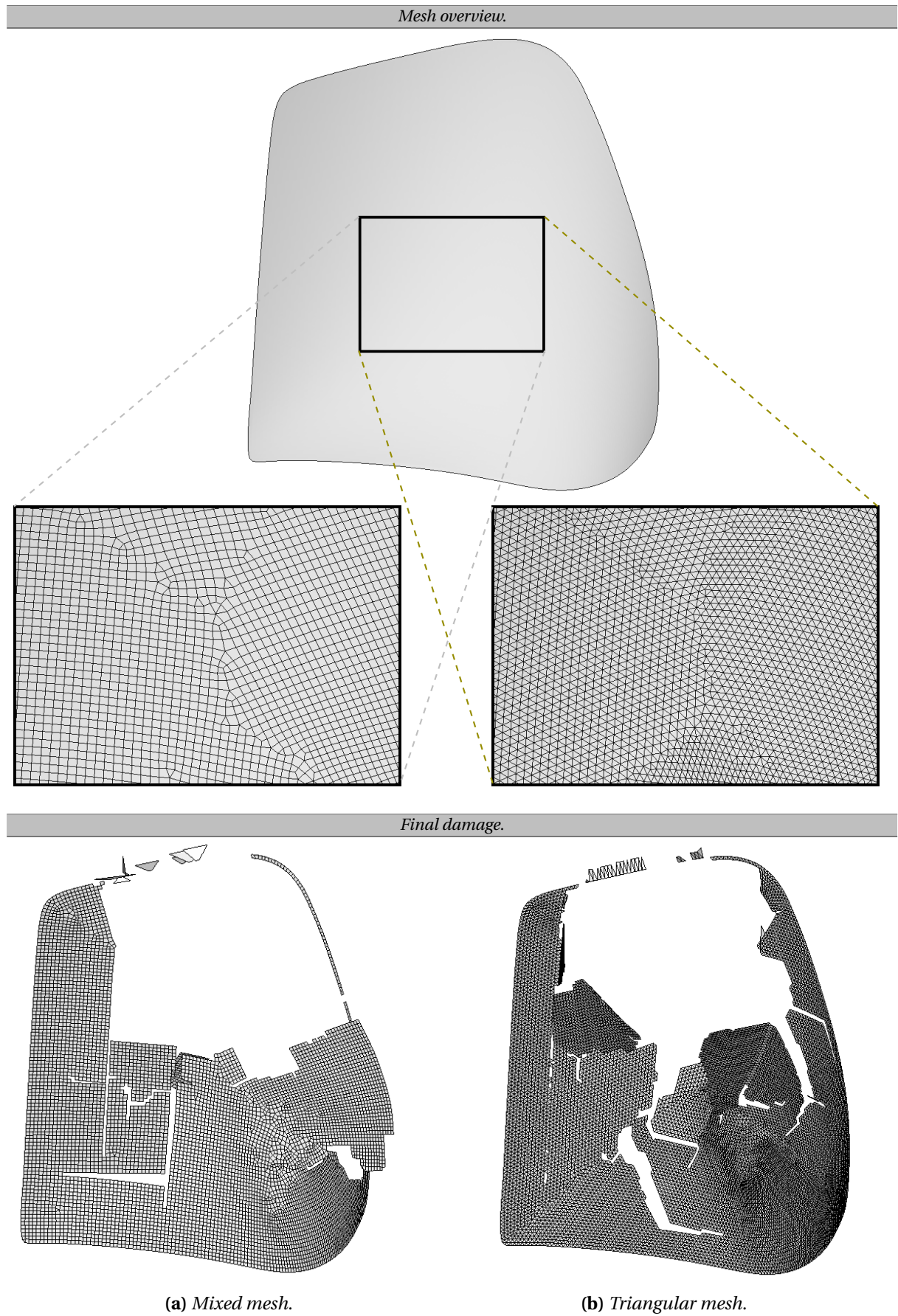
Figure 7.4: *Comparison of the damage pattern of a 8.0 mm thick windshield impacted by
a 1 kg bird for various windshield mesh types.*

7.4. Conclusion

In this chapter, a discussion is presented regarding certain observations that have been made during the process of obtaining the results of this research as well as after analysis of these results. The effect of the various boundary conditions on the conclusions of this report has been assessed. For a surrounding structure of higher stiffness, a thicker windshield is required to comply with the bird strike certification requirements. However, the boundary conditions do not have a significant effect on the resistance of a UAS impact. Therefore a thinner windshield would result in more parts of the UAS penetrating the windshield. It can be concluded that the boundary conditions have a significant effect on the results of the impact and therefore should be accurately represented. Note that it is currently not known what boundary conditions would be realistic specifically for the A-109. To assess the representativeness of the 1/4 scaled DJI Phantom III model, a comparison with a UAS of similar take-off weight, the DJI Spark, is made. The materials, dimensions, and weight of the various components of the scaled DJI Phantom model and the actual Spark are of a comparable order. Although some differences for example in the main body geometry and the location of the camera can be observed, the results of the scaled model would provide a reasonable approximation of the sustained damage after an impact with an actual drone of a comparable weight. In the last paragraph, the discrepancy of the damage pattern in the simulations and actual acrylic windshields is addressed. A new mesh exclusively made out of triangular elements was created of which the crack propagation showed a stronger correlation with actual damaged acrylic windshields. However, the sustained damage remained of a similar size and therefore it was concluded that the discrepancy in damage pattern would not have a significant effect on the conclusions in this research.

8
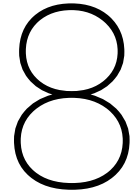
Conclusions and recommendations

In this final chapter of the report, the conclusions of the research will be presented thereby meeting the thesis objective. Thereafter, recommendations to update the certification requirements, to improve the results of the simulations, and to continue the work of this research are proposed.

8.1. Conclusions

In the main body of this report, the four research questions as defined in the aim and scope of this study (Paragraph 1.2) have been answered. The answer to these research questions produced the data required to achieve the thesis objective, which was defined as follows:

The objective of this thesis was to predict the helicopter's damage caused by a collision with an Unmanned Aerial System using explicit Finite Element Analysis.

In this study, it was demonstrated by means of simulations that an A-109 windshield compliant with the Part 29 bird strike certification requirement (§29.631) would sustain severe damage after a collision with the DJI Phantom III. Not only would the windshield break into dangerous fragments that could enter the cockpit, parts of the UAS would also penetrate the windshield thereby potentially severely injuring the crew. It can therefore be concluded that the certification requirements do not guarantee a similar level of safety in case the windshield is impacted by this UAS. These results have been obtained in the most favourable conditions for the crew. This would be the case if the UAS is oriented in its forward flying direction, clamped boundary conditions are a realistic representation of the surrounding windshield structure, and the Part 29 certification requirements apply to the rotorcraft.

If the device is rotated 45° around its yaw axis, the damage would slightly increase when compared to a frontal impact. This is caused by the fact that more critical components of the UAS line up and impact a smaller area of the windshield. In case the surrounding structure of the windshield would be rather flexible, the clamped boundary conditions are not a realistic representation. Fewer constraints have to be imposed onto the edges of the windshield which leads to a reduction in the required thickness of the windshield for compliance with the Part 29 certification standards. This reduction in thickness results in more parts of the UAS penetrating the windshield therefore increasing the risk of injuries to the crew even further. For Part 27 category rotorcraft such as the A-109, no bird strike certification requirement is applicable. A thinner windshield would therefore suffice to pass certification of the rotorcraft causing even more sustained damage and UAS parts penetrating the cockpit after the collision.

After scaling the DJI Phantom to 1/4 of its original weight, parts of the UAS would no longer penetrate the windshield and the windshield would not break into dangerous fragments. Therefore it was shown that a Part 29 compliant windshield would provide a similar level of safety compared to the bird strike requirement for the smaller UAS devices.

8.2. Recommendations

In the conclusion, it was stated that the crew would not be protected against a UAS impacting a windshield that complies with the currently prevailing certification requirements. Therefore in the first subparagraph, a recommendation is provided on how the certification requirements should be amended to guarantee safety of the helicopter crew and passengers. This would be required in case UAS impacts occur on a regular basis in the future. Additionally, throughout the report recommendations have been addressed to improve the FE models in the impact simulations. These recommendations are detailed in the second subparagraph. Opportunities for future work have been proposed by the author in the third and last subparagraph.

8.2.1. Impact related certification requirements

The only prevailing impact related certification requirement at this moment is the §29.631 (EASA, 2018b, FAA, 2019b) which applies to all Part 29 rotorcraft. This specification requires that a safe landing can be guaranteed after the rotorcraft has been impacted by a 1 kg bird. It has been shown in this research by means of simulations that this certification requirement does not guarantee a similar level of safety in case the windshield of a rotorcraft is impacted by a DJI Phantom III. Since the UAS impact is considered a hard body impact whilst the bird strike is a soft body, a different design philosophy would be required to protect the crew as well as the passengers.

Therefore in case UAS impacts occur on a regular basis in the future exceeding an acceptable level of risk, the impact related certification specification should be amended. The amendment should incorporate a hard body impact requirement that covers most of the UAS devices in use at that time. Since at this moment there is no impact related requirement imposed on Part 27 rotorcraft, it should be considered to also incorporate the new requirement in the Part 27 certification standards.

8.2.2. Improvements of the FE models

FE models of various parts of the UAS, the helicopter windshield, and a bird have been developed in this study. The following improvements to these models can be made:

UAS Battery (Paragraph B.2)

Of the critical components of the UAS, only the results of the battery did not show a strong correlation with the validation test results performed by Olivares et al. (2017). The initial deformation was captured accurately, however, the subsequent deformation of the target plate was initially over predicted and thereafter under predicted. To improve the correlation, the casing of the battery can be incorporated in the model or a different numerical mesh, such as an SPH formulation, can be adopted. Additionally, strain softening in the model can be introduced to more accurately capture the initial displacement peak.

Helicopter windshield surrounding structure (Paragraph 5.5)

In the FE model of the helicopter windshield, the surrounding structure was not incorporated due to unavailability of information regarding this framework. Instead, various configurations of boundary conditions were imposed directly at the edges of the windshield and subsequently the results were compared. This comparison indicated that the various boundary conditions result in different thicknesses of the windshield to comply with the certification requirements. A different thickness significantly affected the resulting damage caused by the UAS impact. The FE model of the windshield can therefore be improved by incorporating an accurate representation of the surrounding structure. This improvement will directly result in more accurate results of the damage caused by the UAS impact.

Helicopter windshield validation tests (Paragraph 5.6)

Within this study, the helicopter windshield model has not been validated due to unavailability of validation data. Therefore the results of impacts onto the windshield are based on simulations only. Instead of validating the model, a design process was completed by simulating non-validated bird strikes to assess for which windshield thickness, the model would comply with the applicable certification requirements. To improve the helicopter windshield model, validation data has to be generated and subsequently used to validate the FE model.

8.2.3. Opportunities for future work

This research has opened up numerous opportunities to continue the work in the future. The author would like to address the following opportunities specifically:

Main rotor blade impact

In the risk analysis in Chapter 3, it was analysed that an impact on the windshield and main rotor of the helicopter poses the highest risk to the operator. The damage caused by a UAS collision on the windshield was predicted in this research based on the various simulation. The impact damage on the main rotor blade caused by the UAS impact was not assessed, since creating an accurate model of this part was not feasible within the given timeframe. Therefore this work can be continued by creating an accurate and validated model of a helicopter blade and subsequently simulating the impact with the UAS.

Other types of UAS

In this study, an FE model of the DJI Phantom III was created to impact the helicopter impact location. This UAS type was selected based on popularity and availability of actual test results to validate the model. The variety of UAS however is enormous and the results in this research are based on an impact of a single type of UAS. Therefore, the work of this study can be continued by assessing the damage caused by other types of UAS. For example, fixed wing UAS are based on a different design philosophy and can therefore potentially damage the helicopter in a different manner.

<div style="text-align: right;">

9

Bibliography

</div>

Accident Investigation Board Norway, (2005), *Report on the accident at Brokskar, Troms county, Norway 17 may 1999, involving Eurocopter (Aerospatiale) SA365N Dauphin 2, LN-OLT operated by Lufttransport AS,*
Available through: AIBN website [Accessed May/2019].
<http://www.aibn.no>

Air Accidents Investigation Branch, (2012), *Air accident monthly bulletin of March 2012,*
Available through: UK Government publications website [Accessed May/2020].
<https://www.gov.uk/government/collections/air-accident-monthly-bulletins#2012-monthly-bulletins>

Air Accidents Investigation Branch, (2019), *Air accident monthly bulletin of June 2019,*
Available through: UK Government publications website [Accessed May/2020].
<https://www.gov.uk/government/collections/air-accident-monthly-bulletins#2019-monthly-bulletins>

Amazon, (2020), *Amazon Prime Air first delivery,* [Image online],
Available through: Amazon Prime Air website [Accessed May/2020].
<https://www.amazon.com/Amazon-Prime-Air/b?ie=UTF8&node=8037720011>

Aviation Rulemaking Advisory Committee, (2017), *Rotorcraft Bird Strike Working Group Recommendations to the Aviation Rulemaking Advisory Committee,*
Available through: FAA website [Accessed September/2019].
<http://www.faa.gov>

Aviation Safety Network Database, (2020), *ASN Drone Database reporting suspected and confirmed drone collisions with aircraft,*
Available through: ASN online drone database [Accessed March/2020].
<https://aviation-safety.net/database/issue/drones.php>

Browne M, (2009), *Aircrag G-JSAK, 1999 Robinson R22 Beta,* [Image online],
Available through: Airport Data photo database [Accessed June/2020].
<https://www.airport-data.com/aircraft/photo/000296197.html>

Buyuk M, Kan CDS, Bedewi N, Durmus A, Ulku S, (2004), *Moving beyond the finite elements, a comparison between the finite element methods and meshless methods for ballistic impact simulation,* 8th International LS Dyna users conference May 2-4 in Dearbon USA, pp.8-81-8-96.

Cox LA, (2008), *What's wrong with risk matrices?,* Risk Analysis Vol. 28 No. 2, pp.497-512.

Cwiklak J, Grzesik N, (2016), *Numerical analysis of bird strike events with the helicopter windshield,* Journal of KONES powertrain and transport Vol. 23 No. 3, pp.85-92.

Dennis N, Lyle D, (2009), *Bird strike damage & Windshield bird strike Final report*, Version 1.1, Farnham UK: Atkings Ltd.

DJI Technology Co., (2017), *Phantom III Standard user manual*, Version 1.4.

DJI Technology Co., (2020a), *Mavic air drone follow you*, [Image online],
Available through: DJI Technology Co. website [Accessed May/2020].
<https://www.dji.com/nl/mavic-air>

DJI Technology Co., (2020b), *DJI Spark specifications*,
Available through: DJI Technology Co. website [Accessed May/2020].
<https://www.dji.com/nl/spark>

Domke B, (2006), *Sikorsky UH-60A Blackhawk Windshield viewed from ahead*, [Image online],
Available through: B Domke personal website [Accessed June/2020].
<https://b-domke.de/AviationImages/Blackhawk/10394.html>

Donea J, Huerta A, Ponthot JP, Rodriguez-Ferran A, (2004), *Arbitrary Lagrangian-Eulerian methods*,
Encyclopedia of computational mechanics, John Wiley & Sons Ltd.

Drumond T, Greco M, Cimini C, (2019), *Evaluation of increase weight in a wing fixed leading design to support UAS impact*, Proceedings of the 10th Aerospace Technology Congress 8-9 October in Stockholm Sweden, pp.71-80.

European Aviation Safety Agency, (2013), *Operational Evaluation Board Report Manufacturer: AgustaWestland A109E, A109S & AW109SP*, Final Report - Revision 1,
Available through: EASA online library [Accessed January/2020].
<https://www.easa.europa.eu/document-library>

European Aviation Safety Agency, (2018a), *Certification Specifications and Acceptable Means of Compliance for Small Rotorcraft*, CS-27 Amendment 6,
Available through: EASA regulations for initial airworthiness [Accessed May/2019].
<https://www.easa.europa.eu/regulations#regulations-initial-airworthiness>

European Aviation Safety Agency, (2018b), *Certification Specifications and Acceptable Means of Compliance for Large Rotorcraft*, CS-29 Amendment 6,
Available through: EASA regulations for initial airworthiness [Accessed May/2019].
<https://www.easa.europa.eu/regulations#regulations-initial-airworthiness>

European Commission, (2019), *Commission implementing regulation (EU) 2019/947 of 24 May 2019 on the rules and procedures for the operation of unmanned aircraft*, Official Journal of the European Union L 152, pp.45-71.

FAA Reauthorization Act of 2018, Washington, USA: 115th Congress of the United States of America.

Federal Aviation Administration, (2018a), *Advisory Circular: Certification of Normal Category Rotorcraft*, AC 27-1B Change 8,
Available through: FAA Advisory Circular library [Accessed May/2019].
<https://www.faa.gov/regulations_policies/advisory_circulars/>

Federal Aviation Administration, (2018b), *Advisory Circular: Certification of Transport Category Rotorcraft*, AC 29-2C Change 8,
Available through: FAA Advisory Circular library [Accessed May/2019].
<https://www.faa.gov/regulations_policies/advisory_circulars/>

Federal Aviation Administration, (2019a), *Airworthiness Standards: Normal Category Rotorcraft*, 14 CFR §27,
Available through: Electronic Code of Federal Regulations [Accessed May/2019].
<https://www.ecfr.gov>

Federal Aviation Administration, (2019b), *Airworthiness Standards: Transport Category Aircraft*, 14 CFR §29,
Available through: Electronic Code of Federal Regulations [Accessed May/2019].
<https://www.ecfr.gov>

Federal Aviation Administration, (2019c), *Small unmanned aircraft systems*, 14 CFR §107,
Available through: Electronic Code of Federal Regulations [Accessed May/2019].
<https://www.ecfr.gov>

Federal Aviation Administration, (2019d), *Notice of proposed rulemaking: Remote identification of Unmanned Aircraft Systems*, Federal Register Vol. 84 No. 250, pp.72438-72524.

Federal Aviation Administration, (2020), *Airspace guidance for small UAS operators*,
Available through: FAA UAS regulations website [Accessed June/2020].
<https://www.faa.gov/uas/>

Gettinger D, Michel AH, (2017), *Drone registrations a preliminary analysis*, Center for the Study of the Drone at Bard College,
Available through: CSD Bard website: [Accessed October/2019].
<https://dronecenter.bard.edu>

Gilbert G, (2017), *UK Report: Drone proximity incidents double*, Aviation International News of 30 November 2017.

Gingold RA, Monaghan JJ, (1977), *Smoothed particle hydrodynamics: theory and application to non spherical stars*, Monthly Notices of the Royal Astronomical Society Vol. 181, pp.375-389.

Global Aircraft, (2019), *2003 Agusta A109E Power*, [Image online],
Available through: Global Aircraft website [Accessed June/2020].
<http://www.globalaircrafts.com/aircraft/2003-agusta-a109e-power/>

GrabCAD, (2014), *Augusta A-109 CAD Model*,
Available through: GrabCAD website [Accessed October/2019].
<https://grabcad.com/library/augusta-a-109-1>

GrabCAD, (2015), *DJI Phantom III CAD Model*,
Available through: GrabCAD website [Accessed November/2019].
<https://grabcad.com/library/dji-phantom3-1>

Grimaldi A, (2011), *SPH high velocity impact analysis: A birdstrike windshield application*, PhD thesis at University of Naples Federico II,
Available through: University of Naples Federico II library [Accessed January/2020].
<http://www.fedoa.unina.it>

Hedayati R, Ziaei-Rad S, Eyvazian A, Hamouda AM, (2014), *Bird strike analysis on a typical helicopter windshield with different lay-ups*, Springer Journal of Mechanical Science and Technology Vol. 28 (4), pp.1382-1392.

Hu D, Song B, Wang D, Chen Z, (2016), *Experiment and numerical simulation of a full-scale heli-copter composite cockpit structure subject to a bird strike*, Elsevier Composite Structures Vol. 149, pp.385-397.

Jonkheijm L, (2019), *Literature study: Evaluation of a drone impact on a helicopter*, Version 0.4.

Kay G, (2003), *Failure modeling of titanium 6AI-4V and aluminium 2024-T3 with the Johnson-Cook material model*, Final report, Report DOT/FAA/AR-03/57, Washington D.C. USA: Federal Aviation Administration.

Leonardo Helicopters, (2020), *AgustaWestland AW109 GrandNew brochure*,
Available through: Leonardo Company website [Accessed March/2020].
<https://www.leonardocompany.com/>

Livermore Software Technology Corporation, (2018a), *LS-Dyna keyword user's manual Volume I*, Revision 11 10/12/18.

Livermore Software Technology Corporation, (2018b), *LS-Dyna keyword user's manual Volume II Material Models*, Revision 11 10/12/18.

Lucy LB, (1977), *A numerical approach to the testing of the fission hypothesis*, The Astronomical Journal Vol. 82 No. 12, pp.1013-1024.

Lyons T, D'Souza K, (2019), *Parametric study of an unmanned aerial vehicle ingestion into a business jet size fan assembly model*, Journal of Engineering for gas turbines and power Vol. 141.

May M, (2019), *Use of drones near helicopters is prohibited*, [Image online],
Available through: Sodo Null website [Accessed June/2020].
<https://www.sudonull.com/post/25896-EMI-plans-to-introduce-aircraft-drone-tests>

Meola A, (2017), *Drone market shows positive outlook with strong industry growth and trends*, Business Insider of July 13,
Available through: Business Insider website [Accessed March/2019].
<http://www.businessinsider.com/drone-industry-analysis-market-trends-growth-forecasts-2017-7>

Meng X, Sun Y, Yu J, Tang Z, Liu J, Suo T, Li Y, (2018), *Dynamic response of the horizontal stabilizer during UAS airborne collision*, Elsevier International Journal of Impact Engineering Vol. 126, pp.50-61.

Metallic Material Properties Development Standardization, (2014), *MMPDS Chapter 9*, Ed. 7, Washington D.C. USA: Battelle Memorial Institute.

National Transportation Safety Board, (2017), *NTSB aviation incident final report of incident number DCA17IA202A involving midair collision of DJI Phantom on September 21, 2017*,
Available through: NTSB Docket Management System [Accessed June/2020].
<https://dms.ntsb.gov/pubdms/>

Olivares G, Gomez L, Espinosa de los Monteros J, Baldridge RJ, Zinzuwadia C, Aldag T, (2017), *UAS Airborne collision severity evaluation - Volume II - Quadcopter*, Report DOT/FAA/AR-xx/xx, Washington D.C. USA: Federal Aviation Administration.

Ramirez F, (2014), *Bird Strike to helicopter windshield*, [Online video],
  Available through: F Ramirez youtube-channel [Accessed June/2020].
  <https://www.youtube.com/watch?v=UBhUoV8Ogj4>

Rao CL, Narayanamurthy V, Simha KRY, (2016), *Impact mechanics*, Chichester UK: John Wiley & Sons Ltd.

Rattanagraikanakorn B, Sharpanskykh A, Schuurman M, Gransden D, Blom H, de Wagter C,(2018), *Characterizing UAS Collision Consequences in Future UTM*, American Institute of Aeronautics and Astronautics Aviation forum of June 25-29 in Atlanta USA.

Robinson Helicopter Company, (2020), *Robinson's Impact-Resistant Windshields Improve Bird Strike Protection*, [Online video],
  Available through: Robinson Company youtube-channel [Accessed June/2020].
  <https://www.youtube.com/watch?v=gEvehu3ESZY>

Sahraei A, Meier J, Wierzbicki T, (2014), *Characterizing and modeling mechanical properties and onset of short circuit for three types of lithium-ion pouch cells*, Elsevier Journal of Power Sources Vol. 247, pp.503-516.

Song Y, Horton B, Bayandor J, (2017), *Investigation of UAS ingestion into high-bypass engines*, American Institute of Aeronautics and Astronautics SciTech Forum of January 9-13 in Grapevine USA.

Volocopter, (2020), *Volocopter autonomous air taxi test flight*, [Image online],
  Available through: Volocopter website [Accessed June/2020].
  <https://www.volocopter.com/>

Zukas JA, (1990), *High velocity impact dynamics*, New York USA: John Wiley & Sons Ltd.

A
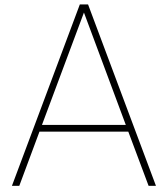
UAS mesh sensitivity analysis

In this appendix, a mesh sensitivity analysis will be performed which evaluates how the mesh size of the various DJI Phantom III components affects the result of the simulation. The aim of this analysis is to select the appropriate mesh size for each component which results in (the most) accurate results whilst simultaneously preventing an excessive required computational time. For the latter reason, a cut-off calculation time of 8 hours was selected for each simulation. For the purpose of this test, a similar target plate as further detailed in Paragraph B.1 was used. The mesh of the target plate has been varied by selecting different number of elements along the edge of the plate. As an example, the mesh of the plate with 8 elements along each edge is shown in Figure A.1. In this case the plate consisted out of 64 elements of size 890 mm / 8 = 111.25 by 111.25 mm. This appendix starts with the mesh analysis of the battery in the first paragraph, followed by the motor, camera, and main body in respectively the second, third, and fourth paragraph.
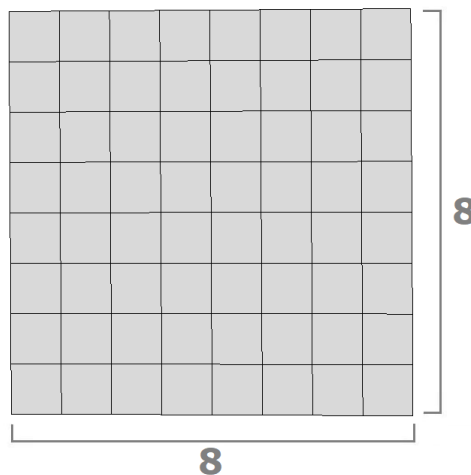
Figure A.1: *Target plate mesh example with 8 elements along each edge.*

A.1. Battery

For the battery test, the impact as further detailed in Paragraph B.2.1 has been simulated for various mesh densities of the target plate. Due to the high velocity impact and the relatively soft material properties of the battery, refer to Table 4.2, the simulation of the battery impact was prone to the following error: Negative volume and complex speed of sound in element X. This error can be present in case the Lagrangian mesh is highly distorted prior to for example deleting elements out of the calculation due to meeting the conditions of an erosion criterion. Multiple iterations were required to determine how a mesh could be created that did not suffer from this error.

The three different meshes that met this prerequisite are shown in Figure A.2 and have been compared in the mesh sensitivity analysis. For all the simulations, the time step in the analysis was governed by the mesh of the plate. Therefore the time step decreased from 2.5 microseconds for the plate with 64 elements along the edge to 310 nanoseconds for the 512 mesh. The time step sizes for

the battery were respectively 12.8 microseconds for the 5×5×30 mesh, 10.1 microseconds for the 10×10×20 mesh, and 6.4 microseconds for the 10×10×60 mesh. The slight reduction in the time step indicates that although the aspect ratio is different for the 10×10×20 mesh compared with the other two mesh compositions, there is a mesh refinement between the three.

The maximum deflection of the center of the target plate of each of this test is shown in Figure A.3. It should be noted that 0 displacement in this figure refers to a contact error in LS Dyna, which is caused by a large difference in mesh size between the two contacting bodies with a significant difference in their strength. As shown in the figure, the mesh of the plate had to be constructed out of at least 32 elements along the edge in order to be able to complete the simulation without that error. From approximately 128 elements for the 5×5×30 mesh and 256 elements for the other two mesh compositions, the solution converged since the displacement change for increasing mesh density at that stage was less than 8%. However, the converged solutions for the different mesh sizes differed significantly, namely 47.3 mm for the 10×10×20 mesh, 51.8 mm for the 5×5×30 mesh and 39.6 mm for the 10×10×60 mesh.

To analyse the cause of this difference, the visual representations of the impact of the various battery mesh constructions have been compared. In Figure A.4, the battery at 0.9 ms after the initial contact with the plate is presented for the plate meshed with 256 elements along each edge. As shown, the deformation of the battery was different in each case. For the 10×10×20 elements battery, the front side of the battery was severely distorted, whilst for the 10×10×60 elements battery additionally the back side ruptured. In both cases, the cause of these distortions were elements meeting the erosion criterion of maximum strain and resulted in multiple elements not contacting the target plate. At that stage, the 5×5×30 elements battery still had an in tact contact surface. Thereafter, also the 5×5×30 elements battery disrupted at the front and back side. The plate displacement over time during the impact for the 256 elements plate is shown in Figure A.5. It can be seen that the fact that the 5×5×30 elements battery remained in tact for a longer period of time resulted into a higher initial and subsequent deflection during the impact. Since the fact that the 5×5×30 elements battery would more closely match reality due to the more in tact contact surface and the fact that the results showed a stronger correlation with actual test data (refer to Paragraph B.4.1), the battery mesh of 5×5×30 elements will be used in the simulations of the remainder of this research.

A.2. Motor

Due to the geometrical features of the motor, the motor could only be meshed in LS Dyna by using the automatic solid mesher. When selecting a default size other than 2 mm, the PrePost processor issued an error message. Therefore only the mesh obtained by selecting a default element size of 2 mm, as presented in Figure 4.4, was analysed.

For this mesh, the impact test as further detailed in Paragraph B.3.2 was simulated for various mesh densities of the target plate. The time step calculated automatically by LS Dyna was governed by the mesh of the motor, regardless of the mesh density of the plate, and was 18 nanoseconds. The maximum deflection of the center of the plate for each simulation is presented in Figure A.6. The mesh analysis showed that the maximum deflection converged to approximately 7.4 mm from 128 elements along the plate edge and onwards. Since no other mesh could be established, the mesh with an element default size of 2 mm will be used in the remainder of this research.

A.3. Camera

Similar to meshing the motor, the camera could only be meshed in LS Dyna by the automatic solid mesher due to the structure's geometrical features. In this analysis, the results for element default sizes of 8, 4, 2, and 1 mm, as presented in Figure A.7, from the automatic mesher have been compared.

(a) *10×10×20 Elements*

(b) *5×5×30 Elements*

(c) *10×10×60 Elements*
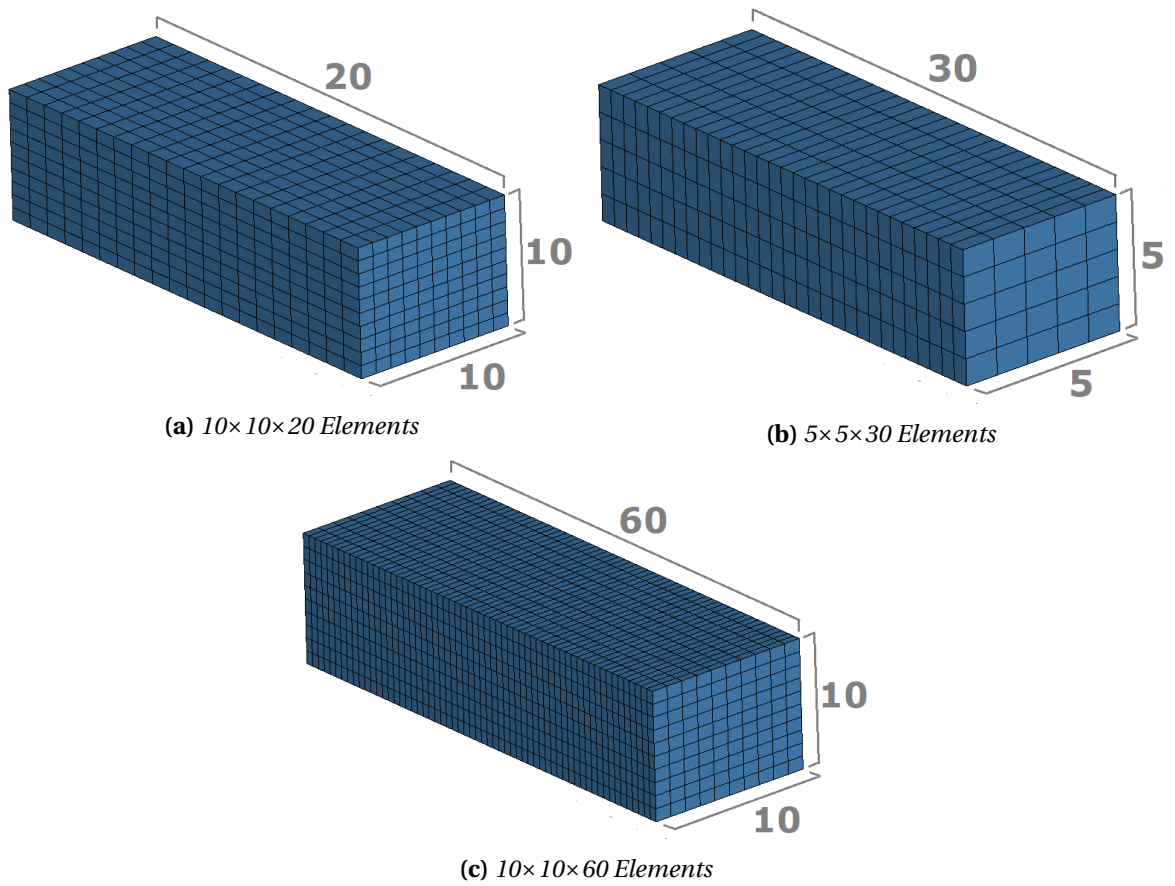
Figure A.2: *Various battery mesh sizes for the mesh sensitivity analysis.*
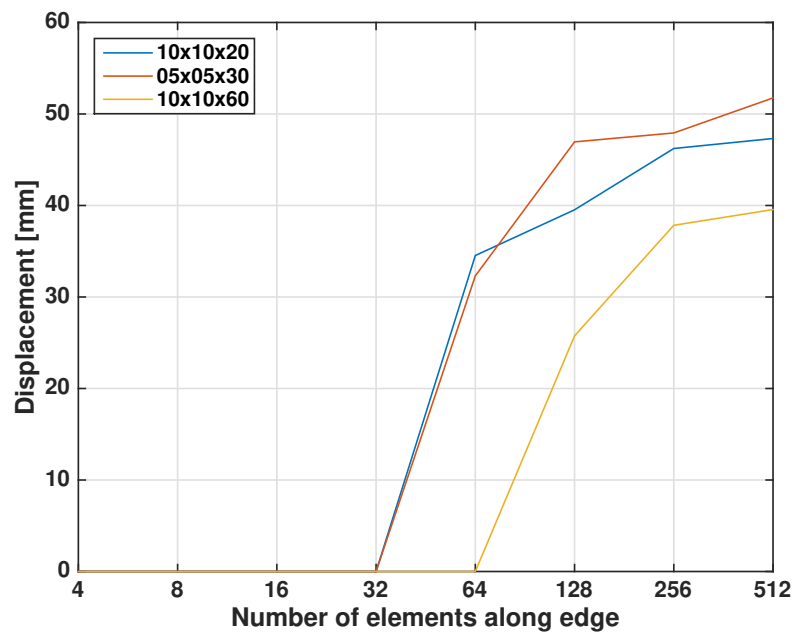
Note: 0 displacement indicates an error occurred in the calculation caused by a large difference in mesh size between the two contacting bodies.

Figure A.3: *Battery mesh sensitivity analysis.*

(a) *10×10×20 Elements*   **(b)** *5×5×30 Elements*   **(c)** *10×10×60 Elements*
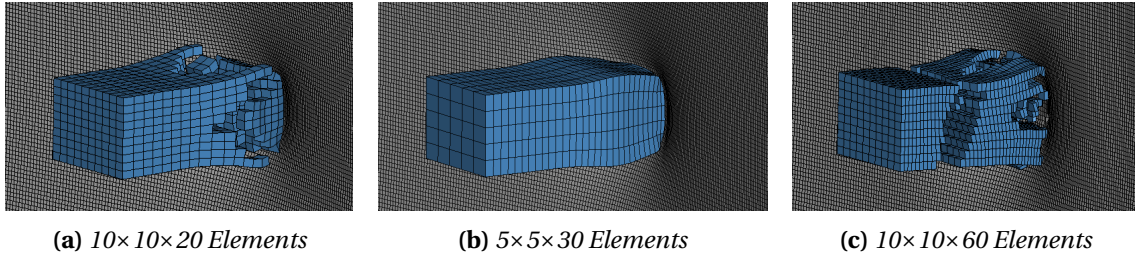
Figure A.4: *Comparison of the battery deformation of the various mesh sizes at 0.9 ms after initial contact.*
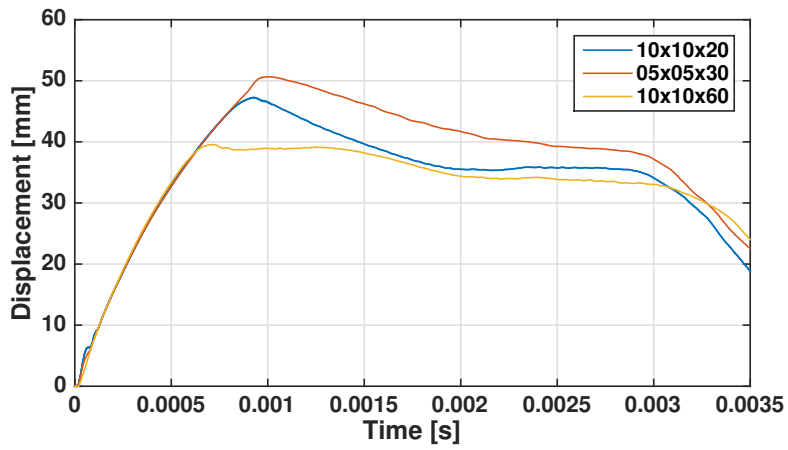
Figure A.5: *Center plate deformation over time for the various battery mesh sizes.*
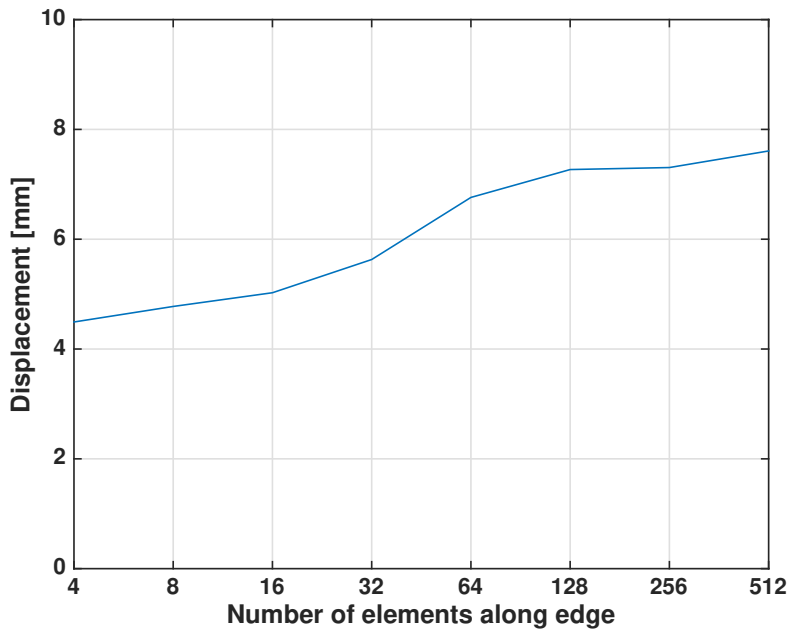
Figure A.6: *Motor mesh sensitivity analysis.*

Regardless of the mesh density of the plate, the time step calculated by LS Dyna was governed by the camera mesh for all tested camera mesh sizes. The time step was respectively 25 nanoseconds for the finest 1 mm mesh, 54 nanoseconds for the 2 mm mesh, 180 nanoseconds for the 4 mm mesh, and 200 nanoseconds for the coarsest mesh of 8 mm. This reduction in time step with decreasing default size of the automatic mesher shows that the actual resulting mesh was refined accordingly. This aspect was of importance since the correct refinement of the actual mesh was the aim of this analysis.

For these four meshes, the impact test as further detailed in Paragraph B.4.1 was simulated for different mesh densities of the target plate. The maximum plate deflection for each of this simulation is shown in Figure A.8. It can be seen in this figure that for the default element sizes of 8, 4 and 2 mm, the solution converged to approximately 18.3 mm for the plate meshed by 256 elements along the edge. For the camera mesh with element size of 1 mm, the displacement was considerably less at approximately 15 mm (relative difference of 17%) at that stage.

For the plate density of 256 elements along the edge of the plate, the displacement of the center of the plate during the impact for each of the tested camera mesh sizes is presented in Figure A.9. The difference in the displacement of the plate for the camera mesh of sizes 8, 4, and 2 mm was negligible. However as previously analysed for the 1 mm element size, this displacement was throughout the simulation considerably less. There was a potential that the solution for this test did not yet fully converge, since the mesh of the camera (1 mm) was still significantly smaller than the element size of the plate (3.5 mm). However since this simulation already required 7 hours and 40 minutes to complete, no further investigation was made to prevent an excessively long calculation time required. Additionally the other simulations showed a very strong correlation with actual test data (refer to Paragraph B.4.1). Therefore the camera meshed by elements of 1 mm was not further considered.

Increasing the mesh of the camera from 8 to 2 mm did not affect the result of the simulation, as demonstrated in the negligible difference between the results in Figure A.9. However it did considerably increase the calculation time from 30 min for the 8 mm mesh size to 1 hour 52 min for the 2 mm mesh size with the 256 element edge of the plate, which was a 370% relative increase. Therefore, in the remainder of the thesis the camera mesh constructed out of elements of 8 mm will be used.

A.4. Main body

Due to the thin-walled structure, the geometry of the main body and propellers would be represented by 2D shell elements. The means in LS Dyna to mesh a CAD model into these elements is the 2D automatic mesher. In this analysis, results for a default element size of 8, 5, and 2 mm, as shown in Figure A.10, have been compared.

The time step throughout the test was governed by the mesh of the main body, regardless of the mesh density of the plate. The time step was 81 nanoseconds for all the three different main body mesh sizes. This was caused by the fact that in order to capture the complex geometry of the main body, a very fine mesh was required in certain areas. This reduced the effect of the mesh refinement and thereby reduced the quality of this mesh sensitivity analysis. Due to the large amount of small elements within the various mesh compositions, it was not an option to manually replace these small elements with larger elements.

Since no actual impact validation test was performed by Olivares et al. (2017) for the main body, a test set-up had to be created. This test set-up was the main body impacting a 1.6 mm thick aluminium plate, similar to the one used for the actual validation tests, at 129 m/s. The shell thickness of the main body and propellers was set to 1.5 mm and non structural mass was added to the nodes through the *ELEMENT_MASS function to match the weight to 500 g as analysed in Paragraph 4.6. The maximum center plate deflection of each simulation for the various mesh sizes is depicted in Figure A.11. It can be seen that the plate deflection varies only slightly when the numbers of ele-

(a) *Element size 8 mm*   **(b)** *Element size 4 mm*

(c) *Element size 2 mm*   **(d)** *Element size 1 mm*
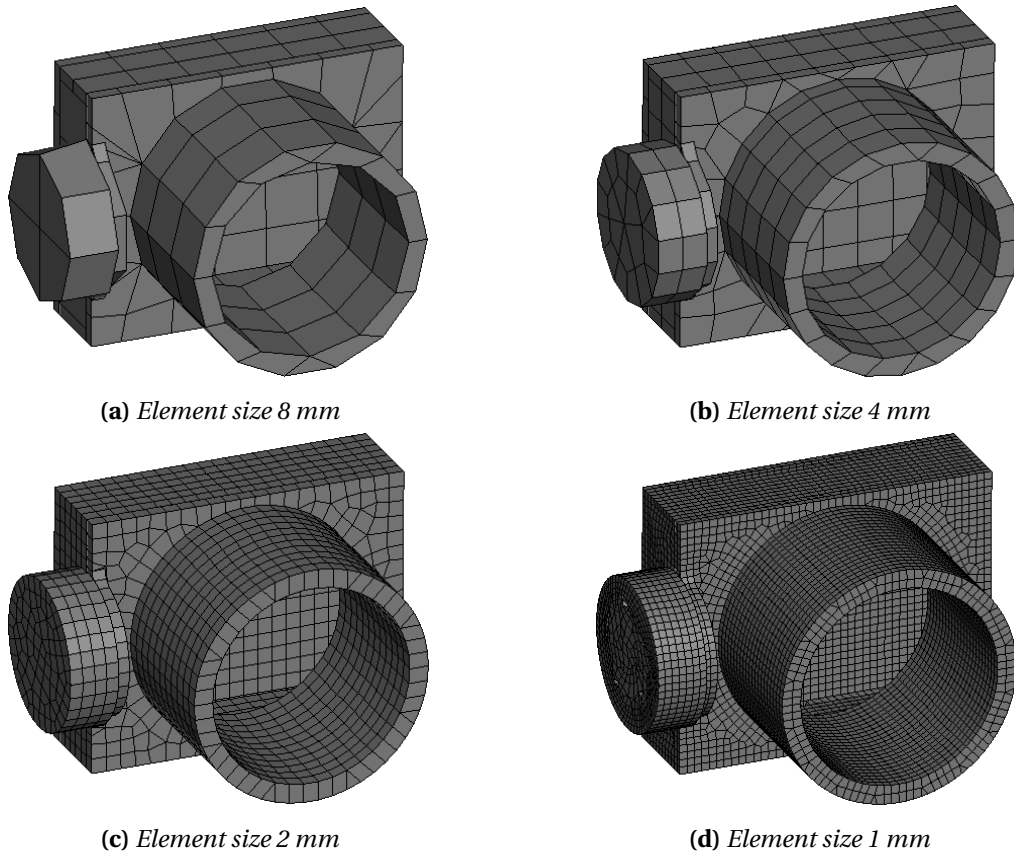
Figure A.7: *Various camera mesh sizes for the mesh sensitivity analysis.*
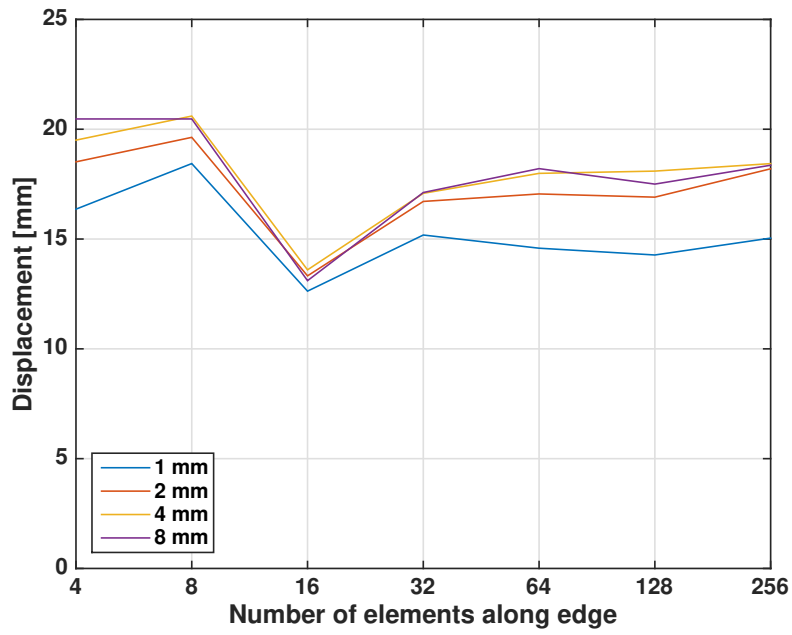
Figure A.8: *Camera mesh sensitivity analysis.*
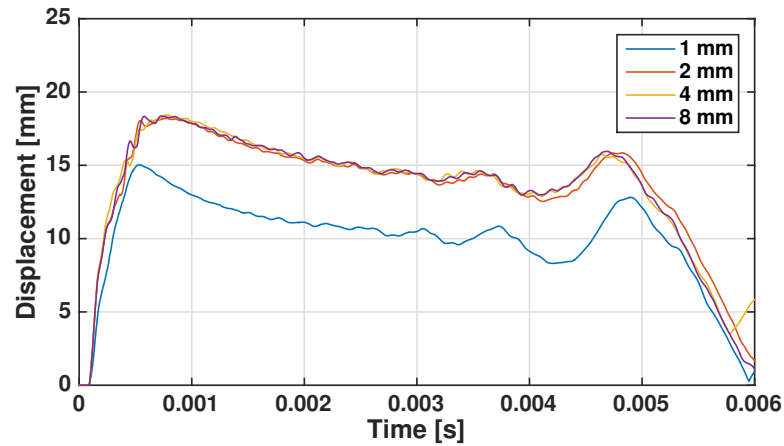
Figure A.9: *Center plate deformation over time for the various camera mesh sizes.*

ments along the edge is increased beyond 4. The solution converged to approximately 36 mm for all the three mesh sizes of the UAS main body. The maximum difference between the different mesh sizes of the main body is for 32 elements along each edge of the plate and is relatively 8%. It can be concluded that the difference in the maximum deflection is small for the various mesh sizes of the main body.

For 256 elements along each edge of the plate, the displacement of the plate's center point during the impact for each tested main body mesh size is presented in Figure A.12. As the figure indicates, the deformation of the plate shows strong similarities for the different mesh sizes. The maximum relative difference is approximately 9% at 1.8 ms, but reduces rapidly thereafter. It can therefore be stated that the difference is negligible, which is potentially caused by the fact that the mesh refinement was not very effective indicated by the constant time step. Due to fact that the mesh density does not affect accuracy of the results, the coarsest mesh is the best option in terms of computational efficiency. Therefore the main body and propellers mesh constructed out of elements of default size 8 mm is selected for the remainder of this study.

(a) *8 mm*

(b) *5 mm*

(c) *2 mm*
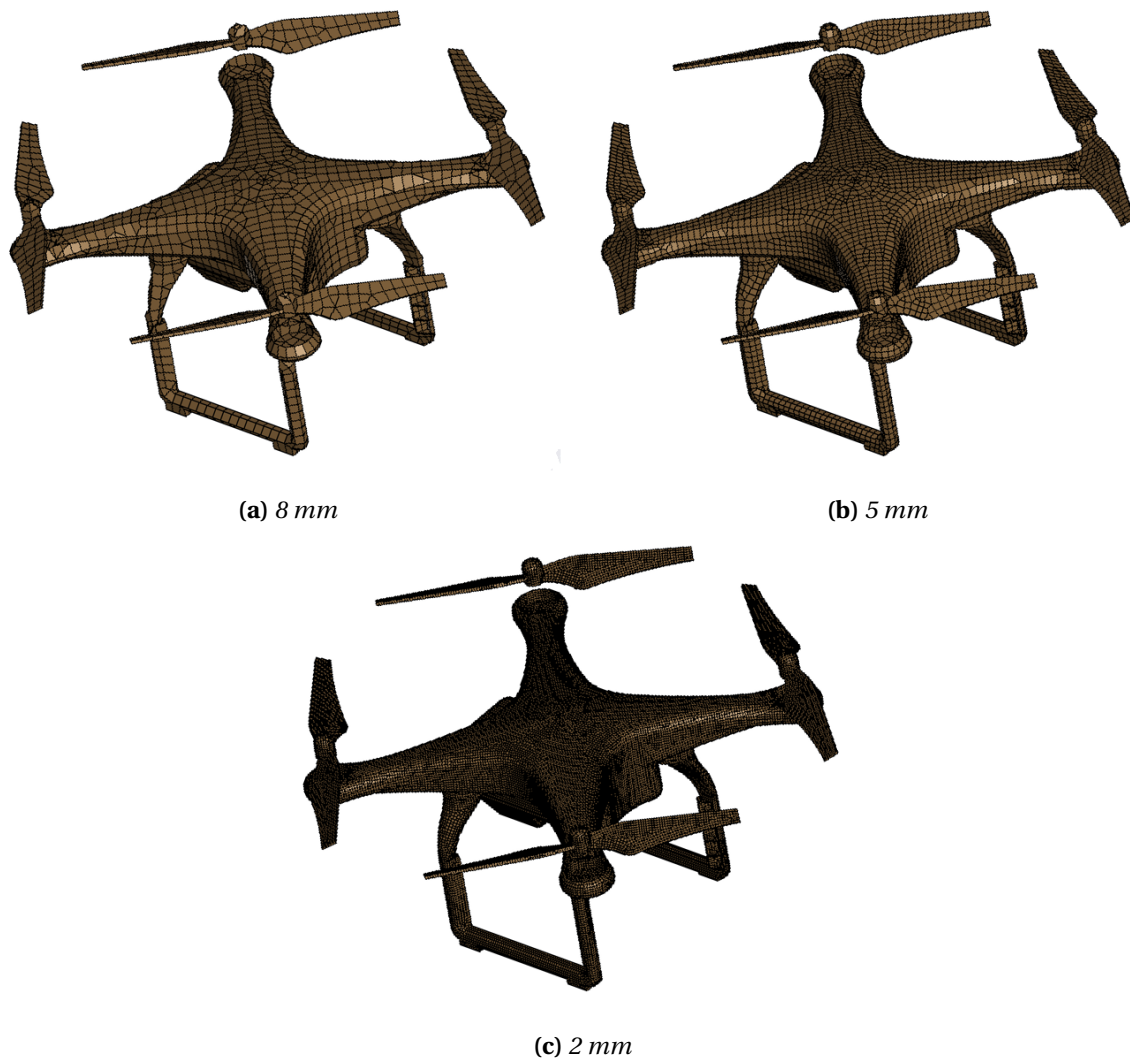
Figure A.10: *Various main body mesh sizes for the mesh sensitivity analysis.*
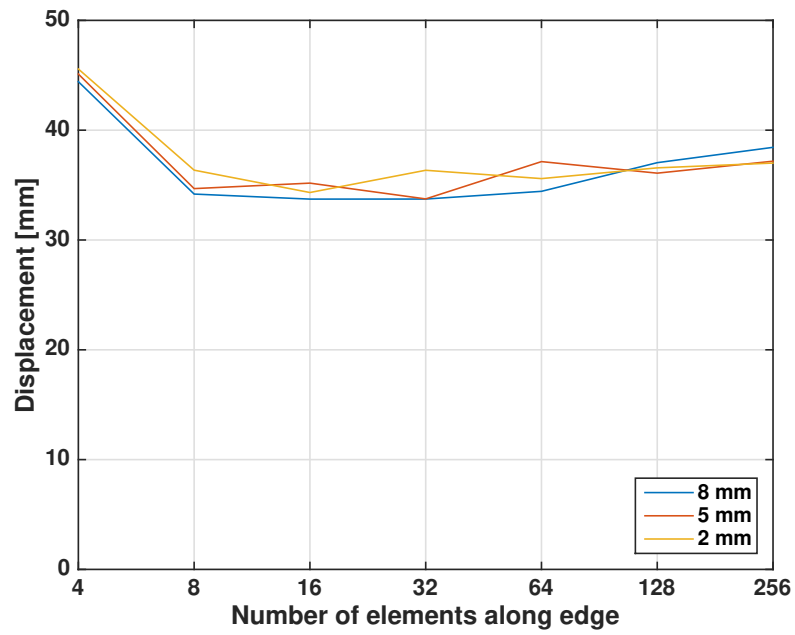
Figure A.11: *Main body mesh sensitivity analysis.*
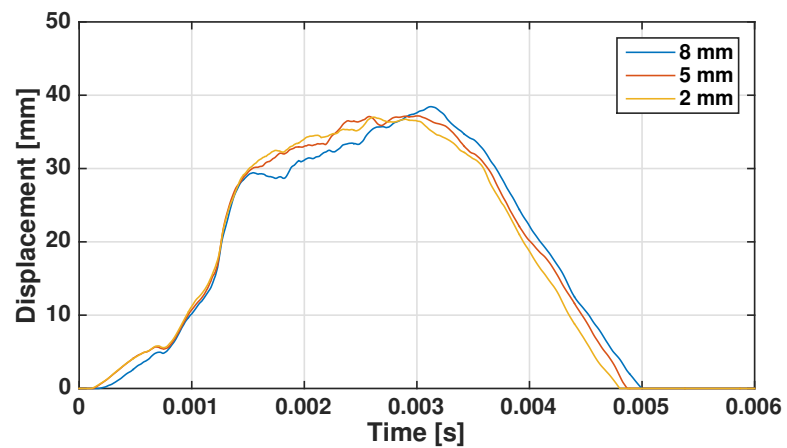
Figure A.12: *Center plate deformation over time for the various main body mesh sizes.*

<div style="text-align: right; font-size: 3em;">B</div>

UAS component validation tests

The critical components of a UAS are the battery, motor, and camera as for example analysed by Drumond, Greco, and Cimini (2019). Olivares et al. (2017) performed a number of tests impacting these critical components of the DJI Phantom III onto a flat aluminium plate. The results of these tests were comprehensively detailed in the report and were subsequently used to validate their FE model. For the same purpose, the results of the actual impact tests can be used in this study. The aim of this appendix is to assess how accurately the FE model of the critical components matches the actual test results. A summary of the test results from Olivares et al. (2017) is shown in Table B.1.

In the first paragraph in this appendix, a description is provided of the test set-up of the actual tests performed by Olivares et al. (2017) and how this test set-up has been simulated into a FE model. The subsequent paragraphs detail the validation results of the battery, the motors, and the camera in respectively the second, third, and fourth paragraph.

<div style="text-align: center;">77</div>

Table B.1: *Results of the DJI Phantom III critical components ballistic impact tests performed by Olivares et al. (2017).*

UAS component	Panel thickness [mm]	Serial	Impact velocity [m/s]	Projectile weight [g]	Penetration	Max. plate deflection [mm]
Battery	1.6	5660	133.2	344.28	No	48.5
		5669	129.24	348.86	No	49.5
		*5670	127.71	343.07	No	47.8
Battery	6.35	*5661	131.67	350.06	No	19.6
		5662	128.63	351.62	No	20.1
		5671	129.54	344.71	No	19.1
		5672	128.93	343.62	No	19.1
Battery	3.18	*5675	49.68	344.1	No	14.5
		5676	46.63	344.08	No	12.7
		5679	51.21	351.45	No	15.5
Motor	1.6	*5665	128.32	50.73	Yes	N/A
		5668	135.64	51.10	Yes	N/A
Motor	6.35	5677	121.62	51.30	No	6.9
		*5678	136.25	50.98	No	7.9
Camera	1.6	5666	131.37	52.91	No	15.2
		*5667	129.24	52.57	No	18.5

* Test serials that have been modelled in the verification process in this chapter.

B.1. Test set-up

B.1.1. Experiments

The various UAS components in Olivares et al. (2017) were impacted onto a flat aluminium alloy A2024-T3 plate of constant thickness. In the experimental set-up, the target plate was sandwiched in between two square steel frames, which were bolted together. The area of the aluminium plate inside the opening of the frames and therefore exposed to the projectile was 890 by 890 mm. Load cells were attached to the mounting frame and strain gauges to the target plate to record the loads and strains. A high speed camera recorded the impact and the displacement fields were captured by Digital Image Correlation. The projectiles were accelerated by means of a compressed gas gun system and aimed to impact the center of the panel specimen.

B.1.2. Finite Element model

The target plate was represented by a surface plane measuring 890 by 890 mm. This surface was meshed into square-shaped shell elements with a certain amount of elements along each edge of the plate as depicted in Figure A.1. The LS Dyna default 2D shell element, Belytschko-Tsay, was selected (element formulation 2) with the shear factor and through the shell thickness integration points set to the default values of respectively 0.833 and 2. Kay (2013) performed multiple verification tests to establish material properties for 2024-T3 aluminium represented by the Johnson-Cook failure strain model. These properties are detailed in Table B.2 and were implemented in the LS Dyna *MAT_JOHNSON_COOK material model (*MAT_015, LSTC, 2018b). In this material model, plasticity is strain rate and temperature sensitive. In addition, the Johnson-Cook failure model is included in this material model as well by means of the failure parameters. The surrounding structure was simplified by adding clamped boundary conditions to the edges of the target plate. For comparison with the actual test results, a visual representation of the impact as well as the displacement of the center node of the plate was generated as output of each simulation.

Table B.2: *Aluminium 2024-T3 material properties (Kay, 2013).*

Material Property	Symbol	Value	Unit
Density	ρ	2770	kg/m^3
Modulus of Elasticity	E	72	GPa
Poisson's Ratio	ν	0.33	-
Strain hardening constant	A	369.0	MPa
Strain hardening coefficient	B	684.0	MPa
Strain rate coefficient	C	0.0083	-
Thermal softening exponent	m_t	1.7	-
Strain hardening exponent	n	0.73	-

Johnson-Cook failure parameters [-]

D_1	D_2	D_3	D_4	D_5
0.112	0.123	1.500	0.007	0.0

(a) *Ballistic test results*
(Olivares et al., 2017)

(b) *FEM model simulation*
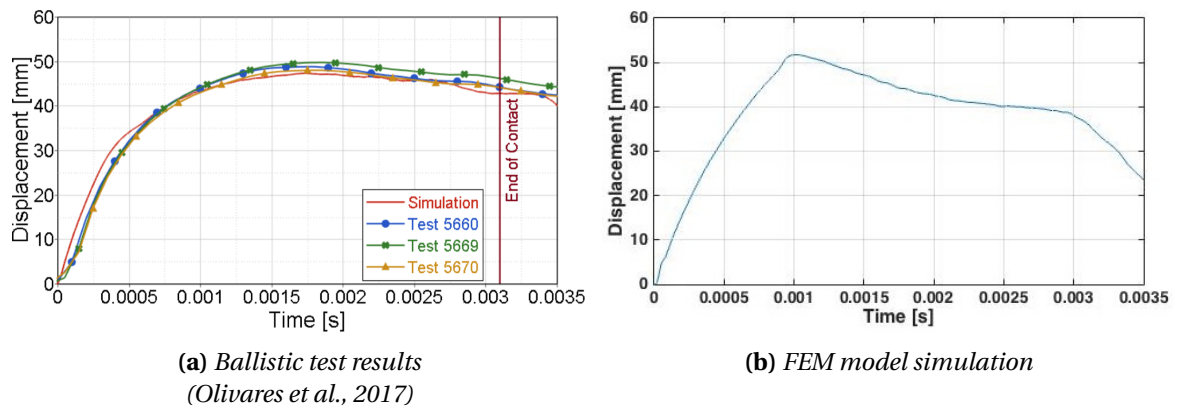
Figure B.1: *Verification of center displacement of a 1.6 mm thick A2024-T3 panel impacted by the battery at 128.6 m/s.*

B.2. Battery

B.2.1. Test 1

The target test conditions of the first battery impact test were an impact at 128.6 m/s (250 knots) on a 1.6 mm thick aluminium A2024-T3 plate. Three ballistic impact tests have been performed by Olivares et al. (2017), refer to Table B.1, of which serial 5670 had the least deviation from the target test conditions in terms of impact velocity and impact angle. Therefore, the simulation matched the impact velocity (127.71 m/s) and battery weight (343.7 g) of this test serial. In the simulation, the battery mesh consisted of 5×5×30 elements, as analysed in Paragraph A.1, and was impacted onto the plate with 512 elements along each edge.

The displacement of the center of the target plate during the impact of the ballistic test and the FE simulation are presented in Figure B.1. During the initial phase of the contact, the plate displacement in the simulation and the test corresponded by increasing up to approximately 40 mm at 0.75 ms after the initial contact. Thereafter in the ballistic test, the displacement gradually continued to increase up to a maximum displacement of 47.8 mm at approximately 1.75 ms. In the simulation in contrary, the peak displacement was reached earlier at 1 ms and was slightly over predicted at 51.8 mm, which was a relative difference of 8.4%. Subsequently the displacement in the simulation reduced to 40 mm at 2.5 ms, whilst in the actual test the displacement was approximately 6 mm larger at that time.

In Figure B.2, images of the ballistic test and the corresponding 3D plots of the simulation at 0.5 ms and 1.8 ms after start of the contact are shown. The propagation of the damage in and around the impact area and of the battery appears similar at 0.5 ms. However, at 1.8 ms a clear distinction between the way the battery has disintegrated can be observed.

As summarized above and presented in Figure B.1 and B.2, the displacement of the target plate as well as the 3D plots of the impact simulation closely matched the results of the actual ballistic test during the initial phase of the contact. However after approximately 1 ms, the results start to diverge where the initial peak displacement is slightly over predicted and the subsequent damage under predicted when comparing the simulation with the actual tests. In addition, the distinct peak in the simulation is not present in the actual test, where the displacement more gradually increases.
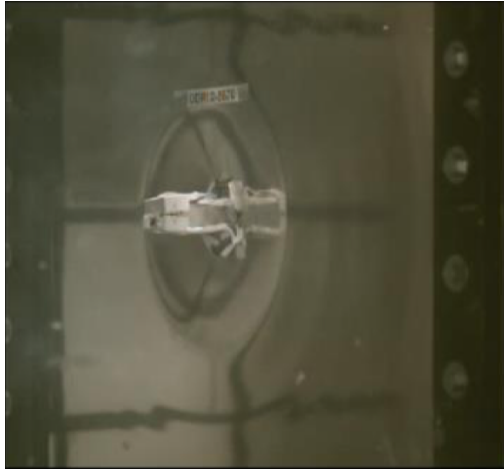
(a) *Ballistic test at 0.5 ms*
(Olivares et al., 2017)
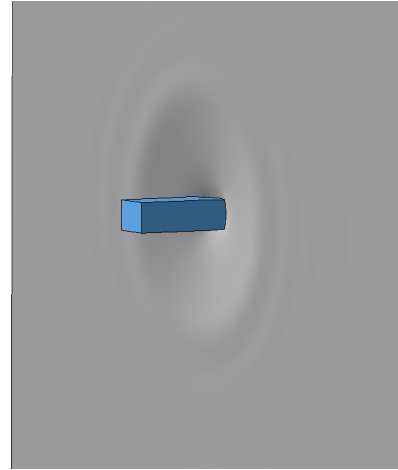
(b) *FEM model simulation at 0.5 ms*
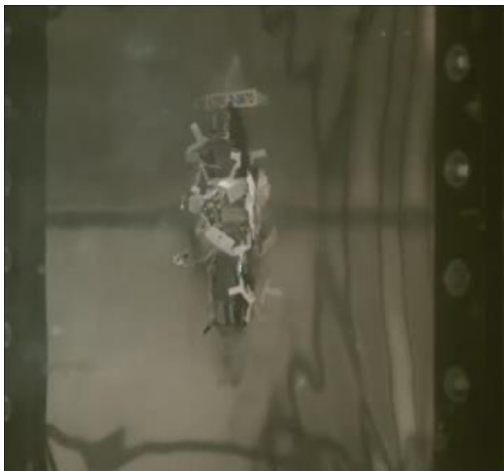
(c) *Ballistic test at 1.8 ms*
(Olivares et al., 2017)
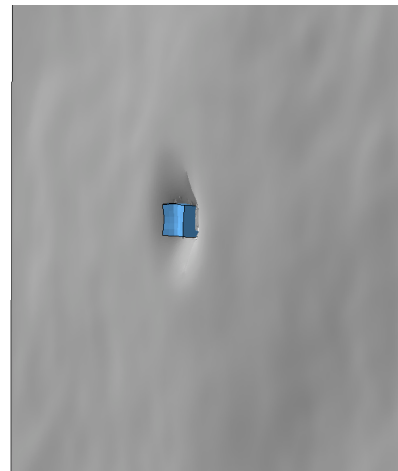
(d) *FEM model simulation at 1.8 ms*

Figure B.2: *Comparison of the damage propagation of a 1.6 mm thick A2024-T3 panel impacted by the battery at 49.7 m/s at different time intervals.*

(a) *Ballistic test results*
(Olivares et al., 2017)

(b) *FEM model simulation*
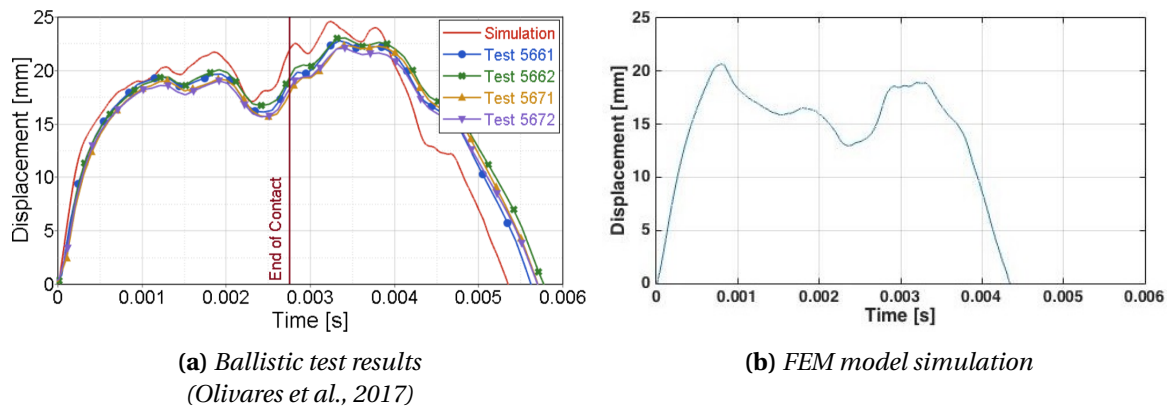
Figure B.3: *Verification of center displacement of a 6.35 mm thick A2024-T3 panel*
impacted by the battery at 128.6 m/s.

B.2.2. Test 2

The target test conditions of the second battery impact test were an impact at 128.6 m/s (250 knots) on a 6.35 mm thick aluminium A2024-T3 plate. Four ballistic impact tests have been performed by Olivares et al. (2017), refer to Table B.1, of which serial 5661 had the least deviation from the target test conditions in terms of impact velocity and impact angle. Therefore, the simulation was configured to match the impact velocity (131.67 m/s) and battery weight (350.06 g) of this test serial. In the simulation, the battery mesh consisted of 5×5×30 elements, as analysed in Paragraph A.1, and was impacted onto the plate with 512 elements along each edge.

The displacement of the center of the target plate during the impact of the ballistic test and the FE simulation are shown in Figure B.3. During the initial phase of the contact, the plate displacement in the simulation as well as in the actual test increased up to approximately 15 mm at 0.5 ms. Thereafter the plate's displacement in the simulation continued with the same rate up to 20 mm at 0.75 ms, whilst in the actual test, it more gradually increased to 20 mm at approximately 1.25 ms. Thereafter the simulation and actual test showed a similar oscillation albeit that the displacement in the simulation is approximately 4 mm less throughout. At the final stage, the simulation more rapidly decreased compared to the actual test. The maximum displacement during the contact in the simulation was 20.7 mm whilst the ballistic test recorded 19.6 mm, which is a relative difference of 5.7%.

In Figure B.4, images of the ballistic test and the corresponding 3D plots of the simulation at 0.5 ms and 2.8 ms after start of the contact are shown. The propagation of the damage in and around the impact area as well as of the battery showed strong similarities at 0.5 ms. However, at 2.8 ms a clear distinction between the way the battery has disintegrated can be observed.

As summarized above and presented in Figure B.3 and B.4, the displacement of the target plate as well as the visual representation of the impact simulation closely matched the results of the actual ballistic test during the initial phase of the contact. However after approximately 0.75 ms, the results started to diverge where the damage in the simulation was less than in the actual tests. In addition, the distinct peak in the simulation is not present in the actual test, where the displacement more gradually increases.

B.2.3. Test 3

The target test conditions of the third battery impact test were an impact velocity of 51.4 m/s (100 knots) on a 3.18 mm thick aluminium A2024-T3 plate. Three ballistic impact tests have been performed by Olivares et al. (2017), refer to Table B.1, of which serial 5675 had the least deviation from the target test conditions in terms of impact velocity and impact angle. Therefore, the simulation was configured to match the impact velocity (49.68 m/s) and battery weight (344.1 g) of this test

(a) *Ballistic test at 0.5 ms
(Olivares et al., 2017)*
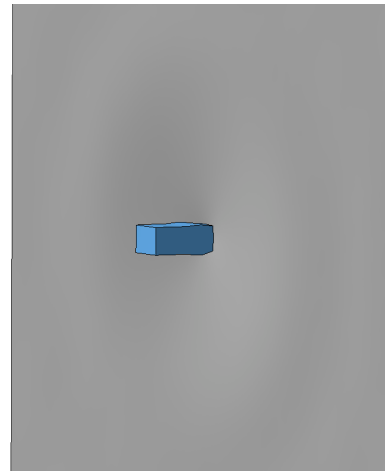
(b) *FEM model simulation at 0.5 ms*
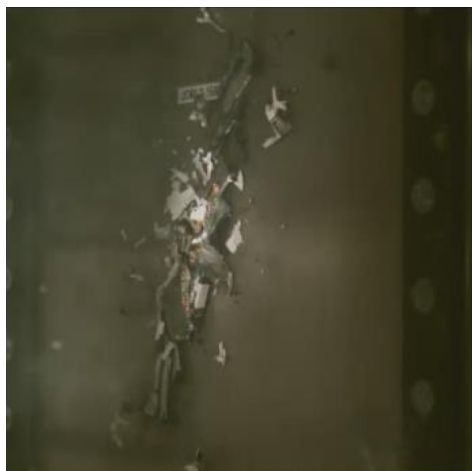
(c) *Ballistic test at 2.8 ms
(Olivares et al., 2017)*
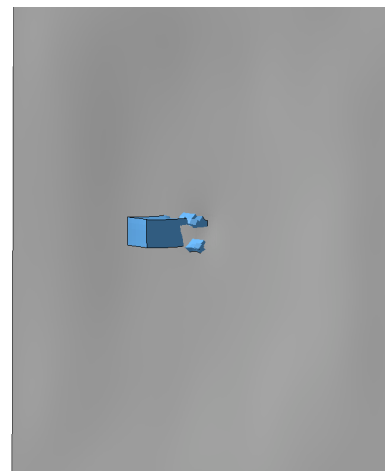
(d) *FEM model simulation at 2.8 ms*

Figure B.4: *Comparison of the damage propagation of a 6.35 mm thick A2024-T3 panel
impacted by the battery at 128.6 m/s at different time intervals.*

(a) *Ballistic test results (Olivares et al., 2017)*

(b) *FEM model simulation*
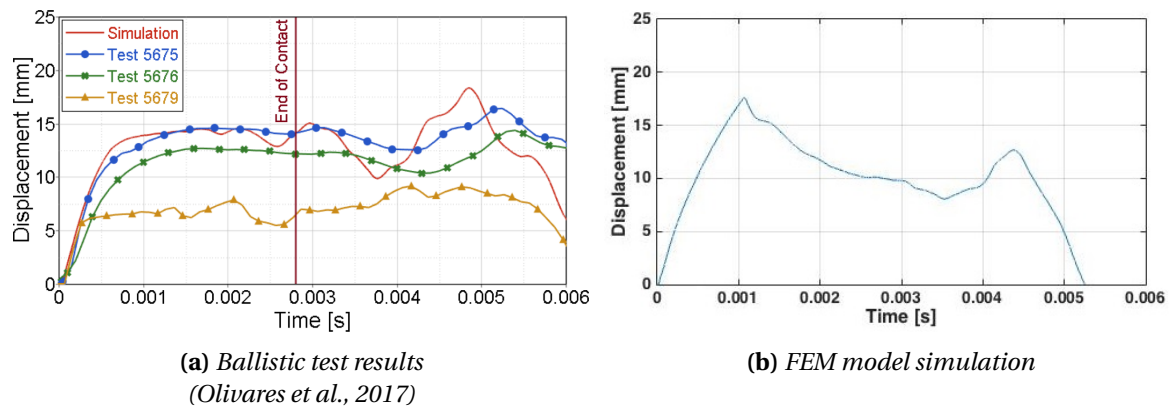
Figure B.5: *Verification of center displacement of a 3.18 mm thick A2024-T3 panel impacted by the battery at 49.7 m/s.*

serial. In the simulation, the battery mesh consisted of 5×5×30 elements, as analysed in Paragraph A.1, and was impacted onto the plate with 512 elements along each edge.

The displacement of the center of the target plate during the impact of the ballistic test and the FE simulation are shown in Figure B.5. During the initial phase of the contact, the plate displacement in the simulation as well as in the actual ballistic tests increased up to approximately 13 mm at 0.75 ms. Thereafter the plate's displacement in the simulation continued with the same rate up to 17 mm at 1.1 ms, whilst in the actual test, it more gradually increased to 15 mm at approximately 1.5 ms. Thereafter, the plate displacement in the simulation decreased to approximately 8 mm at 3.5 ms, whilst in the actual test the displacement remained approximately 13 mm up to that point. At the final stage, the simulation more quickly decreased compared to the actual test. The maximum displacement during the contact in the simulation was 17.6 mm whilst the ballistic test recorded 14.5 mm, which is a relative difference of 21.4%.

In Figure B.6, images of the ballistic test and the corresponding 3D plots of the simulation at 0.5 ms and 2.8 ms after start of the contact are shown. The propagation of the damage in and around the impact area as well as of the battery showed strong similarities at 0.5 ms. However, at 2.8 ms a clear distinction between the way the battery has disintegrated was observed.

As summarized above and presented in Figure B.5 and B.6, the displacement of the target plate as well as the visual representation of the impact simulation reasonably matched the results of the actual ballistic test during the initial phase of the contact. However after approximately 0.75 ms, the results started to diverge where the damage in the simulation was less than in the actual tests. In addition, the distinct peak in the simulation is not present in the actual test, where the displacement more gradually increases.

B.2.4. Conclusion

In all three tests, the plate displacement and the visual representation of the impact closely matched during the initial phase of contact. Particularly the maximum displacement at the higher velocity tests showed a close correlation with the actual tests with respectively 8.4 and 5.7% relative difference. However, the displacement of the plate in the simulation subsequently started to diverge from the actual test results and was consistently less. This was possibly caused by the fact that only the battery itself had been modelled and the battery's casing was omitted, refer to Figure 4.3. Due to the soft material properties of the battery compared to the target plate, refer to Table 4.2, the elements underwent large deformations. This caused the incorporated erosion criterion to delete some elements from the equation prior to contacting the target. This additionally could explain why the plate's deflection in the simulation was less when compared to the actual test after the initial phase. In conclusion, it should be taken into account in the remainder of the simulations in this report

(a) *Ballistic test at 0.5 ms (Olivares et al., 2017)*
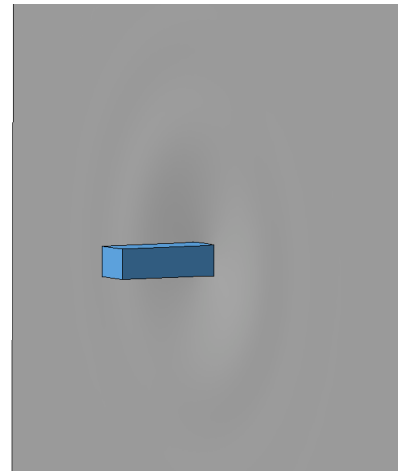
(b) *FEM model simulation at 0.5 ms*

(c) *Ballistic test at 2.8 ms (Olivares et al., 2017)*
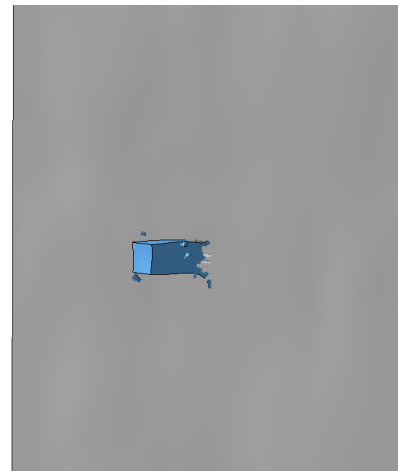
(d) *FEM model simulation at 2.8 ms*

Figure B.6: *Comparison of the damage propagation of a 3.18 mm thick A2024-T3 panel impacted by the battery at 49.7 m/s at different time intervals.*

that the damage caused by the battery could be under predicted. To improve the battery FE model, the casing could be incorporated into the model. Additionally, a different numerical mesh can be used, which can more accurately represent a severely distorted specimen. An option is to use the meshless SPH method, as described in Paragraph 2.2.2. Softening at high strain rates can be introduced to reduce the distinct peak displacement in the simulation, which is not present in the actual test results. This however could lead to certain elements reaching the erosion criterion in an earlier phase, thereby potentially deviating more from the actual test results at a later stage.

B.3. Motor

B.3.1. Test 1

The target test conditions of the first motor impact test were an impact velocity of 128.6 m/s (250 knots) on a 1.6 mm thick aluminium A2024-T3 plate. Two ballistic impact tests have been performed by Olivares et al. (2017), refer to Table B.1, of which serial 5665 had the least deviation from the target test conditions in terms of impact velocity and impact angle. Therefore, the simulation was configured to match the impact velocity (128.32 m/s) and motor weight (50.73 g) of this test serial. For the validation simulation, the plate was constructed out of 512 elements along each edge.

Since the motor penetrated the center of the plate, the displacement of this point could not be recorded. Therefore a comparison between the images of the ballistic test and the corresponding 3D plots of the simulation at time 0.2 and 1 ms after the initial contact was made as presented in Figure B.7. The figure showed that the shockwaves propagating through the plate were accurately captured by the simulation. The motor damaged the plate by cutting an opening and subsequently penetrating through this opening in the simulation and the actual ballistic test. The FE simulation showed a strong correlation with the ballistic test in capturing the damage propagation and penetration of the motor.

B.3.2. Test 2

The target test conditions of the second motor impact test were an impact velocity of 128.6 m/s (250 knots) on a 6.35 mm thick aluminium A2024-T3 plate. Two ballistic impact tests have been performed by Olivares et al. (2017), refer to Table B.1, of which serial 5678 had the least deviation from the target test conditions in terms of impact velocity and impact angle. Therefore, the simulation was configured to match the impact velocity (136.25 m/s) and motor weight (50.98 g) of this test serial. For the validation simulation, the plate was constructed out of 512 elements along each edge.

The displacement of the center of the target plate during the impact of the ballistic test and the FE simulation have been presented in Figure B.8. During the contact, the displacement increased up to approximately 7 mm for both the simulation and the ballistic test. After two troughs and one peak, the maximum displacement of the plate was reached at approximately 2 ms. The maximum displacement of the ballistic test was measured at 7.9 mm whilst the simulation recorded 7.6 mm, which is a relative difference of 3.8%. Throughout the test period, the displacement of the plate in the simulation closely matched the ballistic test results.

In Figure B.9, images of the ballistic test and the corresponding 3D plots of the simulation at 0.3 ms after the initial contact are shown. The propagation of the damage in and around the impact area of both tests showed strong similarities. In addition, the contact between the two bodies as well as the shockwaves propagating through the plate were captured accurately. Qualitatively assessed, the FE simulation showed good correspondence with the results of the ballistic tests.

As summarized above and presented in Figure B.8 and B.9, the displacement of the target plate as well as the visual representation of the impact simulation closely matched the results of the actual ballistic test. Therefore, it can be concluded that the results of the FEM model simulation showed a strong correlation with the results of this ballistic test.

(a) *Ballistic test at 0.2 ms (Olivares et al., 2017)*
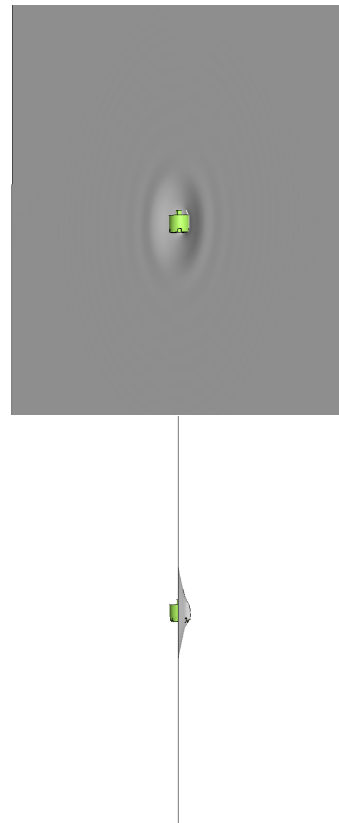
(b) *FEM model simulation at 0.2 ms*

(c) *Ballistic test at 1 ms (Olivares et al., 2017)*
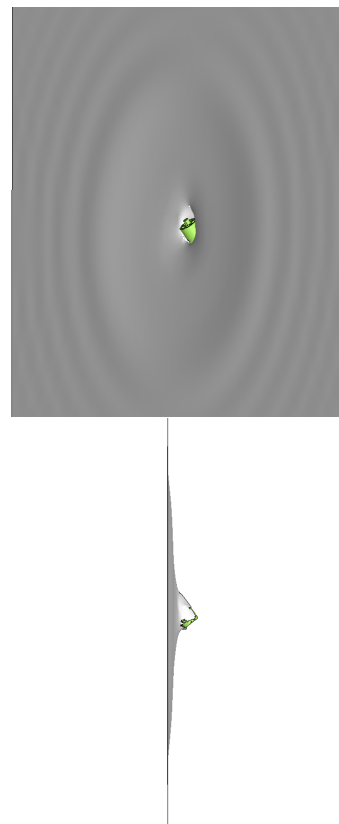
(d) *FEM model simulation at 1 ms*

Figure B.7: *Comparison of the damage propagation of a 1.6 mm thick A2024-T3 panel impacted by the motor at 128.6 m/s at different time intervals.*

(a) *Ballistic test results*
(Olivares et al., 2017)

(b) *FEM model simulation*
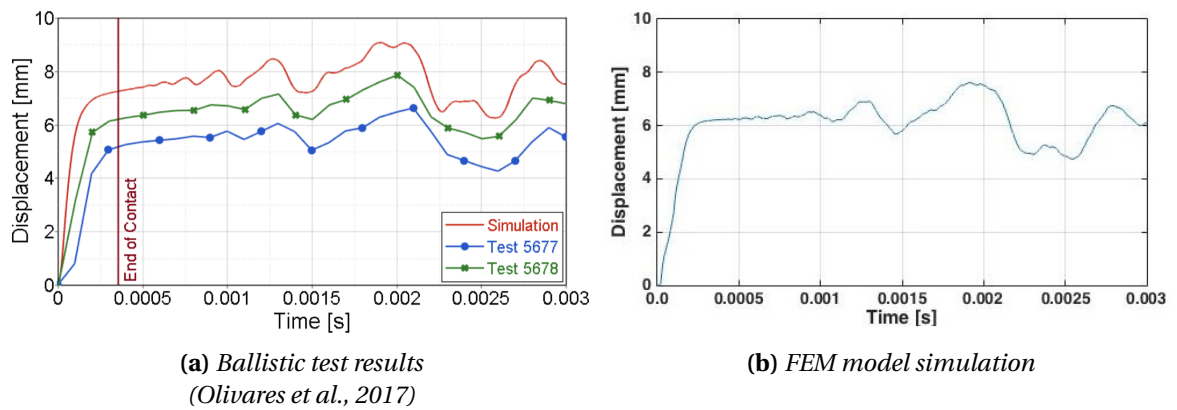
Figure B.8: *Verification of center displacement of a 6.35 mm thick A2024-T3 panel impacted by the motor at 128.6 m/s.*

(a) *Ballistic test at 0.3 ms*
(Olivares et al., 2017)
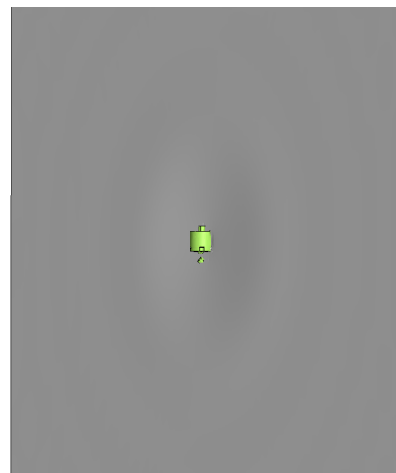
(b) *FEM model simulation at 0.3 ms*

Figure B.9: *Comparison of the damage propagation of a 6.35 mm thick A2024-T3 panel impacted by the motor at 128.6 m/s at different time intervals.*

B.3.3. Conclusion

For both the motor tests, the simulation showed a strong correlation with the results of the actual ballistic tests. The panel displacement as well as the graphical representations of the impact showed a close match for both the tests. Additionally, the contact between the two bodies was accurately captured. Therefore, it can be assumed that the damage caused by the motor(s) in the remaining simulations in this report would closely match reality.

B.4. Camera

B.4.1. Test 1

The target test conditions of the camera impact test were an impact velocity of 128.6 m/s (250 knots) on a 1.6 mm thick aluminium A2024-T3 plate. Two ballistic impact tests have been performed by Olivares et al. (2017), refer to Table B.1, of which serial 5667 had the least deviation from the target test conditions in terms of impact velocity and impact angle. Therefore, the simulation was configured to match the impact velocity (129.24 m/s) and weight (52.57 g) of this test serial. The target plate was constructed out of 256 elements along each edge and the camera model with the 8 mm mesh was selected, as analysed in Paragraph A.3.

The displacement of the center of the target plate during the impact of the ballistic test and the FE simulation have been presented in Figure B.10. During the contact, the displacement increased up to the maximum displacement at 0.5 ms after the impact. This maximum displacement was 18.5 mm in the ballistic test and 18.1 mm in the simulation, which is a relative difference of 2.2% between the two. Subsequently, the displacement in the simulation decreased to approximately 12.5 mm before increasing back to 16 mm at 4.7 ms. The corresponding displacement during the actual ballistic tests was approximately 11 mm before increasing back to 16 mm at 5.8 ms. Throughout the test period, the displacement of the plate in the simulation closely matched the ballistic test results. Albeit that at the end of the test, the simulation precedes the actual test by approximately a millisecond.

In Figure B.11, images of the ballistic test and the corresponding 3D plots of the simulation at 2 and 5 ms after the initial contact are shown. The propagation of the damage in and around the impact area of both tests showed strong similarities. In addition, the contact between the two bodies as well as the shockwaves propagating through the plate were captured accurately. Qualitatively assessed, the FE simulation showed good correspondence with the results of the ballistic tests.

As summarized above and presented in Figure B.10 and B.11, the displacement of the target plate as well as the 3D plots of the impact simulation closely matched the results of the actual ballistic test. Therefore, it can be concluded that the results of the FEM model simulation showed a good correlation with the results of this ballistic test.
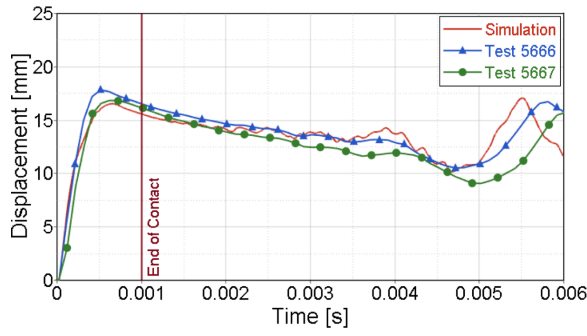
(a) *Ballistic test results (Olivares et al., 2017)*
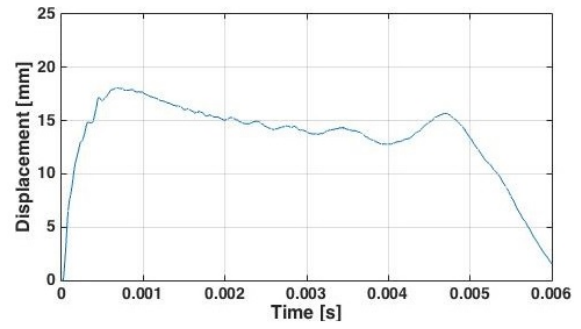
(b) *FEM model simulation*

Figure B.10: *Verification of center displacement of a 1.6 mm thick A2024-T3 panel impacted by the camera at 128.6 m/s.*

(a) *Ballistic test at 0.2 ms (Olivares et al., 2017)*
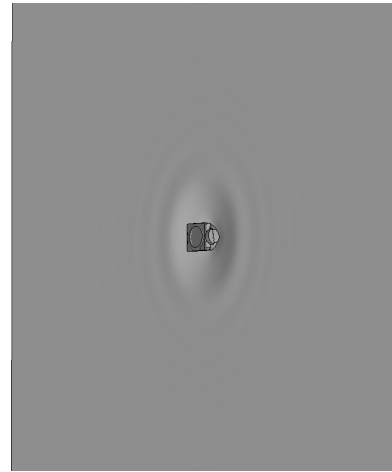
(b) *FEM model simulation at 0.2 ms*

(c) *Ballistic test at 0.5 ms (Olivares et al., 2017)*
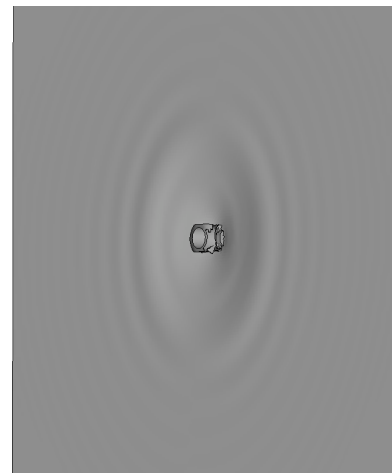
(d) *FEM model simulation at 0.5 ms*

Figure B.11: *Comparison of the damage propagation of a 1.6 mm thick A2024-T3 panel impacted by the camera at 128.6 m/s at different time intervals.*

B.4.2. Conclusion

For the camera impact test, the simulation showed good correlation with the results of the actual ballistic test. The panel displacement as well as the graphical representations of the impact matched closely. In addition, the contact between the two bodies was accurately captured. Therefore, it can be assumed that the damage caused by the camera in the remaining simulations in this report would closely match reality.

Helicopter windshield bird strike analysis

How the FE model of the A-109 windshield was made, is detailed in Chapter 5. As explained in that chapter, the thickness of the windshield remained a variable in that process. The literature review in Paragraph 2.4 pointed out that results of validation tests of windshield bird strikes were not freely available or could not be easily simulated in FE software. As an alternative approach to determine a representative thickness of the windshield, it was decided to perform simulations to assess when the windshield would comply with the certification requirements of CS (EASA, 2018b) and FAA 14 CFR (FAA, 2019b) §29.631. This approach is similar to the procedure as detailed in the report of Hedeyati et al. (2014). The aim of this appendix is therefore to determine the minimum thickness of the windshield FE model at which the simulation complies with the certification requirements.

The first paragraph in this appendix will describe the test set-up of the FE simulation for the bird strike event and the results of these simulations are detailed in the second paragraph. Conclusions and recommendations to improve the analysis have been included in the third and last paragraph of this appendix.

C.1. Test set-up

C.1.1. Bird SPH model

In the simulations, the SPH bird model as detailed in the report of Grimaldi (2011) was implemented. The geometry of the bird was simplified by a cylindrical shape with a length to diameter ratio of 2:1 and a mass density of $\rho = 950 \ kg/m^3$. The SPH model is shown in Figure C.1 and consisted of 12640 nodes. Since the weight W of the bird had to be 1 kg in accordance with the certification requirements, the diameter d and length l of the cylinder were calculated as follows:

$$d = \sqrt[3]{\frac{2W}{\pi\rho}} = 8.75 \ cm$$

$$l = 2d = 17.5 \ cm$$

The selected material model for the substance of the bird was the LS Dyna *MAT_NULL card. This model allows equations of state to be considered without computing deviatoric stresses (*MAT_009, LSTC, 2018b). The Equation Of State (EOS) added to this material model was the *EOS_TABULATED in which the pressure P is calculated as follows:

$$P = C(\epsilon_V) + \gamma \, T(\epsilon_V) E$$

In this equation is E the internal energy per initial volume and γ the ratio of specific heat. $C(\epsilon_V)$ and $T(\epsilon_V)$ are the tabulated pressure and temperature as a function of the volumetric strain ϵ_V. LS Dyna linearly interpolates between the user defined tabulated values of $C(\epsilon_V)$ and $T(\epsilon_V)$. The temperature dependency was neglected in this simulation, therefore only the EOS parameters for the bird as listed in Table C.1 were inserted. Note that pressure is positive in compression in this EOS, which explains that negative volumetric strain (ϵ_V) equates to positive values of $C(\epsilon_V)$.
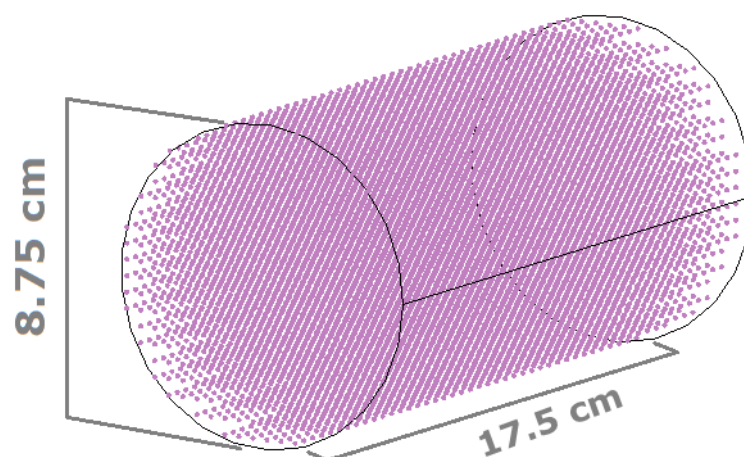
Figure C.1: *Bird SPH model.*

Table C.1: *Bird tabulated equation of state parameters (Grimaldi, 2011).*

ϵ_V [-]	C [MPa]	ϵ_V [-]	C [MPa]
0	0	-0.154	972
-0.105	237	-0.169	1180
-0.118	425	-0.183	1370
-0.128	586	-0.195	1540
-0.137	727	-0.217	1840

C.1.2. Parameters of the simulation

In the simulations, the default size for the mesh of the windshield was set to 7 mm, refer to Figure 5.3a. The impact location of the bird onto the windshield was vertically centered and horizontally slightly left of center when viewed from the front. At this location, the distance to the edge was the largest whilst the windshield's orientation was most perpendicular to the direction of motion of the bird. The expected damage was therefore the largest when the bird strike occurred at that location. An overview of the simulation is shown in Figure C.2. Note that the surrounding structure was not incorporated in the FE model and is only shown in this figure to help the reader in understanding the orientation of Figure C.4 and C.6 in the next paragraph. Tests have been completed for the two configurations of boundary conditions as detailed in Paragrah 5.5. The initial velocity of the bird was set to 80 m/s, as defined in Paragraph 5.6, to assess compliance with the certification requirements.

To define the contact between the SPH nodes and the Lagrangian elements of the windshield, the *CONTACT_AUTOMATIC_NODES_TO_SURFACE algorithm was implemented. This algorithm establishes contact when nodes of one part penetrate a target surface of the other part (LSTC, 2018a). It is particularly suitable when contact between SPH particles and element-based parts is present, which is the case in this simulation. The contact card is penalty-based and non-oriented (automatic) therefore capable of detecting penetration coming from either side of the element.
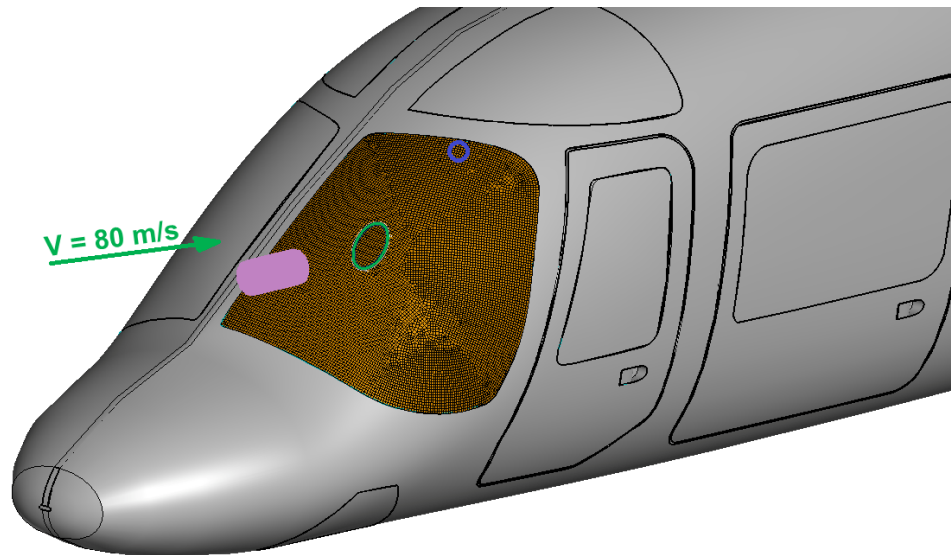
● Impact location of the bird.
● Point at which displacement was recorded.
Note: The windshield surrounding structure is only displayed for visualization purposes and was not
incorporated in the simulation.

Figure C.2: *Windshield bird strike simulation overview.*

C.2. Thickness analysis

C.2.1. Clamped boundary conditions

For the clamped boundary conditions, the bird strike simulation was completed for various thicknesses of the windshield ranging from 7.0 up to 9.3 mm. The thickness was increased in 0.1 mm increments up to the point that the bird no longer penetrated the structure and the windshield's material did not break into dangerous fragments. The displacement over time of the center top point of the windshield as pointed in Figure C.2 is shown in Figure C.3. A positive displacement equates to the point moving inwards into the cockpit i.e. towards the tail of the aircraft. The damage propagation of the various windshields at 6 ms and 12 ms after the initial contact is visually represented in Figure C.4. The orientation of the windshield in this figure with respect to the surrounding structure is depicted in the bird strike overview Figure C.2.

For the 7.0 and 8.0 mm thick windshield, the entire top part of the windshield ruptured. A significant part of the nodes of the bird penetrated the windshield and fragments of the acrylic moved inwards. This would result in both these objects entering the cockpit. The bird was deflected off the 9.0 mm thick windshield such that it did not penetrate the window. However, the top part of the windshield broke into dangerous fragments, which would displace into the cockpit. The velocity at which these elements moved inwards was lower and the fragments were smaller in size compared to the cases with the thinner windshields. For a thickness of 9.3 mm, the bird did not penetrate the windshield and the windshield remained in tact throughout the simulation.

C.2.2. Alternative boundary conditions

The bird strike simulation was completed for various thicknesses of the windshield ranging from 6.0 up to 7.0 mm with 0.1 mm increments for the alternative boundary conditions. The displacement over time of the center top point of the windshield as pointed in Figure C.2 is shown in Figure C.5. A positive displacement equates to the point moving downwards i.e. towards the bottom of the aircraft. The damage propagation of the various windshields at 6 ms and 12 ms after the initial
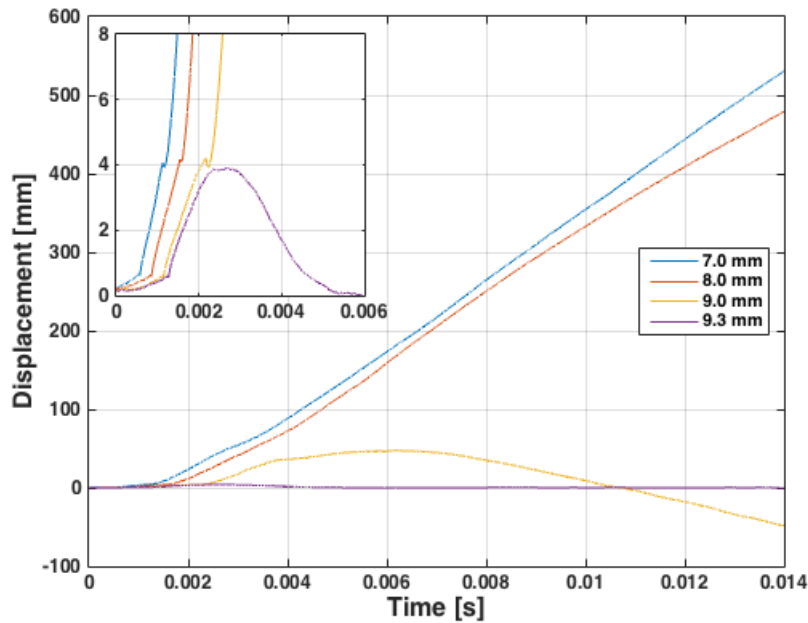
Figure C.3: *Comparison of the displacement of the top center windshield with the clamped boundary conditions over time for various windshield thicknesses.*

contact is visually represented in Figure C.6. The orientation of the windshield in this figure with respect to the surrounding structure is depicted in the bird strike overview Figure C.2.

For a thickness of 6.6 and 7.0 mm, the top part of the windshield initially moves approximately 80 mm downwards and subsequently springs back to the original shape. A sudden change in the magnitude of displacement was present for windshields thinner than 6.6 mm. The downwards movement of the top part of the windshield increased to approximately 150 mm for a thickness of 6.0 and 6.5 mm. Additionally, a crack propagated along the width of the windshield at the top part, which resulted in the windshield not returning back to its original shape. The magnitude of the displacement of the top of the windshield would be such that the assumptions on which the alternative boundary conditions are based, refer to Paragraph 5.5, would no longer be valid. It can be concluded that these deformations would in reality cause the windshield to break and no longer comply with the certification requirements. Therefore, the thickness of the windshield should at least 6.6 mm.

C.3. Conclusion

The aim of this appendix was to determine the minimum thickness of the windshield at which it would comply with the certification requirements. A number of simulations have been performed with an SPH bird model impacting an acrylic windshield of the A-109. With the boundary conditions clamping the edges of the windshield, a 9.3 mm thick windshield would not break into dangerous fragments and the bird would be deflected away from the cockpit. For the alternative boundary conditions, the windshield should be at least 6.6 mm thick in order to remain in tact and for the boundary conditions to remain valid. The windshield in the simulations with these thicknesses would therefore comply with the certification standards. It should be noted that this conclusion is based on the simulations only and no validation of the bird model or windshield was performed. It is therefore recommended to conduct an actual windshield bird strike test and subsequently use the results of this test to validate the model.

(a) *Thickness 7.0 mm at 6 ms*

(b) *Thickness 7.0 mm at 12 ms*

(c) *Thickness 8.0 mm at 6 ms*

(d) *Thickness 8.0 mm at 12 ms*

(e) *Thickness 9.0 mm at 6 ms*

(f) *Thickness 9.0 mm at 12 ms*

(g) *Thickness 9.3 mm at 6 ms*

(h) *Thickness 9.3 mm at 12 ms*
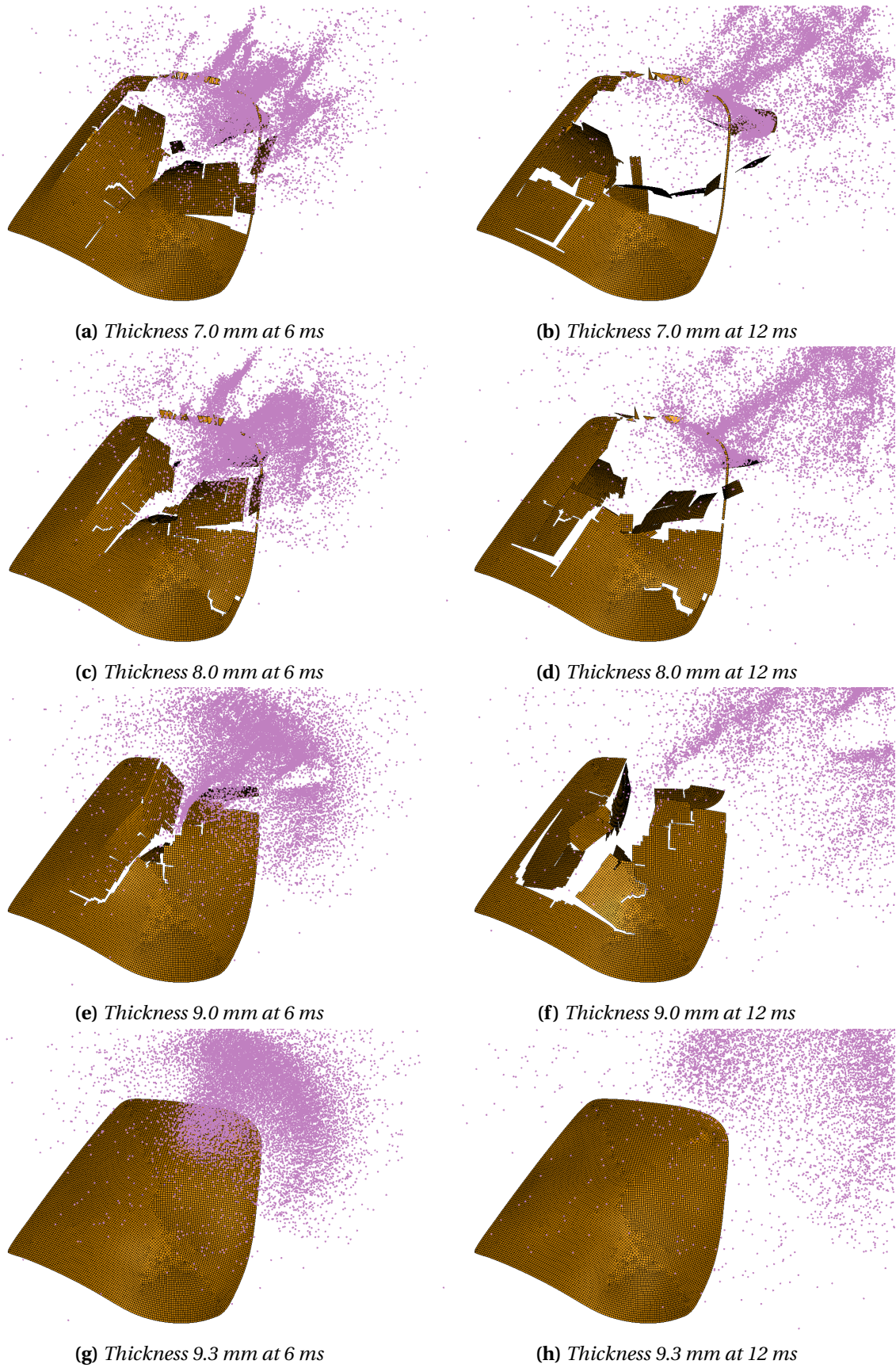
Figure C.4: *Comparison of the damage propagation of the windshield with the clamped boundary conditions for various thicknesses impacted by a 1 kg bird at different time intervals.*
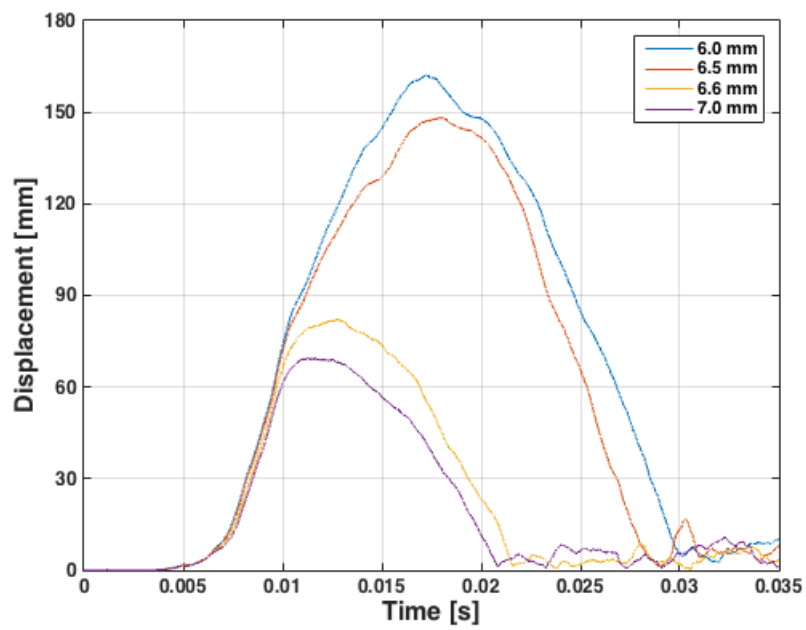
Figure C.5: *Comparison of the displacement of the top center windshield with the alternative boundary conditions over time for various windshield thicknesses.*

(a) *Thickness 6.0 mm at 6 ms*

(b) *Thickness 6.0 mm at 12 ms*

(c) *Thickness 6.5 mm at 6 ms*

(d) *Thickness 6.5 mm at 12 ms*

(e) *Thickness 6.6 mm at 6 ms*

(f) *Thickness 6.6 mm at 12 ms*

(g) *Thickness 7.0 mm at 6 ms*

(h) *Thickness 7.0 mm at 12 ms*
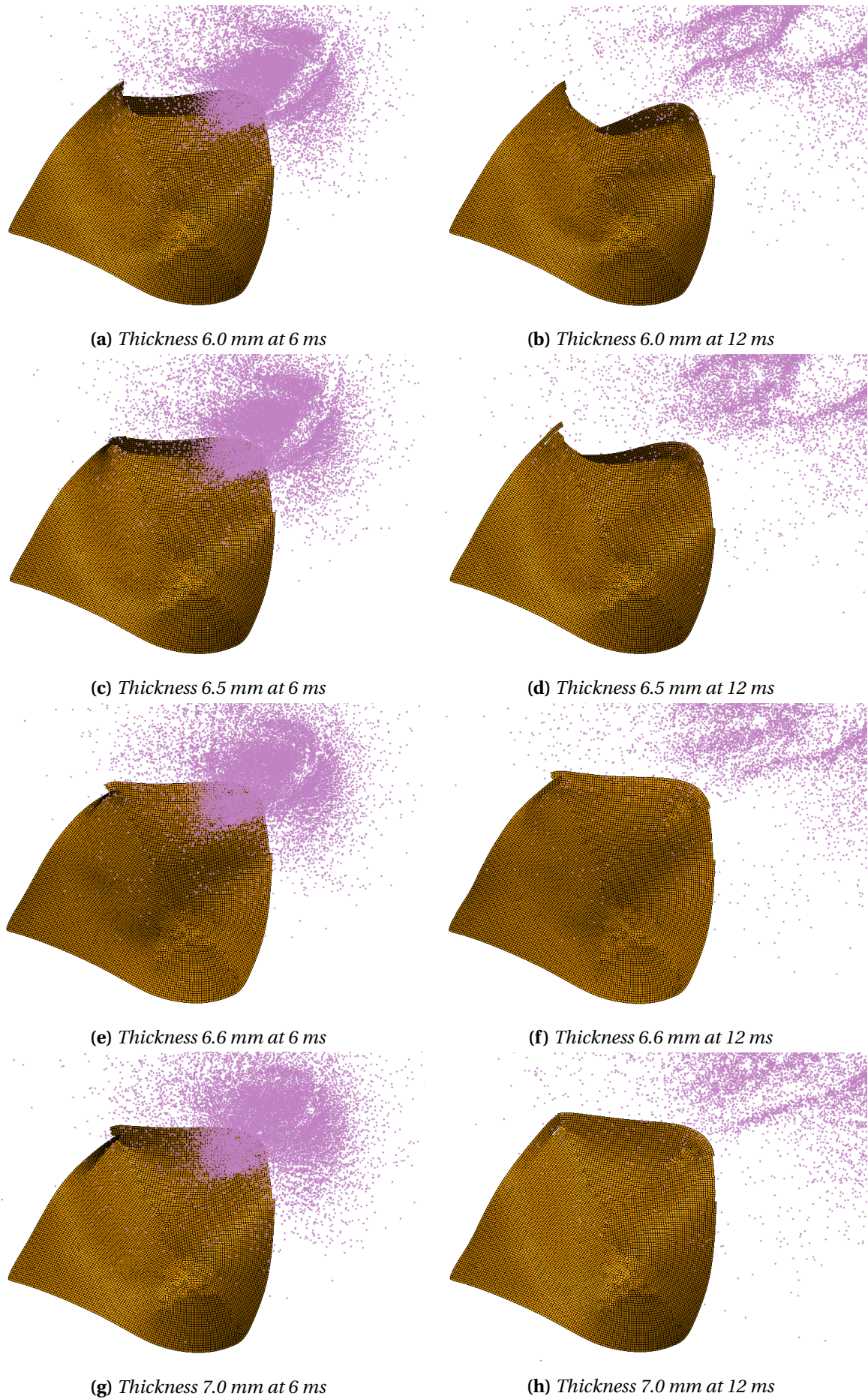
Figure C.6: *Comparison of the damage propagation of the windshield with the alternative boundary conditions for various thicknesses impacted by a 1 kg bird at different time intervals.*